

**MoDOT**

PB2002-100076



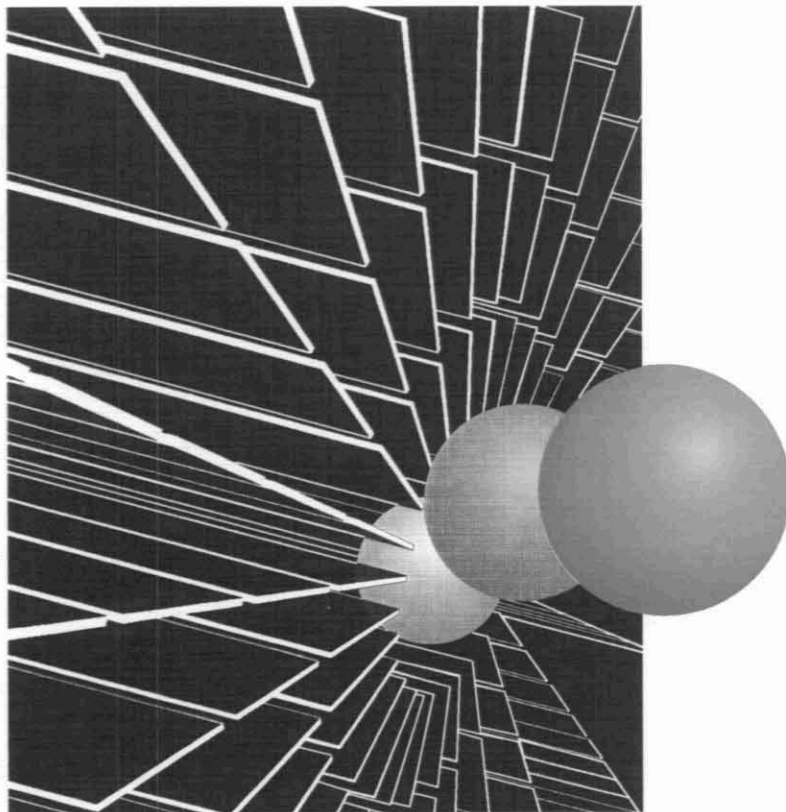
Research, Development and Technology

University of Missouri-Columbia

RDT 01-007

# Instrumentation and Monitoring of High Performance Concrete Prestressed Bridge Girders

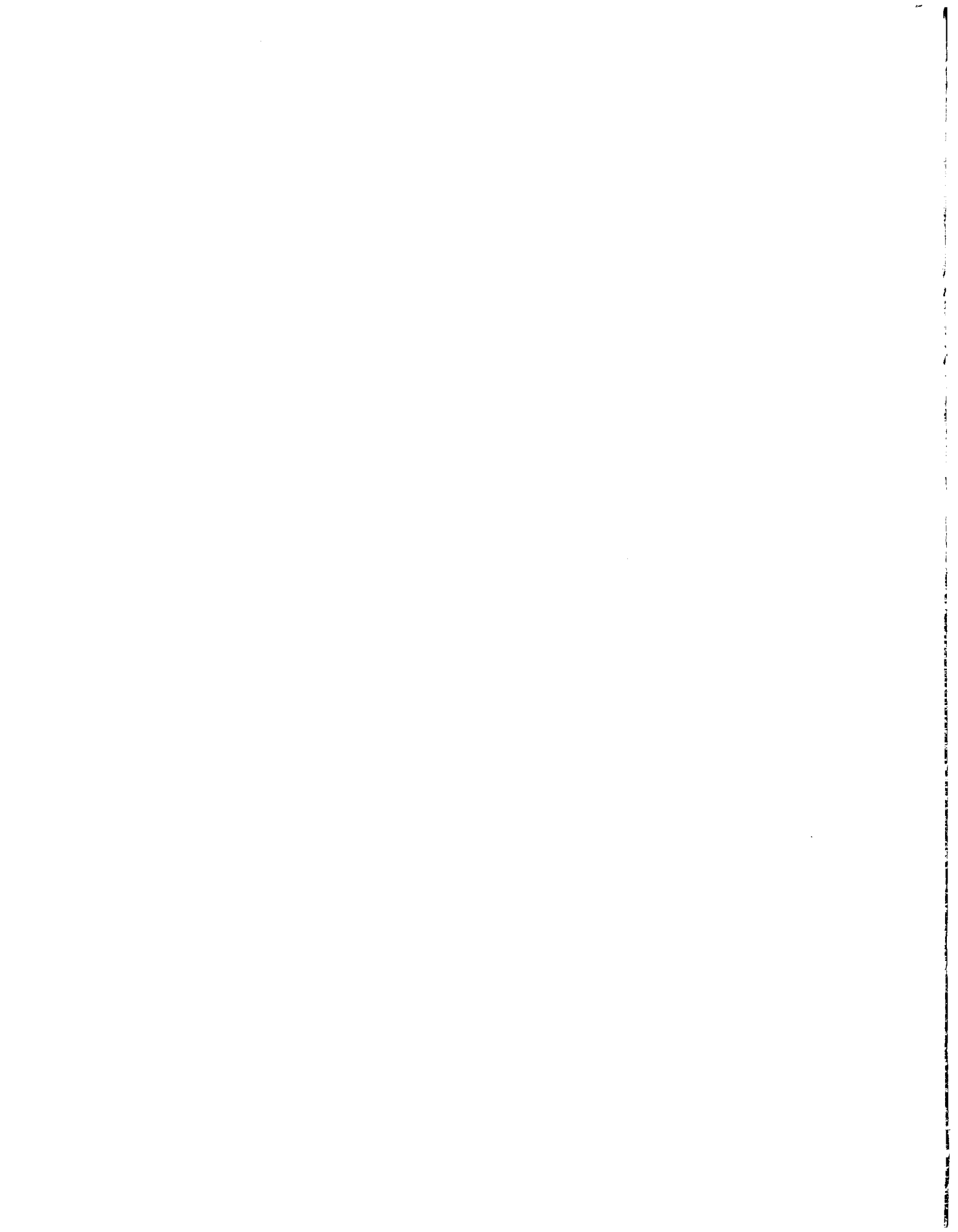
RI 97-036



May, 2001

REPRODUCED BY:  
U.S. Department of Commerce  
National Technical Information Service  
Springfield, Virginia 22161

**NTIS**



## TECHNICAL REPORT DOCUMENTATION PAGE

1. Report No. RDT 01-007	2. Government Accession No.	3. Recipient's Catalog No.	
4. Title and Subtitle Instrumentation and Monitoring of High Performance Concrete Prestressed Bridge Girders	5. Report Date May 2001		6. Performing Organization Code University of Missouri-Columbia
	8. Performing Organization Report No. RDT 01-007/RI 97-036		
7. Author(s) Vellore S. Gopalaratnam, Matthew Eatherton – University of Missouri-Columbia		10. Work Unit No.	11. Contract or Grant No.
9. Performing Organization Name and Address University of Missouri-Columbia Dept. of Civil and Environmental Engineering E2509 Engineering Building East Columbia, Missouri 65211-2200		13. Type of Report and Period Covered Final Report, January 1998 – May 2001	
		14. Sponsoring Agency Code MoDOT	
12. Sponsoring Agency Name and Address Missouri Department of Transportation Research, Development and Technology P. O. Box 270-Jefferson City, MO 65102		15. Supplementary Notes The investigation was conducted in cooperation with the U. S. Department of Transportation, Federal Highway Administration.	
16. Abstract <p>Bridge A5529 in Jefferson County, Missouri was constructed using high performance concrete (HPC) prestressed I-girders. This bridge is Missouri's first high performance concrete bridge. Four of the twenty girders for Bridge A5529 were instrumented to monitor temperatures, strains, and deflections from when the girders were fabricated up to approximately one year in service. Additional laboratory experiments included tests for compression response, fracture characteristics, unrestrained creep and unrestrained shrinkage. The unrestrained creep and shrinkage tests were also performed on cylinders from a companion normal strength concrete (NSC, Bridge A5530) bridge for comparison. Thirty-six strain-gaged bars, sixty-seven thermocouples, thirty-two vibrating wire strain gages, and eight instrumented stirrups were installed in the four girders, diaphragm, and deck slab as a part of the instrumentation program. External measurements made during girder fabrication included transfer length, end slip, camber, and an infrared thermographic survey of the steel mold for surface temperature distribution.</p> <p>The objectives of the instrumentation program included to study the early-age response during curing/hydration, investigate end-zone stresses during prestress transfer, investigate unrestrained creep and shrinkage response of HPC used in the girders and compare them with NSC used typically, examine temperature and strain variations during storage, transport and construction, compare strains and deflections during a load test to analytical predictions, and to examine strains due to daily and seasonal service temperature variations.</p> <p>It was concluded that cracking at girder ends could result from a combination of residual stresses due to early-age differential thermal loading and stresses from prestress transfer. Improved curing procedures and potential design modifications can minimize this potential for cracking.</p> <p>Unrestrained shrinkage strains in HPC were observed to be approximately 40% less than that measured for NSC under similar laboratory conditions. Total creep was 5-15% smaller for HPC compared to NSC, however the basic creep components were nearly equal. HPC exhibited high early creep (within 60 days) which soon stabilized resulting in very little additional creep strains. The improved creep and shrinkage performance of HPC can be incorporated in design so as to allow more accurate prediction of prestress losses.</p> <p>The influence line of strains from a load-test (using a total truck load of 41,780 lbs) produced predictable profiles, although the overall as-built response was approximately 30-40% stiffer compared to analytical predictions (which did not include stiffness contributions from curb, railing, barriers etc.). Maximum strains from daily and seasonal temperature variations were observed to be significant and 5-6 times than the maximum strains observed from the load-test. It would be prudent to review design procedures so that bridges of this type (continuous composite prestressed I-girder) could be explicitly designed for these levels of service thermal loading in addition to normal design loading.</p>			
17. Key Words Bridges Early Age Behavior High Performance Concrete Instrumentation Precast Girders Prestressed Concrete Thermal Loading		18. Distribution Statement No restrictions. This document is available to the public through National Technical Information Center, Springfield, Virginia 22161	
19. Security Classification (of this report) Unclassified	20. Security Classification (of this page) Unclassified	21. No. of Pages 155	22. Price

*This unnumbered page is intentionally left blank*

RESEARCH INVESTIGATION RI 97-036

**INSTRUMENTATION AND MONITORING OF HIGH PERFORMANCE  
CONCRETE PRESTRESSED BRIDGE GIRDERS**

PREPARED FOR THE  
MISSOURI DEPARTMENT OF TRANSPORTATION

IN COOPERATION WITH THE  
FEDERAL HIGHWAY ADMINISTRATION

Written by

Vellore S. Gopalaratnam  
Professor of Civil Engineering  
**University of Missouri-Columbia (UMC)**  
Columbia, Missouri

and

Matthew Eatherton,  
Engineer, **Leigh and O’Kane Engineers**, Kansas City, Missouri  
*(formerly M.S. Candidate, UMC when work was completed)*

Submitted  
May 2001

The opinions, findings and conclusions expressed in this report are those of the authors. They are not necessarily of the Missouri Department of Transportation, the U.S. Department of Transportation or the Federal Highway Administration. This report does not constitute a standard, specification or regulation.

*This unnumbered page is intentionally left blank*

## ACKNOWLEDGEMENTS

The authors would like to thank the Missouri Department of Transportation (MoDOT) for their financial support that made this project (MoDOT Study 97-8) possible. The Research, Development and Technology division, especially Patty Brake-Lemongelli, and Tim Chojnacki, were extremely helpful during the course of the project. Useful discussions with Chris Criswell and Shyam Gupta of the Bridge Division during the course of this study are also acknowledged. The authors would also like to thank the MoDOT inspections personnel including Joe Brewen, Shannon Inman, and Brian Immer for their help. Thanks also go to Eric Wade at Egyptian Concrete who did everything he could to accommodate the MU research team.

Special gratitude and thanks are extended to University of Missouri-Columbia (UMC) Senior Technician Rick Wells and Electronics Technician Richard Oberto for their wholehearted support for the project. This complex instrumentation program would not have been possible without their assistance. The timely help from Dr. Michael Barker and Senior Technician C. H. Cassil in the planning and execution of the load test is greatly appreciated. Thanks also go to Ric Whikehart of Electro-Test Inc who conducted the thermographic survey. Generous donations of solar panel components from the UMC Suntiger (solar car) Team went a great way to helping us power our data acquisition system and associated instrumentation.

The help of a number of undergraduate and graduate students were required to fabricate, install, and assist in data analysis. Thanks go to Dave Barrett, Jeremy Boxdorfer, Patrick Earney, Kevin Studer, Lee Sommers, Scott Weibenmeyer, Drew Hanke, Louie Vannetta, Jeff White and Adam Zentz.

**PROTECTED UNDER INTERNATIONAL COPYRIGHT  
ALL RIGHTS RESERVED  
NATIONAL TECHNICAL INFORMATION SERVICE  
U.S. DEPARTMENT OF COMMERCE**

Reproduced from  
best available copy. 

*This unnumbered page is intentionally left blank*

## EXECUTIVE SUMMARY

Bridge A5529 in Jefferson County, Missouri was constructed using high performance concrete (HPC) prestressed I-girders. This bridge is Missouri's first high performance concrete bridge. Four of the twenty girders for Bridge A5529 were instrumented to monitor temperatures, strains, and deflections from when the girders were fabricated up to approximately one year in service. Additional laboratory experiments included tests for compression response, fracture characteristics, unrestrained creep and unrestrained shrinkage. The unrestrained creep and shrinkage tests were also performed on cylinders from a companion normal strength concrete (NSC, Bridge A5530) bridge for comparison. Thirty-six strain-gaged bars, sixty-seven thermocouples, thirty-two vibrating wire strain gages, and eight instrumented stirrups were installed in the four girders, diaphragm, and deck slab as a part of the instrumentation program. External measurements made during girder fabrication included transfer length, end slip, camber, and an infrared thermographic survey of the steel mold for surface temperature distribution.

The objectives of the instrumentation program included to study the early-age response during curing/hydration, investigate end-zone stresses during prestress transfer, investigate unrestrained creep and shrinkage response of HPC used in the girders and compare them with NSC used typically, examine temperature and strain variations during storage, transport and construction, compare strains and deflections during a load test to analytical predictions, and to examine strains due to daily and seasonal service temperature variations.

The instrumentation program which required some serious planning to allow measurement of different parameters at different stages in the life of the girders was very successful given the fact that almost all of embedded instrumentation performed as designed. Better calibration of the response from the vibrating wire gages when subjected simultaneously to transient mechanical and thermal loads in hindsight would have been desirable. The data acquisition system designed was self contained and was powered with a solar panel at the remote bridge site. The system had the capability of remotely uploading of data acquisition programs and downloading of data through a

cellular phone. Such systems could serve well as front-ends of intelligent bridge monitoring and control systems for important bridges.

It has been concluded from the study that cracking at girder ends could result from a combination of residual stress due to differential thermal loading from curing/hydration and stresses due to prestress transfer. Improved curing procedures and potential design modifications can minimize this potential for cracking.

Unrestrained shrinkage strains in HPC were observed to be approximately 40% less than that measured for NSC under similar laboratory conditions. For the HPC mix parameters used, it was observed that autogenous shrinkage was comparable to drying shrinkage in magnitude, although the former was marginally more dominant. Total creep was 5-15% smaller for HPC compared to NSC, however the basic creep components were nearly equal. HPC exhibited high early creep (within 60 days) which soon stabilized resulting in very little additional creep strains. The improved creep and shrinkage performance of HPC can be incorporated in design so as to allow more accurate prediction of prestress losses.

Maximum strains during transportation of the girders from the precasting yard to the bridge site and construction strains were of the order of  $\pm 40 \mu\text{str}$ . The influence line of strains from a load-test (using a total truck load of 41,780 lbs) produced predictable profiles, although the overall as-built response was approximately 30-40% stiffer compared to analytical predictions (which did not include stiffness contributions from curb, railing, barriers etc.). Maximum strains from daily and seasonal temperature variations were observed to be significant and 5-6 times than the maximum strains observed from the load-test. It would be prudent to review design procedures so that bridges of this type (continuous composite prestressed I-girder) could be explicitly designed for these levels of service thermal loading in addition to normal design loading.

## TABLE OF CONTENTS

List of Figures .....	iv
List of Tables .....	viii
List of Symbols .....	ix
<b>1. Introduction .....</b>	<b>1</b>
1.1 FHWA High Performance Concrete Initiative .....	1
1.2 Project Overview .....	1
1.3 Objectives of Instrumentation.....	5
1.3.1 Overall Motivation.....	5
1.3.2 Study Early Age Thermal Loading and its Influence.....	5
1.3.3 Investigate End Zone Stresses due to Prestress Transfer.....	5
1.3.4 Monitor Transportation and Service Strains .....	6
1.3.5 Unrestrained Creep and Shrinkage .....	6
1.4 Previous Research.....	7
1.4.1 General Information on High Performance Concrete .....	7
1.4.2 Applications for HPC.....	9
1.4.3 HPC Prestressed Concrete Bridges and Instrumentation.....	9
1.4.4 Creep and Shrinkage Response of HPC.....	15
<b>2. Experimental Program .....</b>	<b>21</b>
2.1 Field Instrumentation.....	21
2.1.1 General Information on Instrumentation .....	21
2.1.2 Internal Instrumentation .....	25
2.1.3 Data Acquisition System .....	32
2.1.4 External Instrumentation .....	39
2.2 Laboratory Studies .....	44
2.2.1 General .....	44
2.2.2 Compression Tests .....	45
2.2.3 Creep Tests .....	47
2.2.4 Shrinkage Tests .....	49
2.2.5 Fracture Tests .....	51
2.2.6 MoDOT Tests .....	52
<b>3. Material Properties .....</b>	<b>53</b>
3.1 HPC Mix Design .....	53
3.2 Compression Tests on HPC .....	54
3.3 Fracture Tests on HPC .....	56
3.4 Creep and Shrinkage of HPC .....	58
3.4.1 Beam Shrinkage .....	58
3.4.2 Cylinder Shrinkage .....	59
3.4.3 Total Creep .....	60
3.4.4 Basic Creep .....	61

3.5	Prestressing Strands.....	62
3.6	Reinforcing Bar .....	63
4.	Hydration and Early Age Response .....	64
4.1	Introduction .....	64
4.2	Data From Instrumentation .....	67
4.2.1	Temperature.....	67
4.2.2	Strains .....	74
4.3	Thermographic Survey.....	78
4.3.1	General Information.....	78
4.3.2	Limitations of the Thermographic Survey .....	78
4.3.3	Results From the Thermographic Survey .....	79
5.	Stress Transfer .....	83
5.1	Introduction .....	83
5.2	Internal Strain During Transfer.....	85
5.2.1	Strains During Transfer .....	85
5.2.2	Analysis of Strains During Transfer.....	90
5.3	Camber Measurements .....	92
5.4	End Slip Measurements .....	94
5.5	Transfer Length .....	94
5.6	Cracking in the Ends of the Girders.....	94
5.6.1	Description of Cracks .....	94
5.6.2	Anchorage Zone Stresses.....	96
6.	Storage, Transport, and Construction .....	101
6.1	Transporting the Girders to the Yard .....	101
6.1.1	General .....	101
6.1.2	Strains During Movement to the Yard .....	102
6.2	Storage in the Precast Plant Yard.....	103
6.2.1	Storage Location .....	103
6.2.2	Daily Temperature Variations .....	104
6.2.3	Strains Due to Daily Temperature Variations .....	108
6.3	Transport to the Construction Site .....	108
6.3.1	Process of Transport and Installation .....	108
6.3.2	Transport Strains .....	110
6.4	Curing of the Diaphragm .....	111
6.4.1	General .....	111
6.4.2	Temperatures During Diaphragm and Slab Casting/Curing .....	111
6.4.3	Strains During Diaphragm and Slab Casting/Curing .....	112
7.	Load Testing and Service Performance.....	114
7.1	Load Test .....	114
7.1.1	Introduction .....	114
7.1.2	Equipment Used To Carry Out Load Test .....	114
7.1.3	Loading Schemes .....	114

7.1.4	Expected Strains During Load Test .....	116
7.1.5	Results from the Load Test .....	116
7.2	Service Performance .....	118
7.2.1	Introduction .....	118
7.2.2	Daily Temperature Variation .....	120
7.2.3	Daily Strain Variation .....	121
7.3	Long Term Strain and Deflection .....	123
7.3.1	Long-Term Strain Measurements .....	123
7.3.2	Long-Term Deflection Measurements .....	128
7.3.3	Curvature Comparisons .....	129
8.	Conclusions and Recommendations .....	135
8.1	Conclusions .....	135
8.2	Recommendations .....	136
9.	References .....	138
10.	Appendices .....	142
	Appendix A - Timeline for Important Events .....	142
	Appendix B - Instrumentation Wiring Schemes Used .....	143

*This unnumbered page is intentionally left blank*

## LIST OF FIGURES

Figure 1.1	Side view of Bridge A5529 .....	2
Figure 1.2	Cross-sectional view of Bridge A5529 (High Performance Concrete) and sister Normal Strength Concrete bridge .....	2
Figure 1.3	Plan view of Bridge A5529 .....	3
Figure 1.4	Cross-sectional dimensions of MoDOT Type VI girders and strand arrangement for girders in Span 1-2 .....	3
Figure 1.5	Strand arrangement for Span 2-3 .....	4
Figure 2.1	Plan view of Bridge A5529 showing instrumented girders .....	22
Figure 2.2	Instrumented cross-sections showing location of gages .....	22
Figure 2.3	Schematic showing gage locations in an instrumented stirrup .....	24
Figure 2.4	Schematic showing details of the diaphragm instrumentation .....	25
Figure 2.5	Instrumented strain-gage bar before (top) and after water proofing .....	26
Figure 2.6	Vibrating wire gage .....	27
Figure 2.7	Thermocouples after welding, labeling and sealing .....	28
Figure 2.8	Location of instrumented stirrup reinforcement in Span 1-2 girders .....	29
Figure 2.9	Location of instrumented stirrup reinforcement in Span 2-3 girders .....	29
Figure 2.10	Instrumentation and associated wires being readied for placement in the girder molds at the precasting site .....	30
Figure 2.11	Top flange instrumentation showing instrumented strain-gaged rebar and vibrating wire gage .....	31
Figure 2.12	Web instrumentation at midheight attached to stirrups .....	31
Figure 2.13	Bottom flange instrumentation showing instrumented strain-gaged rebar and vibrating wire gage .....	32
Figure 2.14	Photograph of the girder showing the end cross-section instrumentation, instrumented stirrup, and wire bundles .....	33
Figure 2.15	Terminal box undergoing fabrication .....	34
Figure 2.16	Completed terminal box ready to install .....	35
Figure 2.17	The data acquisition box showing wiring details used for the multiplexers .....	36
Figure 2.18	The finished data acquisition box .....	36
Figure 2.19	Solar power source for long-term remote data acquisition .....	38
Figure 2.20	Taut-wire deflection device showing the passive (left) and active (right) ends .....	39
Figure 2.21	Digital calipers used to measure girder deflections .....	40
Figure 2.22	Arrangement for measurement of end-slip .....	41
Figure 2.23	Digital calipers used to make end-slip measurements .....	41
Figure 2.24	Transfer length measurement being made using the Whitmore gage .....	42
Figure 2.25	Electrotest Inc. personnel recording infrared thermographic video images .....	43
Figure 2.26	Casting of the cylinders and slabs used for the laboratory tests .....	44
Figure 2.27	Compression test on 6" diameter cylinder test conducted at the MoDOT Materials Testing Laboratory .....	45
Figure 2.28	Compression test on 3" diameter cored cylinders conducted using circumferential strain control .....	46
Figure 2.29	Custom fabricated creep test frames .....	47

Figure 2.30	Strain measurements on shrinkage cylinders .....	50
Figure 2.31	Beam shrinkage specimens showing Demec points used for strain measurements .....	51
Figure 2.32	Test set-up showing CMOD controlled notched beam .....	51
Figure 3.1	Results from the compression tests on 3" cored cylinders .....	55
Figure 3.2	Results from the compression tests on 6" cylinders .....	56
Figure 3.3	Typical load – CMOD response of a notched HPC beam .....	57
Figure 3.4	Typical load – deflection response of a notched HPC beam .....	57
Figure 3.5	Beam shrinkage as a function of time .....	59
Figure 3.6	Cylinder shrinkage as a function of time .....	60
Figure 3.7	Total creep strain for sealed cylinders (including elastic shortening and autogenous shrinkage) versus time .....	61
Figure 3.8	Basic creep strain for sealed cylinders (autogenous shrinkage and elastic shortening subtracted from total creep) versus time .....	62
Figure 3.9	Stress-strain response of the reinforcing bar used for the strain-gaged bars.....	63
Figure 4.1	The sidewinder being loaded with concrete at the batch plant .....	65
Figure 4.2	Top view of the sidewinder .....	65
Figure 4.3	Placement of the concrete in the forms .....	66
Figure 4.4	Vibrating the concrete during casting .....	66
Figure 4.5	Development of temperatures in cross-section SIE .....	67
Figure 4.6	Development of temperatures in cross-section SIM .....	69
Figure 4.7	Development of temperatures in cross-section LXM .....	69
Figure 4.8	Development of temperatures in cross-section LIM .....	70
Figure 4.9	Development of temperatures in cross-section LXE .....	71
Figure 4.10	Thermistor temperatures in cross-section LXE .....	71
Figure 4.11	Difference between the maximum and minimum temperatures in the cross-sections of the long girders .....	72
Figure 4.12	Difference between the maximum and minimum temperatures in the cross-sections of the short girders .....	73
Figure 4.13	Test slab and cylinder temperatures compared to girder temperatures .....	74
Figure 4.14	Apparent strain from strain-gaged bars in cross-section LIM .....	75
Figure 4.15	Apparent strain from strain-gaged bars in cross-section SXE .....	76
Figure 4.16	Apparent strain from vibrating wire strain gages in cross-section SXE .....	77
Figure 4.17	Apparent strains in stirrups used in girder SX .....	77
Figure 4.18	Infrared photograph showing the side of girders SI and SX .....	79
Figure 4.19	Infrared photograph of girder after approximately 13.5 hours of curing .....	80
Figure 4.20	Infrared photograph of girder after approximately 19.5 hours of curing .....	80
Figure 4.21	Infrared photograph of girder after approximately 22.5 hours of curing .....	81
Figure 4.22	Maximum temperatures along the length of the girder during curing .....	82
Figure 4.23	Temperature gradients along the length of the girder during curing .....	82
Figure 5.1	Transfer of the prestress force .....	83
Figure 5.2	Close-up of the process of cutting prestressing strands with a torch .....	84
Figure 5.3	Strand cutting sequence for short girders .....	84

Figure 5.4	Strand cutting sequence for long girders	86
Figure 5.5	Strains during transfer of prestressing force for cross-section SXE	87
Figure 5.6	Strains during transfer of prestressing force for cross-section SIM	87
Figure 5.7	Strains during transfer of prestressing force for cross-section LXE	88
Figure 5.8	Strains during transfer of prestressing force for cross-section LIM	88
Figure 5.9	Stirrup strains during transfer of prestressing force for girder SI	89
Figure 5.10	Stirrup strains during transfer of prestressing force for girder LI	89
Figure 5.11	Strain distribution and gradient after transfer for cross-section SIE	90
Figure 5.12	Strain distribution and gradient after transfer for cross-section SIM	91
Figure 5.13	Strain distribution and gradient after transfer for cross-section LIE	91
Figure 5.14	Strain distribution and gradient after transfer for cross-section LIM	92
Figure 5.15	Camber profiles after prestress transfer for the short girders	93
Figure 5.16	Camber profiles after prestress transfer for the long girders	93
Figure 5.17	Transfer length measurement results	95
Figure 5.18	Photograph of girder end cracking	96
Figure 5.19	Sketches of girder-end cracks for the “marked end” of girder LI	96
Figure 5.20	Sketches of girder-end cracks for the “marked end” of girder LX	97
Figure 5.21	Modified Gergely-Sozen model (Earney 2000)	98
Figure 5.22	Assumed stress distribution from unbalanced moment	99
Figure 6.1	Gantry crane used to move girders	101
Figure 6.2	Strains in girder LI while the girder is being moved from the precasting bed	102
Figure 6.3	Stirrup strains while girder LI is moved from the precasting bed	103
Figure 6.4	Storage of the girders at the precasting yard prior to bridge construction	103
Figure 6.5	Acquiring data during the girder storage period	104
Figure 6.6	Daily variations in ambient air temperature	105
Figure 6.7	Temperature gradients in cross-section LXM due to daily ambient temperature variations	105
Figure 6.8	Daily strain variation during girder storage (girder cross-section LXM)	106
Figure 6.9	Daily variation in stirrup strain during girder storage	106
Figure 6.10	Daily variation in strain during girder storage (girder cross-section SIE)	107
Figure 6.11	Daily strain variation measured using the vibrating wire strain gages (girder cross-section SIE)	107
Figure 6.12	Transporting the girder to the bridge site	109
Figure 6.13	Setting the instrumented girders on the bents	109
Figure 6.14	Instrumented girders in place on bents	110
Figure 6.15	Strains during girder transport to the bridge site (girder cross-section SXE)	111
Figure 6.16	Diaphragm temperatures during diaphragm and slab hydration	112
Figure 6.17	Girder temperatures (LXM) during diaphragm and slab hydration	113
Figure 6.18	Strains in girder cross-section LXM during the curing of the diaphragm and slab	113
Figure 7.1	Load truck and markings on the bridge for the load test	115
Figure 7.2	Load test in progress	115

Figure 7.3	Strains from the load test in cross-section LXM measured by vibrating gages .....	117
Figure 7.4	Strains from the load test in cross-section LIM measured by strain-gaged bars .....	118
Figure 7.5	Strains from the load test in cross-section SIE measured by strain-gaged bars .....	119
Figure 7.6	Strains from the load test in cross-section SXM measured by vibrating gages .....	119
Figure 7.7	Daily temperature variations in the girder and the diaphragm .....	120
Figure 7.8	Strains due to daily temperature variations (cross-section LIE) .....	121
Figure 7.9	Strains due to daily temperature variations (cross-section LXM) .....	121
Figure 7.10	Strains due to daily temperature variations (cross-section SIE) .....	122
Figure 7.11	Strains due to daily temperature variations (cross-section SIM) .....	122
Figure 7.12	Stirrup strains due to daily temperature variations (cross-section SIM) .....	124
Figure 7.13	Diaphragm strains due to daily temperature variations .....	124
Figure 7.14	Platform built to facilitate easy data acquisition and wiring reconfigurations ....	125
Figure 7.15	Access to the work platform using a 30-ft ladder .....	125
Figure 7.16	Strains due to service temperatures during a period of increasing temperature in cross-section SIE .....	127
Figure 7.17	Strains due to service temperatures during a period of decreasing temperature in cross-section SIE .....	127
Figure 7.18	Deflections in girder SX at selected times during the girder life .....	128
Figure 7.19	Deflections for girder LX at selected times during the girder life .....	129
Figure 7.20	Measured strain gradients at selected times for cross-section LIE .....	130
Figure 7.21	Measured strain gradients at selected times for cross-section LXM .....	131
Figure 7.22	Measured strain gradients at selected times for cross-section SIM .....	131
Figure 7.23	Measured strain gradients at selected times for cross-section SXE .....	132

## LIST OF TABLES

Table 1.1	Ultimate creep coefficient, $C_u$ (from Nawy, 1996)	17
Table 3.1	Typical proportioning for HPC and NSC mixes	54
Table 3.2	Results from the compression tests on 3" cored cylinders	55
Table 3.3	Summary of the results from the compression tests on 6" cylinders (cast and cured along with the girders)	56
Table 3.4	Summary of results from the fracture tests	58
Table 5.1	Elapsed time in minutes for prestress transfer operations of short girders	85
Table 5.2	Elapsed time in minutes for prestress transfer operations of long girders	86
Table 5.3	Experimental determination of zero strain location from stirrup strain data	99
Table 5.4	Maximum tensile stress and location due to prestress transfer using the Gergely – Sozen model	100
Table 7.1	Analytically predicted strains based on the load truck used	116
Table 7.2	Time-dependent deflections due to prestress force	129
Table 7.3	Measured curvatures in girder SI at selected times	132
Table 7.4	Measured curvatures in girder SX at selected times	133
Table 7.5	Measured curvatures in girder LI at selected times	133
Table 7.6	Measured curvatures in girder LX at selected times	134
Table A1	Timeline for important events	142
Table B1	Multiplexer 1 wiring scheme for Setup 1	143
Table B2	Multiplexer 2 wiring scheme for Setup 1	144
Table B3	Multiplexer 3 wiring scheme for Setup 1	145
Table B4	Multiplexer 1 wiring scheme for Setup 2	146
Table B5	Multiplexer 2 wiring scheme for Setup 2	146
Table B6	Multiplexer 3 wiring scheme for Setup 2	147
Table B7	Multiplexer 1 wiring scheme for Setup 3	147
Table B8	Multiplexer 2 wiring scheme for Setup 3	148
Table B9	Multiplexer 3 wiring scheme for Setup 3	148

*This unnumbered page is intentionally left blank*

## LIST OF SYMBOLS

$a$	= air content in percent
$c$	= cement content in $\text{kg/m}^3$
$C_U$	= Ultimate creep coefficient
$CTOD_c$	= Critical crack tip opening displacement
$d$	= effective depth of the prestressed reinforcement at midspan
$E$	= elastic modulus of a material
$E_c(t)$	= elastic modulus of concrete at time, $t$
$f'_c$	= compressive strength of concrete
$f_c(t)$	= compressive strength of concrete at time, $t$
$G_f$	= Fracture energy
$h$	= total height of girder
$h_f$	= height of bottom flange bulb
$h_o$	= average thickness in the size/shape correction equation of the ACI creep model
$I$	= first moment of inertia about the centroid of section
$K_{IC}^s$	= Mode I steady-state fracture toughness in the Two-Parameter Fracture Model
$M$	= the resultant moment of the thermal stresses
$m$	= gradient of stress distribution on girder end segment
$P$	= the resultant force of the thermal stresses
$T_c$	= time in days in the correction factor for curing in the ACI shrinkage model
$t$	= age of concrete in days
$t_w$	= web thickness
$V$	= externally applied shear force
$V_p$	= vertical component of prestressing force
$x$	= length of girder used in Gergely-Sozen analysis
$y$	= location along girder height above bottom flange bulb (Gergely-Sozen analysis)
$y_f$	= height of resultant force from stress distribution on bottom flange bulb
$y_{ps}$	= height of centroid of prestressing force, $P$
$\gamma_{1-6}$	= ACI correction coefficients for creep and shrinkage strains

- $\epsilon(t)$  = total strain at time t in days (instantaneous elastic strain plus creep strain)
- $\epsilon_{sh}(t)$  = shrinkage strain at time t in days
- $\epsilon_{sh}^*$  = ultimate shrinkage strain as time tends to infinity
- $\sigma_f$  = magnitude of stress distribution at top of bottom flange bulb
- $\sigma_o$  = sustained stress in the ACI creep model
- $\sigma_t$  = magnitude of stress distribution at location of maximum moment, y
- $\phi(t,\tau)$  = creep coefficient at time t, loaded from age  $\tau$
- $\tau$  = age at loading, in days
- $\psi$  = percent ratio of fine aggregate to total aggregate in the correction factor for concrete composition in the ACI shrinkage model

# 1. INTRODUCTION

## 1.1 FHWA High Performance Concrete Initiative

In the early 1990's, the Federal Highway Administration (FHWA) initiated a national program to promote and implement the use of high performance concrete (HPC) in bridges. A total of 18 bridges were constructed in 13 states as demonstration projects. As a part of the HPC initiative, the FHWA in cooperation with the states sponsored various HPC showcase workshops to share technology and experiences gained. The first of these was held in Houston, Texas in March 1996. In addition to the FHWA sponsored HPC projects, several other states including Missouri, have implemented the use of HPC in bridge projects.

Missouri constructed its first bridge using HPC girders in October 1998. The Missouri Department of Transportation (MoDOT) has also begun the planning and design of other bridges that will use HPC not only in the girders but also in the superstructure (decks) and/or the substructure (piers, bents). To facilitate the incorporation of HPC into bridge construction and share its expertise with others involved in concrete construction in the state, MoDOT formed a Focus Team on HPC for Bridges. This team is made up of MoDOT personnel from several divisions, and representatives from concrete precast plants, contractors, and academic institutions. With the need for greater quality control and the use of performance-based specifications in HPC applications, the need for communication and cooperation between all the above parties becomes important.

## 1.2 Project Overview

Bridge A5529, in Jefferson County, Missouri, is the first bridge in Missouri to utilize HPC. It is approximately 30 miles south of St Louis, Missouri. The bridge is an overpass carrying Route 21 over a relocated Route M. Figure 1.1 shows a side view of the bridge with Route M and Route 21 labeled.

The bridge carries the northbound traffic of Route 21 while a sister bridge designed using Normal Strength Concrete (NSC) carries the southbound traffic. Both are four span bridges of similar span lengths. The NSC Bridge utilizes a six-girder line cross-section as shown in Figure 1.2. By specifying the concrete strength to be 10,000 psi at 56 days one girder line could be removed. The cross-section of bridge A5529 is also shown in Figure 1.2. A plan view of Bridge

A5529 is shown in Figure 1.3. The bridge has a skew of almost 14°. The four span lengths, bent labeling, and span labeling are shown.

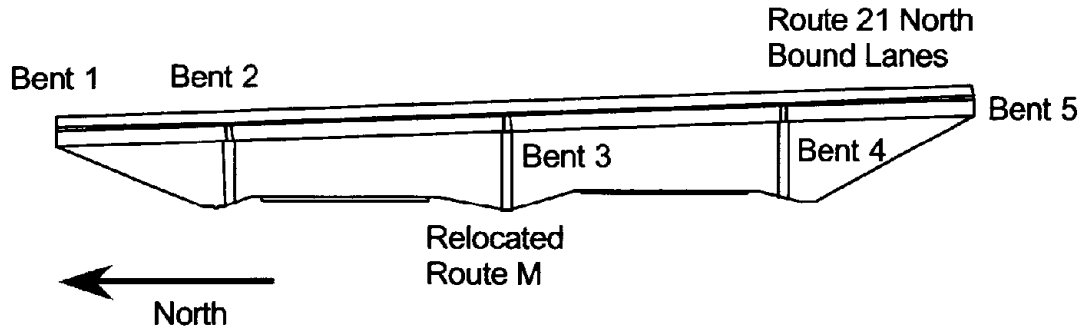


**Figure 1.1 Side view of Bridge A5529**

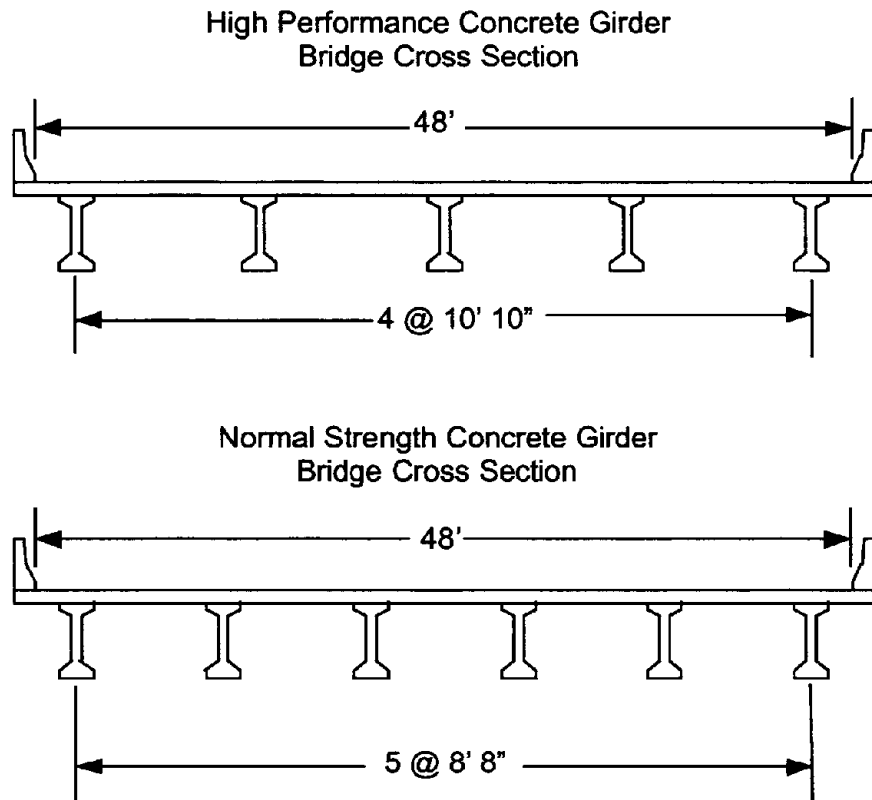


**Figure 1.2 Cross-sectional view of Bridge A5529 (High Performance Concrete) and sister Normal Strength Concrete bridge**

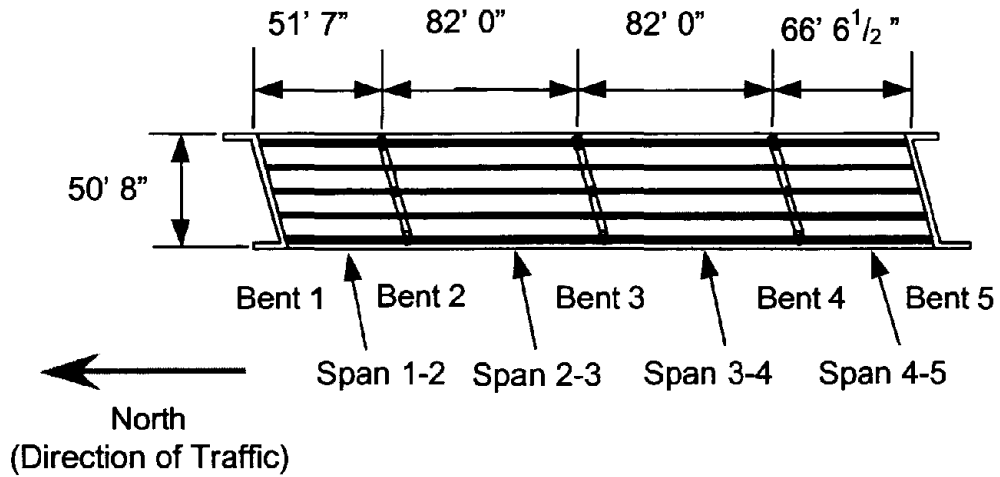


**Figure 1.3 Plan view of Bridge A5529**

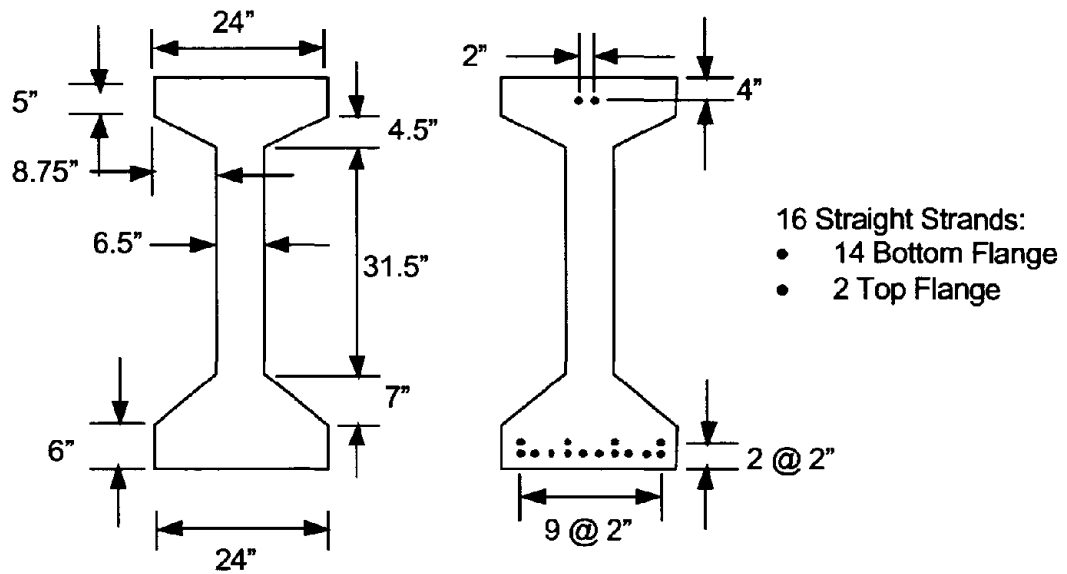


**Figure 1.4 Cross-sectional dimensions of MoDOT Type VI girders and strand arrangement for girders in Span 1-2**

The girders in both bridges are standard MoDOT Type VI girders. The dimensions of a Type VI girder are given in Figure 1.4. The concrete compressive strength was specified to be 10,000-psi at 56 days as opposed to a 5,000- or 6,000-psi design strength typically used. A compressive strength of 5,500-psi at transfer was also specified. The rest of the superstructure and the substructure were constructed using normal strength concrete.

All of the instrumentation used in the project described in this report was used in Span 1-2 and Span 2-3. For this reason the strand arrangements of Span 1-2 and Span 2-3 are detailed in Figure 1.4 and Figure 1.5. Span 1-2 used only straight strands while the other three spans all used a combination of straight and draped strands. The strands are  $\frac{1}{2}$ , seven wire, low relaxation, Grade 270 prestressing strands with an initial prestress force of 31 kips each. This adds up to 496 kips total prestress force for Span 1-2 girders and 868 kips for Span 2-3.

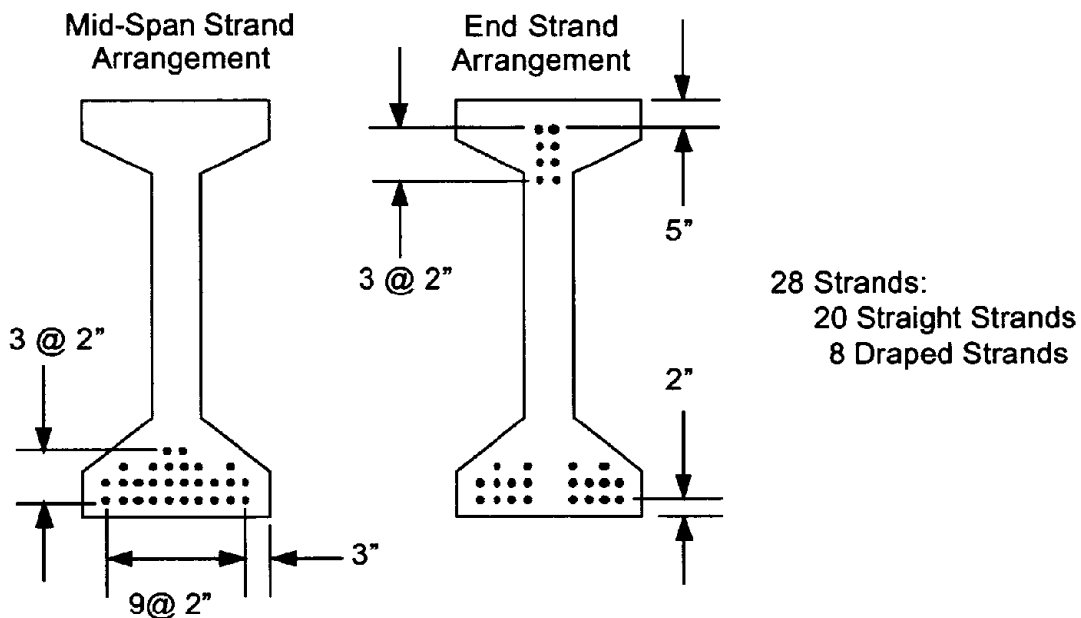


**Figure 1.5 Strand arrangement for Span 2-3**

The HPC prestressed precast bridge girders were fabricated by Egyptian Concrete Company in Bonne Terre, Missouri. The contractor in charge of the erection of the bridge was Pace Construction of St. Louis, Missouri. The girders were cast during late-July of 1998. The bridge was constructed in October 1998 and opened for traffic in November 1998. A timeline of major activities associated with the project are listed in Appendix 1.

## **1.3 Objectives of Instrumentation**

### **1.3.1 Overall Motivation**

The overall motivation of the instrumentation and monitoring project was to get a better understanding of early age and long-term performance characteristics of HPC bridge girders. Most of the design equations and procedures currently incorporated in design codes and manuals are based on data from normal strength concrete. Information and associated experience from this and other similar projects will eventually lead to development of design equations and procedures that are specifically valid for HPC. More specific objectives of the current investigation are described in the following sub-sections.

### **1.3.2 Study Early Age Thermal Loading and its Influence**

One concern about the use of high performance concrete is with regard to hydration temperatures. High cement content in HPC mixes typically result in higher internal temperatures during hydration. Differential temperature gradients could also, as a result, be significant. One specific objective of the instrumentation program was to monitor the temperatures in the girders during hydration.

The larger temperature gradients during curing can result in greater magnitudes of residual stresses in the girders. It is also possible for different sections of the girder to hydrate at different rates due to elevated temperatures, which may aggravate the residual stress problem. It is the goal of this instrumentation program to measure these temperature gradients, which in turn will allow computation of residual stress levels.

### **1.3.3 Investigate End Zone Stresses due to Prestress Transfer**

The transferring of the prestress force by cutting the prestressing strands is perhaps one the most critical loading stages in the life of a girder. Much of the technique of stress transfer used today has been learned from experience. Monitoring of the strains with a view to understanding the potential for cracking will be undertaken. The experimentally measured strains and strain gradients during transfer will be compared to analytical predictions. The potential for girder end cracking will be evaluated due to the combined effects of residual stress from early-age temperature gradients and stress due to transfer of prestress from the strands to the concrete.

#### **1.3.4 Monitor Transportation and Service Strains**

Design of bridge girders by AASHTO and MoDOT standards involve analysis of the strength of the girder after transfer with only dead load applied and after erection of the bridge in a continuous composite state. Often the strains from the periods of time before and after erection of the bridge are not specifically incorporated in design. Knowledge of transportation strains, particularly since HPC application allows longer span lengths, would facilitate optimization of girder design.

The influence of ambient temperature fluctuations on prestressed bridge girders is not adequately accounted for in many design procedures. Uniform temperature changes cause strain by themselves, but when differential temperatures are applied, the problem becomes significantly more complicated. If thermal loading were applied to the deck of a bridge, negative moment would be expected in the bridge. Also, if thermal loading were applied to only one side of a bridge as happens at various times of the day, in-plane bending would result. This experimental investigation provides useful data for a systematic study of strains in the composite structure due to changes in the ambient temperature. Interesting effects of daily and seasonal temperature variations are also reported. Temperature effects are also likely to influence the bridge depending upon the season (winter, summer etc.) when the bridge was made continuous and composite.

A live load test was also carried out to observe the in service performance of the bridge. The measured strain response is compared to predictions to observe the as-built stiffness of the barrier curbs, and amount of composite action between girders and slab.

#### **1.3.5 Unrestrained Creep and Shrinkage**

The time dependant effects such as creep and shrinkage contribute to reducing prestress force and producing larger deflections. It is important to understand the time dependent properties of HPC and how they influence strains on the bridge girders. Laboratory tests on unrestrained creep and shrinkage were carried out on both HPC and NSC as part of the experimental program. The results are compared to observed strains and deflections in Bridge A5529. The creep and shrinkage characteristics of HPC are also compared to those of normal concrete typically used by MoDOT in its prestressed I-girders.

## 1.4 Previous Research

### 1.4.1 General Information on High Performance Concrete

The American Concrete Institute defines high performance concrete (HPC) as “Concrete that meets special performance and uniformity requirements that cannot always be achieved routinely by using only conventional materials and normal mixing, placing, and curing practices” (Russell, 1977). This definition covers a wide range of concretes that have select properties engineered for specific applications.

Concrete consists of a binding medium and a relatively inert filler. Generally the binding material is hydraulic cement, like Portland cement, mixed with water. The filler is usually some type of mineral aggregate. In addition to these ingredients, admixtures can be added to improve particular properties of the concrete. Some of the major types of admixtures are summarized below (Troxell et al., 1968, Popovics, 1992).

- Air-entraining admixtures
- Superplasticizers
- Granulated blast furnace slag
- Fly ash
- Silica fume
- Retarding admixtures
- Accelerating admixtures
- Polymers and latexes

It is with one or more of these admixtures that certain characteristics of the concrete are improved. Reasons for using these admixtures include improving workability of fresh concrete, reducing required water, improving durability, controlling the set time, promoting a pozzolanic reaction with liberated lime, increasing strength, and decreasing permeability. It is with the use of these admixtures that high performance concrete can be made.

Superplasticizers also referred to as high range water reducers, act to disperse the cement particles and thereby decrease the amount of water required. This is accomplished by deflocculating cement grains, which tend to group together. This defloculation occurs as a result of a decrease in the surface tension of water and an equipolar charging of the cement particles (Nawy, 1996).

The introduction of fine pozzolanic materials can greatly increase some of the mechanical properties of concrete. Pozzolanic materials are high in  $\text{SiO}_2$  and often also  $\text{Al}_2\text{O}_3$ . These compounds react with the quicklime -  $\text{CaO}$ , which is liberated from the cement during hydration.

The result is not only to use up potentially harmful liberated CaO but to also create more binder material (Taylor, 1997).

Commonly used pozzolanic materials include fly ash, ground granulated blast furnace slag, natural pozzolans, and silica fume. These materials are usually much smaller than the cement particles. The smaller particles act to widen the range of grain size in the concrete mix and fill voids (Mailer, 1992). It should be noted, however, that without the use of a deflocculating agent the use of these fine pozzolanic materials does not have as much effect.

The use of superplasticizers and fine pozzolanic materials generally increases the compressive strength and lowers the permeability of the hardened concrete. This is the type of high performance concrete that is the subject of this research where performance specifications target compressive strength and chloride permeability.

Up until the 1950s concrete with 5000 psi (34.5 MPa) compressive strength was often hard to produce (Nawy, 1996). With the introduction of new admixtures and better quality constituents, concretes with compressive strength of 5000 psi (34.5 MPa) are now commonplace. At this time concrete strengths greater than 6000 psi (41.4 MPa) are generally considered high strength (Zia et al., 1997). Concrete with cylinder compressive strength of 20,000 psi (137.9 MPa) has been used in high-rise structures in the United States, while concretes with much larger strengths can be made in the lab. Currently the conventional designs of bridges in Missouri use concrete compressive strengths of 5,000 psi (34.5 MPa) or 6,000 psi (41.38 MPa) for the girders.

During the course of this experimental investigation, the ease with which concrete now termed as “high strength concrete” can be made became very clear. Normally the concrete strength for girders in a prestressed I-Girder bridge is specified to be 5000 psi (34.5 MPa). Often these design mixes end up providing in-service compressive strengths of 7,000 psi – 8,000 psi (48.3 MPa – 55.2 MPa) that would qualify for being called high strength or high performance concrete.

Increased performance is realized in areas such as ease of placement and compaction without segregation, enhanced long-term mechanical properties, high early-age strength, high toughness, volume stability, and long life in severe environments. HPC mixes incorporate mineral and chemical admixtures, fibers and other unconventional materials to achieve the desired properties. Grades of HPC have been defined in published literature and one such classification is provided by Goodspeed et al., 1996.

## **1.4.2 Applications for HPC**

The benefits of high performance concrete can and are being realized in many different applications. High strength concrete has been used in columns of high-rise buildings for years. The increased durability of HPC has made it a prime candidate for overlays and pavements. It has only been in the past decade that state transportation departments have taken interest in HPC for use in bridges.

Use of HPC in bridge applications has gained much wider acceptance in Europe and Japan (Goodspeed et al., 1996). Bridges using HPC have been built in Japan as early as the beginning of the 1970's. It is the challenge of experimental studies such as this one to increase confidence levels at the customer / user level so that more bridges and other structures are designed and built with HPC.

It is only natural that bridge designers would want to use HPC in bridge applications because of its higher strength and durability. Advantages of using HPC in bridges include longer spans, fewer girder lines, shallower sections, increased life span, less prestress losses, less long-term deflections, and higher modulus of elasticity. The initial cost of an HPC girder will be higher but it can be expected that this difference will reduce considerably once the quality control needed to produce HPC is achieved regularly. For the bridge that is the focus of this experimental investigation, the initial cost of the HPC girders per linear foot was higher by approximately 39% over normal strength concrete girders. Even though this price increase will reduce with time, it is necessary to also mention that the number of girders required was reduced by 16% by eliminating a line of girders.

## **1.4.3 HPC Prestressed Concrete Bridges and Instrumentation**

It was in the late 1700's and early 1800's that Smeaton, Vicat, and Apsdin contributed to inventing modern concrete. Then in the mid 1800's Monier, Loanbot, Coignet, and Hennebique put it to use in the first reinforced concrete buildings (Mailer, 1991, Popovics, 1992). It was in the early 1950's that the precast / prestressed concrete I-girders were first used in the United States (Geren et al., 1992). In the past few decades innovative admixtures have been developed. Fly ash and blast furnace slag are waste materials and were first used as a filler to reduce the amount of cement necessary. Silica fume was first used in construction in the 1970's when it was added to concrete during the construction of the Fiskaa smelter in Norway (Mailer, 1991).

High performance concrete has been used in the columns of high rise buildings for some time now, but it has only been recently that the benefits of HPC are being utilized in bridge structures. The following paragraphs of this section describe the bridges that have been constructed, or will be constructed with HPC.

#### **1.4.3.1 Texas**

Texas, one of AASHTO's lead states in HPC has been at the forefront in application of HPC in bridges. The Louetta Road Overpass in Houston, Texas utilizes a newly developed U-shaped cross-section beam (Geren et al., 1992, FHWA, 1997g). Most of the prestressing strands were 0.6" (15.2 mm) instead of the smaller 0.5" (12.7 mm) diameter strands. HPC was used in most aspects of the bridge design including the piers and deck. Concrete strengths for the beams typically exceeded 7000 psi (48.9 MPa) at transfer and ranged between 10,000 psi (69.9 MPa) and 13,000 psi (90.8 MPa) at 56 days. The bridge was constructed in 1997.

Twelve of the thirty-three beams in the Louetta Road Overpass were instrumented (Gross, 1994). Types of gages used were strain-gaged bars, vibrating wire strain gages, and thermocouples. Sixty-four strain-gaged bars (made from #3 reinforcing bars), thirty-two vibrating wire strain gages, and thirty-two thermocouples were installed. Demec mechanical strain gages were used to measure surface strains and a piano wire deflection system was used on the twelve-instrumented beams. Four CR10 dataloggers from Campbell scientific and nine AM416 multiplexers were used to acquire data from the transducers.

The other bridge in Texas that has gotten a significant amount of attention for being built with HPC is the San Angelo Bridge, also known as the North Concho River, U. S. 87 and South Orient Railroad Overpass (Gross, 1995, Ralls, 1996, Ralls, FHWA, 1997h, Ralls, 1998). This overpass consists of eastbound and westbound bridges. The eastbound bridge was designed using HPC. The girders for this bridge are AASHTO Type IV girders with straight pretensioned strands and draped post tensioned strands. All strands are 0.6" (15.2 mm) diameter. Concrete strengths at transfer usually exceeded 8,900 psi (62.2 MPa). The 56-day strength reached values of 14,700 psi (102.7 MPa). The deck utilized HPC as well as a reinforcing bar with a new pattern of deformations to provide improved bond characteristics.

The San Angelo Bridge was instrumented similar to the Louetta Road Overpass. Vibrating wire strain gages, strain-gaged bars, and thermocouples were installed in the girders. Fourteen of the eighty-four girders were instrumented. Ten of these were high strength girders

and four of these were normal strength concrete. Sixty-four strain-gaged bars, sixteen vibrating wire strain gages, and sixteen thermocouples were used along with four AM416 multiplexers and one CR10 datalogger.

One concern with using HPC to extend girder lengths with standard AASHTO type girders is stability (Ralls, 1998). The maximum length of an AASHTO Type IV girder designed for a 56-day compressive strength of 10,000 psi (69.9 MPa) is 153 ft (46.7 m), as opposed to a maximum span of 120 ft (36.6 m) using NSC. This represents an increase in the span-to-depth ratio from 27 to 34 with the use of HPC. Stability and deflections may be a problem with these longer spans. One of the spans in the San Angelo Bridge extended 157 ft (47.9 m) using AASHTO Type IV girders.

#### **1.4.3.2 Virginia**

Virginia has several bridges utilizing HPC (Ozyildirin et al., 1996, FHWA, 1997I, 1997j, Ozyildirin et al., 1999). One of Virginia's goals is to use 0.6" (15.2 mm) diameter strand in conjunction with HPC in prestressed I-girders. The Richlands Bridge has been designed using these larger diameter strands.

Experimental lab studies of several full size girders were conducted. These full size girders were AASHTO Type II girders with 0.6 in (15.2 mm) prestressing strands. Temperatures in the test girders were monitored during curing and were found to approach 85° C (185° F). Cylinders stored near the girders during curing exhibited visual cracks and lower strengths than expected due to heat damage.

The only HPC Bridge to be instrumented is the Richlands Bridge (Ozyildirin and Gomez, 1996). Three of the girders were evaluated for transfer length and end slip at release of pretensioning forces. Internal concrete strains and temperatures were to be monitored during and after fabrication, as well as during and after erection. Measurements for loss in camber were periodically taken.

#### **1.4.3.3 Nebraska**

The 120<sup>th</sup> Street and Giles Road Bridge in Sarpy County, Nebraska used HPC bridge girders (Geren et al., 1992, Einea et al., 1996, Yelton, 1996, FHWA, 1997c). The girder shape was the NU1100 bulb-tee (1100 mm high) developed in a girder optimization program performed by the University of Nebraska at Omaha. The girder strengths were specified to be

12,000 psi (83 MPa) at 56 days and 5,500 psi (38 MPa) at transfer. The deck was specified to have a 56-day compressive strength of 8,000 psi (55 MPa) and chloride permeability less than 1800 Coulombs at 56 days.

The girders were instrumented with strain-gaged bars, thermocouples, and vibrating wire strain gages. The deck was also instrumented with these same types of internal gages in 12 locations. Vibrating wire strain gages were placed in the diaphragms to evaluate the restraining forces generated at the end of the girders. Surface strains were measured using external mechanical gages. Girder camber, end rotation, prestressing force, and shrinkage were also measured. The girders were produced in the fall of 1995 and the bridge was opened to traffic in 1996. Live load tests were carried out using two loaded trucks. More load tests were scheduled at year intervals.

An in-depth parametric study was conducted at the University of Nebraska aimed at developing optimized precast / prestressed concrete I-girders for use in continuous-span bridges (Geren et al., 1992). The 7 NU1100 bulb-tee was the result of this study and is being examined as a part of the field instrumentation program as much as the use of HPC in bridge structures.

#### **1.4.3.4 New Hampshire**

One bridge has been constructed and another was under construction utilizing HPC in New Hampshire (FHWA, 1997d, 1997e, Waszczuk and Juliano, 1999). The first bridge is the Route 104 bridge over the Newfound River in Bristol, New Hampshire. The girders are AASHTO Type III girders with a 56-day compressive strength of 8,000 psi (55.9 MPa) and 6,500 psi (45.4 MPa) at transfer.

Special care was taken in selecting bridge deck concrete mixes. After laboratory testing three mixes were field tested by exposing them to truck traffic at a local waste management site over the winter of 1995-1996. Several parameters were evaluated to determine the best mix for use in the deck of the Route 104 bridge. The mix selected utilized silica fume, had an air content of 6 to 9 percent, corrosion inhibitor, chloride permeability less than 1000 coulombs, and a compressive strength of 7,200 psi (50 MPa). The bridge was constructed in 1996. There is no report of an instrumentation program on this bridge.

New Hampshire's second HPC bridge is the Route 3A Bridge over the Newfound River also in Bristol, New Hampshire. The bridge is a simple-span 60 ft (18.3 m) bridge using 4 New England (NE) Bulb-Tee girder sections. The NE Bulb-Tee section was recently developed for

the region as a new economical section. 0.6” (15.2 mm) diameter prestressing strand is used. A 28-day compressive strength of 8,000 psi (55 MPa), and 5,500 psi (38 MPa) at transfer is specified. Limited instrumentation of two girders was planned.

#### **1.4.3.5 Washington**

The eastbound State Route 18 bridge over State Route 515 in King County, Washington has been constructed using HPC (FHWA, 1997k). The girders are pretensioned Washington State Department of Transportation WSDOT W74G girders that are 74 in (1880 mm) built with composite deck. The prestressing strands are 0.6” (15.2 mm) diameter. The deck concrete is WSDOT Class 4000D concrete, which contains fly ash. No instrumentation program was reported for this bridge.

#### **1.4.3.6 North Carolina**

The U.S. 401 Bridge over the Neuse River in Wake County, North Carolina was constructed using HPC (FHWA, 1997f). The girders are AASHTO Type IV prestressed concrete I-girders utilizing 0.6” (15.2 mm) diameter prestressing strands. The 28 day compressive strength was specified at 10,000 psi (69 MPa) and 7,000 psi (48 MPa) at transfer.

Internal and external instrumentation was installed on four girders. Temperature, camber and transfer length were examined. There is no report of instrumentation to monitor internal strains.

#### **1.4.3.7 Georgia**

Georgia is conducting research to determine the best mixes to accomplish FHWA HPC Grades 1, 2 and 4 using Georgia aggregates, and evaluate the local HPC production capability. Also studies are being conducted to evaluate the bond of 0.6 in (15.2 mm) diameter prestressing strands. The site for Georgia’s first HPC bridge was tentatively identified as the bridge over Interstate 75 in Henry County, Georgia (FHWA, 1997b). Construction was scheduled for the beginning of 1998. An instrumentation program was planned for the HPC bridge including thermocouples, vibrating wire strain gages, surface strains, camber, and initial prestress force.

#### **1.4.3.8 Alabama**

The Highway 199 bridge over the Uphaupee and Bulger Creek in Macon County, Alabama was constructed using HPC (FHWA, 1997a). The girders were AASHTO BT-54 Bulb-

Tee girders. The 28 day compressive strength of the girder concrete was specified to be 10,000 psi (69 MPa), and 9,000 psi (62 MPa) at transfer. The deck and substructure will use concrete with 28 day compressive strength of 6,000 psi (41 MPa), although the substructure was designed based on a compressive strength of 3,000 psi (21 MPa). The girders were instrumented to monitor behavior from placement of concrete through long-term service life. Instrumentation consists of thermocouples, strain-gaged bars, and vibrating wire strain gages. The deflections were also monitored.

#### **1.4.3.9 Minnesota**

Minnesota has done extensive laboratory research on the mechanical properties of HPC as it applies to prestressed concrete construction (Ahlborn et al., 1995, 1996, Mokhtarzadey et al., 1995, French, et al., 1998). Minnesota has also conducted load tests on full scale high-strength concrete composite prestressed bridge girders. These tests were performed to investigate issues such as transfer length, long-term prestress losses, fatigue, ultimate flexure, and shear strengths. A parametric study was also conducted to examine the effect of increased concrete strength on maximum achievable girder span lengths and spacings for a series of Minnesota Department of Transportation prestressed I-girder sections. No field instrumentation of in-service bridge girders has been reported for Minnesota.

#### **1.4.3.10 Louisiana**

Four high strength prestressed, pretensioned bulb-tee girders were fabricated (Adelman and Cousins, 1990, Roller et al., 1995). Two were used to determine early-age flexural properties. For the other two girders a deck slab was added. One of these composite sections was subjected to a static load, approximating the in-service design dead load, for a duration of 18 months. The other was subjected to 5 million fatigue cycles. It was concluded from these studies that AASHTO provisions for calculating creep and shrinkage prestress losses might be overly conservative for high strength concrete.

#### **1.4.3.11 Overseas HPC Bridge Projects**

The use of high strength concrete for bridges has received much wider and earlier acceptance in Europe and Japan. A summary of the earlier bridges built using HPC is given in the FHWA State-Of-The-Art Report (Zia et al., 1997) and will not be duplicated here. Japan constructed one of its first bridges using high strength concrete as early as 1968. France and

Norway have also led the way in research of HPC and construction of several HPC bridges in the 80's and the 90's. Many of the early bridges used concrete strengths that were significantly lower than those used in some of the present day designs.

#### **1.4.3.12 Missouri's HPC Girder Instrumentation and Monitoring Program**

It is the objective of Missouri's instrumentation project to monitor the performance of a standard AASHTO I-girder bridge when designed and built using HPC in the girders. While the importance of using new shapes and larger prestressing strands is recognized, it is felt that HPC will be implemented, at least initially, using traditional design methods. It is with the purpose of examining the performance HPC in traditional girder shapes and with traditional 0.5" (12.7 mm) diameter prestressing strands that the experimental program described in this report was carried out.

At the time this instrumentation program was undertaken to examine the performance of an HPC I-girder bridge using MODOT type girders and standard 0.5" (12.7 mm) diameter prestressing strands, no published information was available for such girders (Eatherton, 1999). The instrumentation program described here fills a gap in the research literature.

#### **1.4.4 Creep and Shrinkage Response of HPC**

Time dependent effects such as creep, shrinkage, and relaxation have significant influence on the long-term behavior of prestressed concrete bridges. One of the objectives of the research program described here was to investigate the effect of creep and shrinkage on HPC girder bridge A5529 and compare the results to prediction models. The following sections describe creep and shrinkage effects, models for predicting them, and the comparison of creep and shrinkage of HPC compared to NSC, as found in the literature.

##### **1.4.4.1 Creep Behavior**

Increase in strain over time due to a sustained stress is termed creep. Creep can be split into two components (Gilbert, 1988). Basic creep is the time-dependant deformation when the specimen undergoes no drying. The additional creep that occurs in a drying specimen subjected to sustained loading is referred to as drying creep. Total creep is computed as the sum of basic and drying creep. The mechanisms for creep in concrete are not fully understood. Generally creep has been attributed to events occurring in the cement gel such as viscous flow, seepage, delayed elasticity and microcracking.

There are several geometric, mix design, and environmental factors affecting creep, not to mention the interaction of creep with other time dependent effects such as shrinkage and relaxation. The following are some of the factors affecting creep of concrete (Bazant and Wittmann, 1982, Gilbert, 1988):

- Level of sustained load
- Water/cementitious materials ratio
- Aggregate/paste ratio
- Age at time of loading
- Relative humidity
- Temperature
- Member size (volume/surface ratio)
- Reinforcement content

There are several models to predict creep in concrete. The model that is presented here is the ACI 209 method, which is based on a hyperbolic function to represent the creep-time relationship (ACI 209, 1992)

$$\epsilon(t) = \frac{\sigma_o}{E_c(\tau)} + \phi(t, \tau) \frac{\sigma_o}{E_c(\tau)}$$

$$\phi(t, \tau) = \frac{(t-\tau)^{0.6}}{10 + (t-\tau)^{0.6}} \phi^*(\tau)$$

, where

the terms used in the above equations include:

$\sigma_o$  = Applied stress,  $E_c(\tau)$  = Modulus of elasticity at the time of loading,  $t$  = Time at loading (days),  $t - \tau$  = The duration of loading (days),  $\phi(t, \tau)$  = Creep – time relationship, and  $\phi^*(\tau)$  = Ultimate creep coefficient =  $2.35 \gamma_1 \gamma_2 \gamma_3 \gamma_4 \gamma_5 \gamma_6$

$\gamma_1$  = Correction factor for loading age =  $1.25 \tau^{-0.118}$  (for moist-cured concrete)

=  $1.13 \tau^{-0.094}$  (for steam-cured concrete)

$\gamma_2$  = Correction factor for the effect of variations in the relative humidity,  $\lambda$  (in percent):

=  $1.27 - 0.0067 \lambda$  for  $\lambda > 40$

$\gamma_3$  = Correction factor for the size and shape of the member based on the average thickness  $h_o$

when  $h_o \leq 150$  mm:

$h_o$ (mm)	50	75	100	125	150
$\gamma_3$	1.30	1.17	1.11	1.04	1.00

when  $150 \text{ mm} < h_b < 380 \text{ mm}$ :

$$\gamma_3 = 1.14 - 0.00092 h_b \text{ when } t - \tau \leq 365 \text{ days}$$

$$\gamma_3 = 1.10 - 0.00067 h_b \text{ when } t - \tau > 365 \text{ days}$$

when  $h_b \geq 380 \text{ mm}$ :

$$\gamma_3 = \frac{2}{3} [1 + 1.13 e^{-0.0213 V/S}] \text{ (where } (V/S) : \text{ volume to surface area ratio)}$$

$\gamma_4$  = Correction factor for the composition of the concrete based on the slump of the fresh concrete,  $s$ , in mm:  $= 0.82 - 0.00264 s$

$\gamma_5$  = Correction factor for the composition of the concrete based on the ratio of the fine aggregate to total aggregate by weight,  $\psi$  (in percent):  $= 0.88 - 0.0024 \psi$

$\gamma_6$  = Correction factor for the composition of the concrete based on the air content of the concrete,  $a$  (in percent):  $0.46 - 0.09 a < 1.0$

#### 1.4.4.2 HPC Creep versus NSC Creep

It has been found that the specific creep and therefore the creep coefficient value are less in high strength concrete than in normal strength concrete (Mailer, 1992, Han, 1996, Nawy, 1996). Table 1.1 shows the creep coefficients for several strengths of concrete that Nawy reports. It is seen from this data that the creep coefficients for HSC can be as low as half of the creep coefficient for NSC.

**Table 1.1 Ultimate creep coefficient,  $C_u$  (from Nawy, 1996)**

Type of Concrete	$f_c$ psi (MPa)	$C_u$	$C_{u,HSC} / C_{u,NSC}$
Low Strength	3,000 (20.7)	3.1	1.0
Medium Strength	4,000 (27.6)	2.9	0.94
Medium Strength	6,000 (41.4)	2.4	0.77
High Strength	8,000 (55.2)	2.0	0.65
High Strength	10,000 (69.0)	1.6	0.52

Han (1996) conducted an extensive experimental program and analysis of current creep prediction models. It was concluded from his research that the creep deformation of HSC loaded at an age of 28 days are generally much smaller than that predicted by ACI-209. It is also concluded that for any given stress-strength ratio, the specific creep is lower for higher strength concretes. Han also concludes that the shape of the AFREM formulation fits the experimental data much better than ACI-209 but predicts values of creep that are somewhat too low.

In a review of the literature, Malier (1992) concludes that the drying creep is greatly reduced with high performance concrete, especially when silica fume is used. It is also concluded that the basic creep of HPC stabilizes much faster than that of ordinary concrete.

#### 1.4.4.3 Shrinkage Strains

Shrinkage can be defined as the time-dependent strain measured at constant temperature in an unloaded and unrestrained specimen. Shrinkage of concrete can be divided into two types, autogenous shrinkage and drying shrinkage. Autogenous shrinkage is the reduction in volume due to the hydration of cement. Drying shrinkage is the reduction in volume due to the loss of water. Due to much lower permeability, it is obvious that the drying shrinkage characteristics of HPC would be different from NSC.

The water content is probably the largest single factor influencing the shrinkage of cement paste and concrete. Tests have shown that for cements having normal shrinkage characteristics, the shrinkage of the cement paste varies directly with the water – cement ratio (ACI 209, 1992). Therefore it is clear that with low w/c ratios and less water content HPC will have different shrinkage characteristics from NSC. Some of the factors affecting the magnitude of shrinkage in concrete include (Bazant and Wittmann, 1982, Gilbert, 1988):

- Aggregate content, modulus, and surface
- Water/cementitious materials ratio
- Member size/shape (volume/surface ratio)
- Ambient humidity
- Ambient temperature
- Admixtures
- Reinforcement content
- Type of cement
- Carbonation

There are several models for the prediction of shrinkage in concrete. The following is a description of the ACI-209 model:

moist cured concrete: 
$$\epsilon_{sh}(t) = \frac{t}{35 + t} \epsilon_{sh}^*$$

steam cured concrete: 
$$\epsilon_{sh}(t) = \frac{t}{35 + t} \epsilon_{sh}^*$$

where the terms are defined as:

t = Elapsed time (days)

$\epsilon_{sh}^*$  = Ultimate shrinkage as time tends to infinity

$$\epsilon_{sh}^* = 780 \gamma_1 \gamma_2 \gamma_3 \gamma_4 \gamma_5 \gamma_6 \gamma_7$$

$\gamma_1$  = Correction factor for the effect of variations in the relative humidity,  $\lambda$  (in percent):

$$\gamma_1 = 1.40 - 0.01 \lambda \quad \text{for } 40 \leq \lambda \leq 80$$

$$\gamma_1 = 3.00 - 0.03 \lambda \quad \text{for } 80 < \lambda \leq 100$$

$\gamma_2$  = Correction factor for the size and shape of the member based on the average thickness  $h_0$

when  $50 \text{ mm} \leq h_0 \leq 150 \text{ mm}$ :

$h_0$ (mm)	50	75	100	125	150
$\gamma_2$	1.35	1.25	1.17	1.08	1.00

when  $150 \text{ mm} < h_0 \leq 380 \text{ mm}$ :

$$\gamma_2 = 1.23 - 0.0015 h_0 \quad \text{when } t \leq 365 \text{ days}$$

$$\gamma_2 = 1.17 - 0.0011 h_0 \quad \text{when } t > 365 \text{ days}$$

when  $h_0 > 380 \text{ mm}$ :

$$\gamma_2 = 1.2 e^{-0.0472 V/S} \quad (\text{where } (V/S) : \text{volume to surface area ratio})$$

$\gamma_3$  = Correction factor for the composition of the concrete based on the slump of the fresh concrete, s, in mm =  $0.89 - 0.00161 s$

$\gamma_4$  = Correction factor for the composition of the concrete based on the ratio of the fine aggregate to total aggregate by weight,  $\psi$  (in percent):

$$\gamma_4 = 0.30 - 0.014 \psi \quad \text{for } \psi \leq 50\%$$

$$\gamma_4 = 0.90 - 0.002 \psi \quad \text{for } \psi > 50\%$$

$\gamma_5$  = Correction factor for the composition of the concrete based on the air content of the concrete, a (in percent):  $0.95 - 0.008 a$

$$\gamma_6 = \text{Correction factor for the cement content, } c \text{ (kg/m}^3\text{): } 0.75 - 0.00061 c$$

$$\gamma_7 = \text{Correction factor for the variation in the period of initial moist curing } T_c \text{ (in days):}$$

T <sub>c</sub> (days)	1.0	3.0	7.0	14.0	28.0	90.0
γ <sub>7</sub>	1.2	1.1	1.0	0.93	0.86	0.75

The Prestressed Concrete Institute (PCI) stipulates for standard conditions an average value of nominal ultimate shrinkage strain,  $\epsilon_{sh}^* = 820 \times 10^{-6}$  in/in.

#### 1.4.4.4 HPC Shrinkage versus NSC Shrinkage

It has been found that the drying shrinkage of high performance concrete is smaller than that of normal strength concrete. The drying shrinkage strain in high strength concretes with different mineral pozzolanic cementitious replacements was shown to be  $540-610 \times 10^{-6}$  in/in at 1200 days as compared to NSC which recorded a value of  $930 \times 10^{-6}$  (Nawy, 1996). The high strength concretes had w/cm ratios between 0.22 and 0.28 while the NSC concrete had a W/C ratio of 0.57. It was found that the incorporation of additional cementitious materials in the mix such as fly ash and slag significantly reduces the drying shrinkage, with the silica fume being relatively more effective.

Malier (1991) presents the results of a study in which the shrinkage of a high performance concrete ( $f'_c = 14.6$  ksi, 101 MPa) was compared to a control concrete. The HPC exhibited a total shrinkage of  $340 \times 10^{-6}$  in/in while the NSC exhibited a total shrinkage of  $650 \times 10^{-6}$  in/in. Similar sealed specimens were monitored to examine the autogenous shrinkage of the specimens. The autogenous shrinkage of the HPC was  $220 \times 10^{-6}$  in/in while this value was  $120 \times 10^{-6}$  for the NSC. The drying shrinkage would therefore be  $120 \times 10^{-6}$  for the HPC and  $530 \times 10^{-6}$  for the NSC.

Han (1996) conducted a series of shrinkage tests on HPC. It was also found in his studies that autogenous shrinkage plays a much larger role in the overall shrinkage of HPC than it does in NSC. Most of the autogenous shrinkage occurs in the early age of the concrete and this is exhibited in the shape of the shrinkage – time relationship. As a result the overall shape of the shrinkage history of HPC is generally different than that of NSC. HPC undergoes a greater initial rate of shrinkage than NSC but has a tendency to plateau quicker. The standard shrinkage model (ACI 209, 1992) does not accurately portray this shape of the shrinkage-time relationship or the final magnitude of the shrinkage strain for typical HPC mixes.

## **2. EXPERIMENTAL PROGRAM**

### **2.1 Field Instrumentation**

#### **2.1.1 General Information on Instrumentation**

##### **2.1.1.1 Instrumented Cross-Sections**

All of the instrumentation was placed in four of the twenty girders of Bridge A5529. One exterior and one adjacent interior girder of the first and second spans were monitored. Figure 2.1 shows the instrumented girders in a plan view of Bridge A5529.

Each of the four selected girders was instrumented at two cross-sections. The cross-sections are located at the mid-span of the girder and at the end close to Bent 2. The cross-section close to Bent 2 is at a distance of 54" from the girder end (approximately equals the depth of the girder).

In addition to the instrumented cross-sections, two stirrups in each of these four girders were instrumented. Instrumentation was also placed in the diaphragm at Bent 2. The locations and details of the stirrup instrumentation are in the Section 2.1.2.4. The diaphragm instrumentation consists of four strain-gaged bars and 3 thermocouples. The locations and details of the diaphragm instrumentation are included in the Section 2.1.1.4.

##### **2.1.1.2 Cross-Section Instrumentation**

Each cross-section contains three types of gages in the following quantities: 4 strain-gaged bars, 4 vibrating wire strain gages, and 8 thermocouples. As shown in Figure 2.2, the strain-gaged bars and vibrating wire strain gages were placed together in every gage location. The redundancy of the gages serves several purposes.

As described in the following sections, the strain-gaged bar is suitable for short-term incremental and dynamic strain measurements. The vibrating wire strain gage is suitable for long-term measurements. However, as it takes sufficiently long to read, it is less suited for short-term dynamic strain events like transfer of prestress, transportation strains, or crawl-speed load tests. Results from the two systems can be compared for quasi-static strain events. This redundancy also provides an important check by measuring strain by two different types of transducers at the same location.

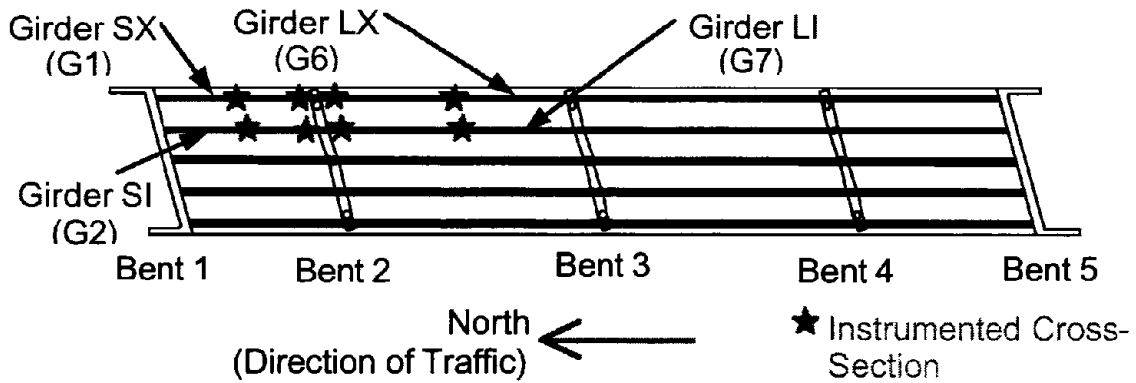


Figure 2.1 Plan view of Bridge A5529 showing instrumented girders

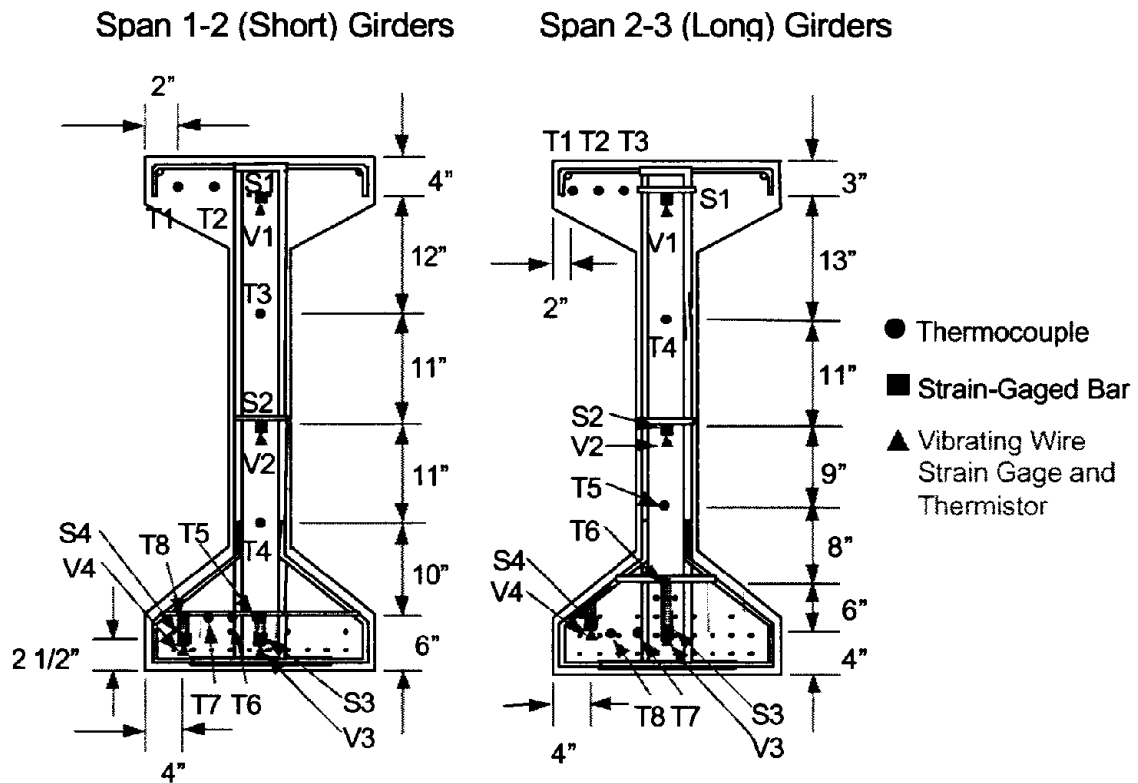


Figure 2.2 Instrumented cross-sections showing location of gages

Three strain-measuring locations were chosen to facilitate monitoring of strain gradients along the depth of the girder. A fourth strain location in the bottom flange provided additional information. The temperature sensors were arranged to obtain a temperature gradient in the top flange, bottom flange and along the depth of the girder. The gage locations in the cross-sections of both girders are shown in Figure 2.2.

### **2.1.1.3 Instrumentation Labeling**

The four instrumented girders are identified by two methods. The identification system used by Egyptian and Pace Construction started with the northeast girder, which is in Span 1-2, as G1. The rest of the girders in Span 1-2 were numbered as G2-G5. The girders in Span 2-3 were also numbered from east to west as G6-G10. Span 3-4 and Span 4-5 were numbered similarly up to G20. The instrumented girders are girders G1 and G2 in Span 1-2 and girders G6 and G7 in Span 2-3.

The more informative identification system used by the MU research team is detailed below. The exterior girder in Span 1-2 was labeled as girder SX for “short exterior” girder. The interior girder in Span 1-2 was labeled as girder SI for “short interior” girder. The exterior girder in Span 2-3 was labeled as girder LX for “long exterior” girder. The interior girder in Span 2-3 was labeled as girder LI for “long interior” girder. The instrumented girders shown in Figure 2.1 are identified according to the above system.

Labeling also identified a particular instrumented cross-section, since each girder was instrumented at the end and mid-span cross-section locations (the letters E and M were appended to the girder identification). For example LXE is the “end” cross-section in the “long exterior” girder (G6).

The gages within each cross-section were further identified by type and location in the cross-section. Vibrating wire strain gages were labeled as V, strain-gaged bars were labeled as S, and thermocouples were labeled as T. The location number is defined on the individual cross-section diagrams, Figure 2.2.

The instrumented stirrups were identified first by the girders in which they were contained. Additionally, notation of N for near (from Bent 2) and F for far was appended to identify the two stirrups in each instrumented girder. The number 1 was included after the hyphen to specify that the strain gage location on the stirrup was at the mid-height of the girder. The number 2 denotes that the strain gage location on the stirrup was  $\frac{3}{4}$  of the way up the girder

depth, Figure 2.3. An example would be LIF-2, which represents the gage  $\frac{3}{4}$  of the way up the long interior girder (G7) at the end far from bent 2. The strain-gaged bars in the diaphragm were labeled as DIA. The instrumentation was then labeled as strain-gaged bar (S) or thermocouple (T) and with a number which describes its location, Figure 2.4. The exact location of the diaphragm bars is discussed in the next section.

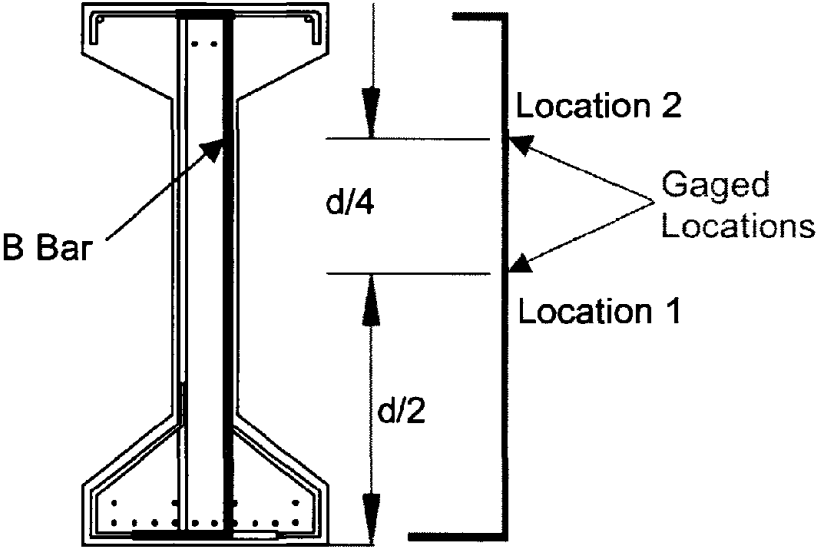


**Figure 2.3 Schematic showing gage locations in an instrumented stirrup**

**2.1.1.4 Diaphragm Instrumentation**

The diaphragm at Bent 2 was instrumented with four strain-gaged bars and three thermocouples. The locations of the instrumentation are shown in Figure 2.4 along with the end cross-section gages and instrumented stirrups. The diaphragm instrumentation was located near the interior girders in Bent 2.

One of the main objectives of the diaphragm instrumentation was to examine if these could be used to study the continuity provided by the diaphragm. By comparing the diaphragm strain measurements to the end cross-section strain readings of the interior girders, it was anticipated that conclusions could be made about the type and level of continuity of the girders over the bent. As shown in Figure 2.4 the strain-gaged bars are at approximately the same depth for both end cross-sections and the diaphragm.

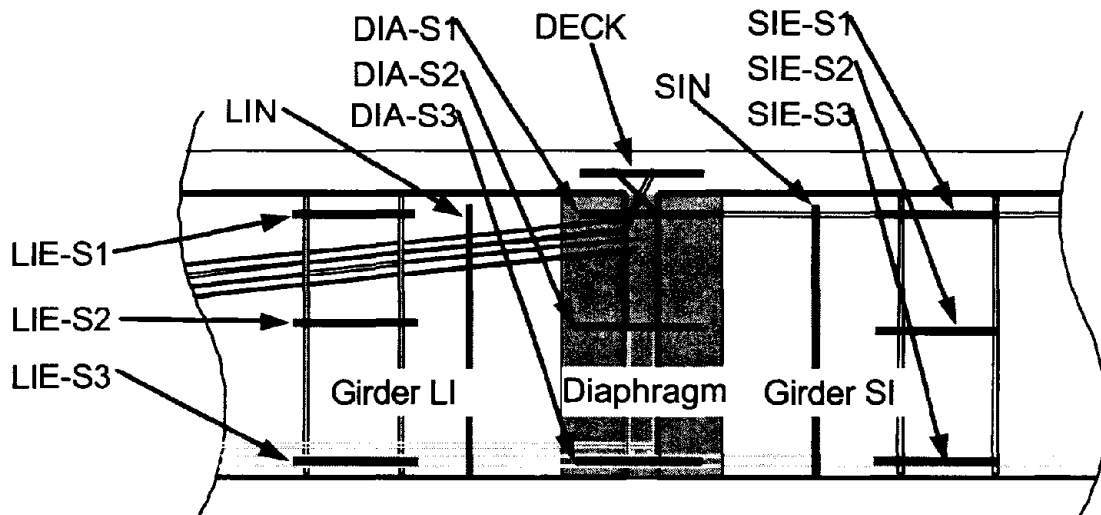


**Figure 2.4 Schematic showing details of the diaphragm instrumentation**

## **2.1.2 Internal Instrumentation**

### **2.1.2.1 Strain-Gaged Bars**

Strain-gaged bars consist of a short length of #4 (nominal diameter = 0.5") reinforcing steel bar with a full bridge of strain gages attached to a machined section in the middle of the bar. The strain-gaged bars were fabricated at the University of Missouri – Columbia. The steel rebar used was Grade 60 used for reinforcing concrete. The bars were cut to 24" lengths except for the diaphragm bars that were 20" long.

Preparation of the strain-gaged bars included cutting the bar to the proper length, machining, strain gage application, waterproofing, and calibration. Waterproofing consisted of several layers of protective materials. This was done to not only keep water out, but also to provide protection against falling concrete during casting. Figure 2.5 shows a strain-gaged bar after instrumenting it and after waterproofing it. By using a full bridge of active strain gages the effects of temperature on measured strains are eliminated.

The instrumented bars were calibrated using a 110 kip capacity MTS machine. The setup consisted of a 20 kip capacity load cell, a universal joint, a coupling apparatus and an extensometer. The universal joint minimizes bending affects for the loading train. The coupling facilitates easy setup and also serves as a safety measure that prevents unanticipated compression loading of the setup. The extensometer has a gage length of 0.5" and was attached to the

instrumented and waterproofed section of the strain-gaged bar. Three cycles of a 0.01 Hz sinusoidal ram displacement-controlled loading was applied during calibration.

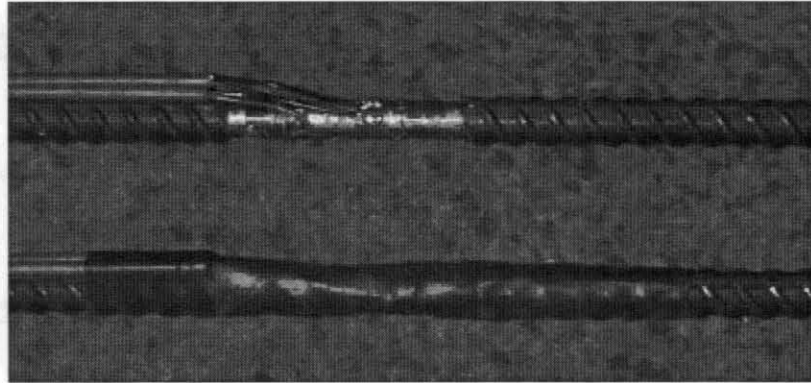


**Figure 2.5 Instrumented strain-gage bar before (top) and after water proofing**

#### **2.1.2.2 Vibrating Wire Strain Gages**

Vibrating wire strain gages made by Geokon, Inc., were used for the project. A photograph of the 6" gage length model VCE-4200 embedment type vibrating wire strain gage is shown in Figure 2.6.

The vibrating wire strain gage involves a wire that is stretched between two flange plates. Displacement of one flange relative to the other causes the tension in the wire to change. The change in wire tension is then measured as a change in the resonant frequency of the wire. Electromagnetic coils, which are housed in a plastic block, are positioned around the center part of the gage. By sending an alternating current through the coils at a range of frequencies, the taut wire is excited. After sweeping the range of frequencies the wire continues to vibrate at its resonant frequency. The electromagnetic coils then pick up the signal as an alternating current induced by the wire vibrations. The frequency of the alternating current is measured and correlated to strain. The strain in the gage is directly proportional to the square of the resonant frequency.

The length of the wire, however, also changes with temperature and as a result the tension, natural frequency, and strain measurement are dependent on temperature. A correction for this effect is provided by the manufacturer, which uses the coefficient of linear thermal expansion of steel (wire material).

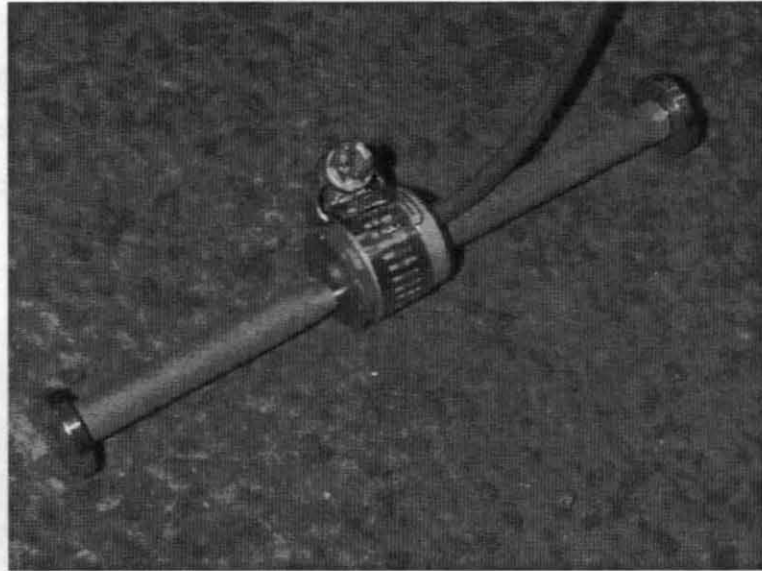


**Figure 2.6 Vibrating wire gage**

Since the vibrating wire strain gage is based on the natural frequency of a wire, instead of a resistance like the strain-gaged bar, the vibrating wire strain gage can be used to measure long-term strain events (no drifts or electrical noise unlike resistance gage based transducers).

Each vibrating wire strain gage includes a thermistor which measures temperature using a temperature related change in resistance. The thermistors are included with the electromagnetic coils in the plastic block so that the strain reading can be corrected for the effects of temperature.

The gages were all calibrated individually on a 110 kip capacity MTS machine. Three LVDTs configured at 120° from each other were used for monitoring the actual strain applied. This minimized adverse effects from possible eccentric loading. Specially designed recessed load platens were used to hold the gage in place. Three cycles of 0.01 Hz sinusoidal ram displacement-controlled loading was applied. A correlation was then obtained between strain applied and the square of the natural frequency of the vibrating wire gage.

### **2.1.2.3 Thermocouples**

Type T thermocouples were used (copper-constantan junction). The wires were 24 gauge Teflon coated thermocouple wires. The Type T thermocouple is rated for a temperature range of -328° to 662° F (-200° to 350° C), which covers the anticipated range of temperatures.

The thermocouple wires were cut to the estimated length from the gage location to the terminal box. They were then welded together at the University of Missouri – Columbia using

proper thermocouple welding equipment. They were then labeled using heat shrink label on both ends of the thermocouple wire. The welded thermocouple end was then dipped in epoxy and set out to dry. The epoxy was a safety measure to protect the thermocouple connection. Figure 2.7 shows a photograph of the thermocouples set out to dry after epoxy was applied to the thermocouple junctions.



**Figure 2.7 Thermocouples after welding, labeling and sealing**

To use a thermocouple, the temperature of the connection between the thermocouple wire and terminals must be known. The temperature at the thermocouple terminals is referred to as the cold junction reference temperature. The reference temperature was measured in the terminal boxes using a temperature sensor. More details of the reference temperature measurement are included in the Section 2.1.3.2.

#### **2.1.2.4 Instrumented Stirrups**

Several “B Bars” of the actual shear reinforcement typically used in prestressed girders were obtained from Egyptian Concrete Co. and instrumented before girder fabrication. A diagram of the girder with the B bar labeled is shown in Figure 2.3.

During fabrication of the girders these instrumented stirrups were installed in designated locations, in place of the normal stirrups. The B bar stirrups were instrumented similarly to the strain-gaged bars, but in two locations along the bar. The B bar was instrumented at the mid-

height of the girder and  $\frac{3}{4}$  the height of the girder as shown in Figure 2.3. These were the expected locations for maximum shear stress in the girder by itself and when acting composite with the deck slab, respectively. Calibration tests were conducted on the instrumented stirrups using static dead loads.

The instrumented stirrups at the end near Bent 2 in both Span 1-2 and Span 2-3 were located approximately 27" distance from the end of the girder which is half the depth of the girder. The instrumented stirrups at the end away from Bent 2 in Span 1-2 and Span 2-3 were located at a distance approximately equal to the depth of the girder which is 54". The location of the instrumented stirrups in relation to the other stirrups and the end of the girders is shown in Figure 2.8 and Figure 2.9.

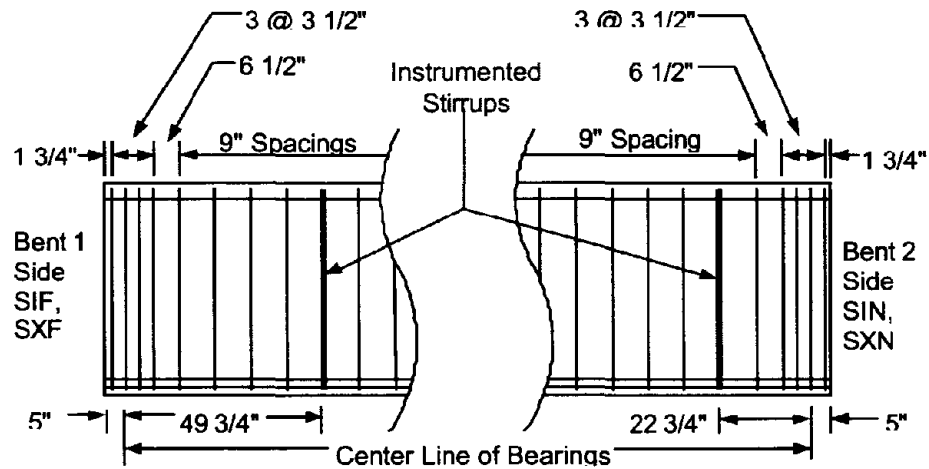


**Figure 2.8 Location of instrumented stirrup reinforcement in Span 1-2 girders**

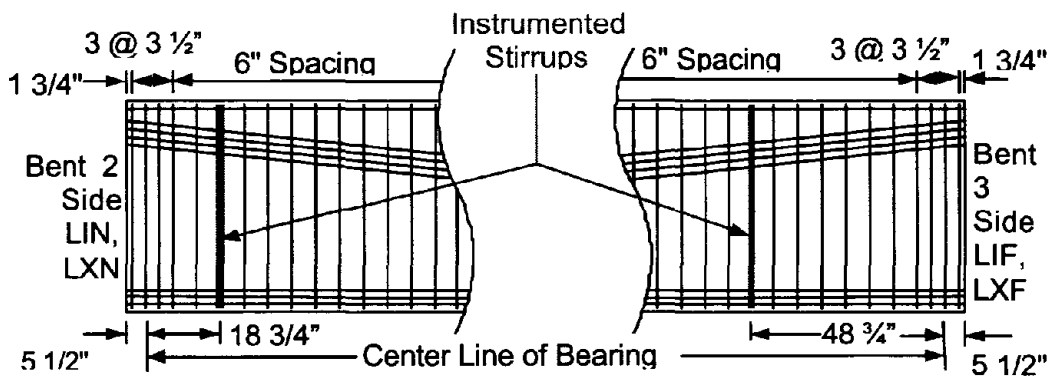


**Figure 2.9 Location of instrumented stirrup reinforcement in Span 2-3 girders**

### 2.1.2.5 Preparation of Instrumentation Clusters

The instrumentation clusters were laid out on the lab floor and grouped according to the cross-section for which they were intended. All gages were checked to ensure that they were operating properly. Figure 2.10 highlights the scope of the instrumentation program. The wire length for every gage was individually estimated such that there would not be slack in the wires when installed.



**Figure 2.10** Instrumentation and associated wires being readied for placement in the girder molds at the precasting site

Wooden spacers were used to hold the vibrating wire strain gage to the strain-gaged bar. The spacers kept the flanges of the vibrating wire strain gages from touching the strain-gaged bars. The centerline of the vibrating wire strain gage was one inch below the centerline of the strain-gaged bar as a result of the spacers. Plastic wire ties held the assembly together. This detail can be seen in Figures 2.11 and 2.12.

The instrumentation was tied into the existing reinforcement in several ways. As shown in Figure 2.11 some gages were tied to the prestressing strands using wire ties. In some places hanger bars were used. As shown in Figure 2.12, the hanger bars were short lengths of #4 bar and were tied into the shear reinforcement. The instrumentation was then tied to the hanger bars.

The thermocouples were wire tied to the appropriate stirrups. The thermocouples are shown in Figures 2.11 and 2.13 (the white label on the thermocouple wire can be seen).

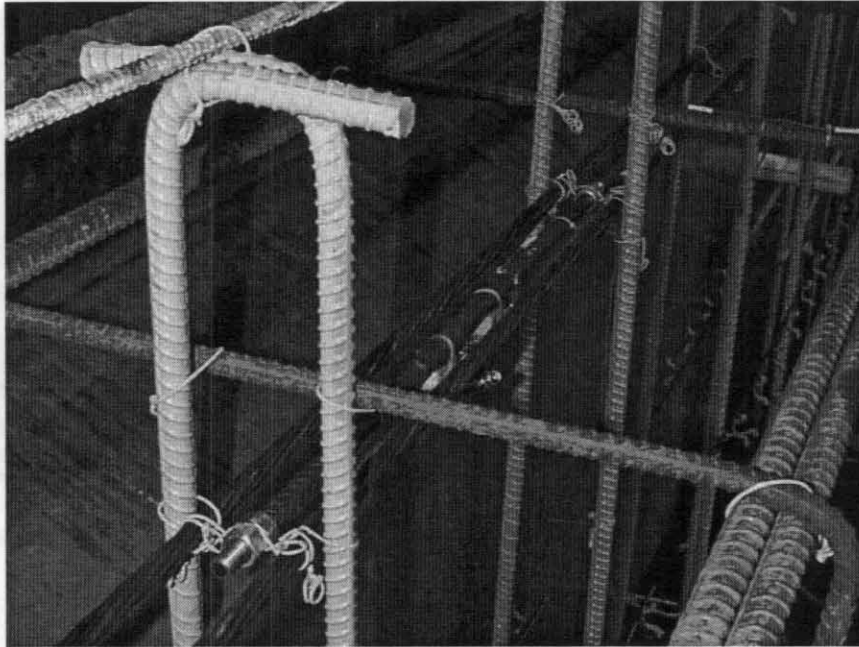


**Figure 2.11** Top flange instrumentation showing instrumented strain-gaged rebar and vibrating wire gage

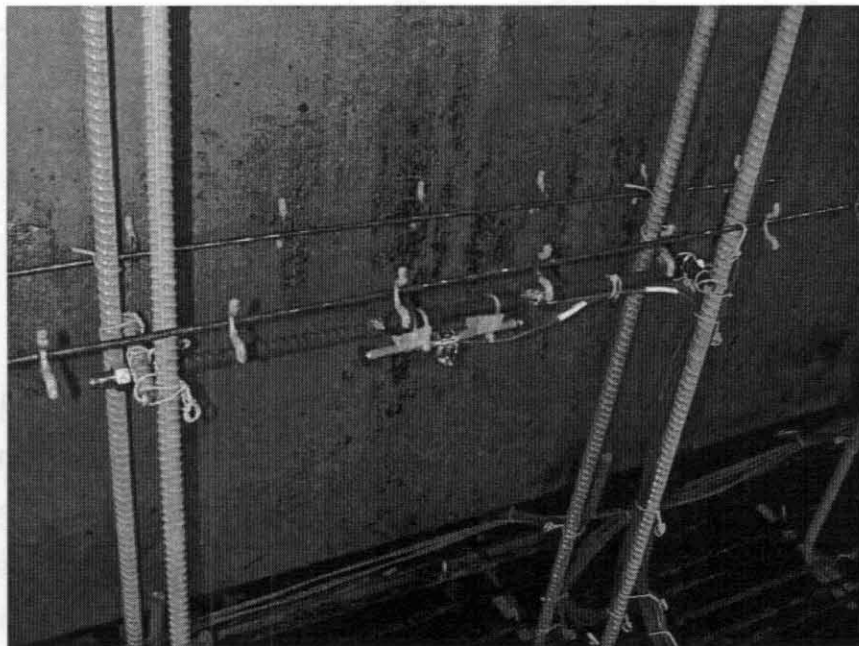


**Figure 2.12** Web instrumentation at midheight attached to stirrups

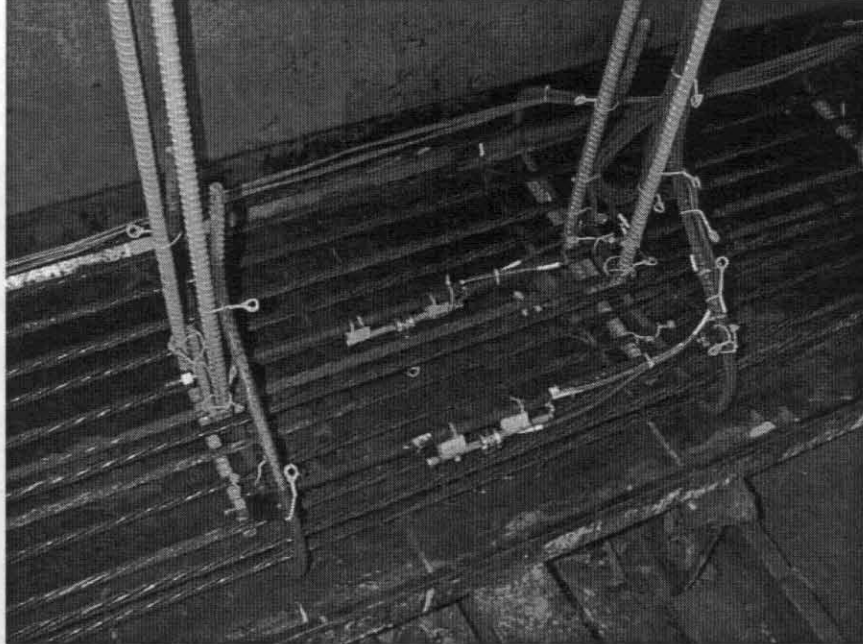


**Figure 2.13** Bottom flange instrumentation showing instrumented strain-gaged rebar and vibrating wire gage

The end of one of the Span 1-2 (short) girders is shown in Figure 2.14. The instrumented end cross-section is shown on the left side of the figure, and the instrumented stirrup is shown just right of center. The bundles of wires coming from each cross-section were tied together and tied to the shear reinforcement in the bottom flange. The bundles of wires were positioned to come out of the girder end at the top. This was done so that after erection the wires exited the girders into the diaphragm. The wires were then routed through the diaphragm to exit the bridge on the north side of Bent 2, in between the interior and exterior girders.

### **2.1.3 Data Acquisition System**

#### **2.1.3.1 General Information**

Approximately two hundred pieces of instrumentation were embedded in the four-instrumented girders. To efficiently take a large number of meaningful measurements and keep the data acquisition system economical was a challenge. The instrumented girders were cast two at a time. Recording temperature gradients and temperature extremes during casting and curing operations was a priority. During the load test it was necessary to take only strain readings. There was a need, therefore, for flexibility in the data acquisition system to allow for changes in the parameters being monitored at specific stages in the life of the girder. During casting, curing,

transport, and erection it was also necessary to be able to attach the data acquisition system to the girders quickly and switch between the girders easily. It was with these goals that the data acquisition system and associated programs were developed.



**Figure 2.14** Photograph of the girder showing the end cross-section instrumentation, instrumented stirrup, and wire bundles

The lead wires from the gages were routed into terminal boxes. One terminal box was dedicated to each girder. Cables with detachable connectors were used to connect the terminal boxes to the data acquisition box. A datalogger and multiplexers housed in the data acquisition box were used to provide excitation and monitor the outputs from the instrumentation.

#### **2.1.3.2 Terminal Boxes**

The terminal boxes served several purposes. First it was necessary to route all of the instrumentation leads efficiently into cables that lead to the data acquisition box. A printed circuit board was fabricated at the University of Missouri – Columbia that had screw terminal posts for connection to the gages and wires. Figure 2.15 shows fabrication of the terminal boxes, when the wires from the connectors are about to be soldered onto the terminal strips. The different gage types were routed into separate cables to minimize electrical noise and facilitate

ease of identification. Three cables were used for each of the four boxes: (i) thermocouples, (ii) strain-gaged bars, and (iii) vibrating wire strain gages / thermistors.

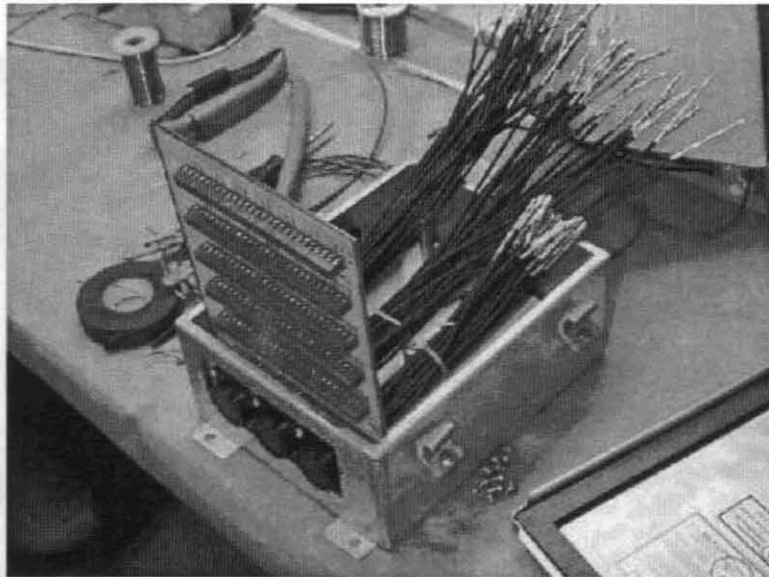


**Figure 2.15 Terminal box undergoing fabrication**

The terminal boxes also served as the cold junction reference for the thermocouple readings. It is necessary to know the temperature of the thermocouple-terminal junction for the thermocouple temperature measurement to be meaningful. A temperature sensor was used to determine the temperature in each terminal box.

A voltage regulator was needed to reduce the 12 Volts from the battery to the 4 Volt excitation used for the strain-gaged bars and the instrumented stirrups. This was accomplished using another circuit within the terminal boxes.

The terminal box enclosure measures 8" x 12" x 4". The leads from the instrumentation were fed through openings in the left side of the terminal box. Clamps were used on the incoming wires to minimize water and bug infiltration. Figure 2.16 shows a finished terminal box.

### **2.1.3.3 Cables and Connectors**

Twelve cables (three for each terminal box) carried the signal wires to the data acquisition box. The cables comprised of 27-pairs of individually shielded wires. The

connectors are 57 pin circular plastic connectors with gold plated pins and sockets. The pins and sockets were individually soldered onto cable wires and pressed into place in the connector.

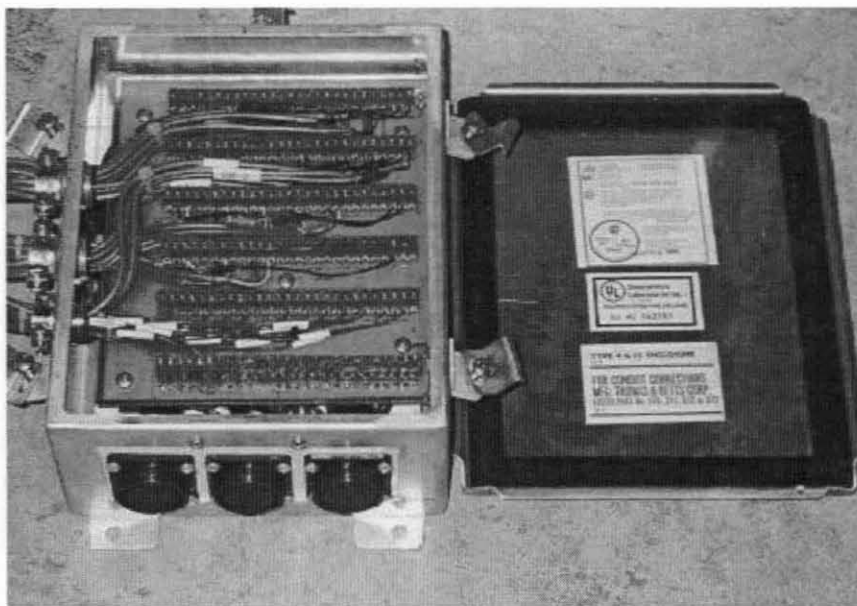


**Figure 2.16 Completed terminal box ready to install**

#### **2.1.3.4 Data Acquisition Box**

The cables from the terminal boxes feed into the data acquisition box through holes in its lower wall. One inch thick aluminum block clamps were tightened onto the cables to provide strain relief and moisture / bug protection. The cables inside the main box were split up into their individual wire pairs. The wire pairs were stripped, tinned and labeled. The individual wire pairs were connected into the multiplexer terminals in different arrangements depending on which gages needed to be monitored. The initial process of connecting wires into the multiplexers is shown in Figure 2.17.

The enclosure, multiplexers, datalogger, battery, and vibrating wire interfaces were obtained from Campbell Scientific, Inc. Three model AM416 relay multiplexers were mounted in the bottom of the data acquisition box. Each multiplexer is capable of multiplexing 32 differential signals into 2 differential outputs. The total number of instruments that can be read at one time is therefore 96, compared to almost 200 gages that were installed. It was decided that it would not be economical to purchase more multiplexers and another datalogger to take

measurements from all pieces of instrumentation at once. With the proper planning and rewiring of the multiplexers it was possible to obtain readings from the gages that were important at any time during the life of the girder. The different multiplexer wiring schemes for different events are described in the Appendix B.

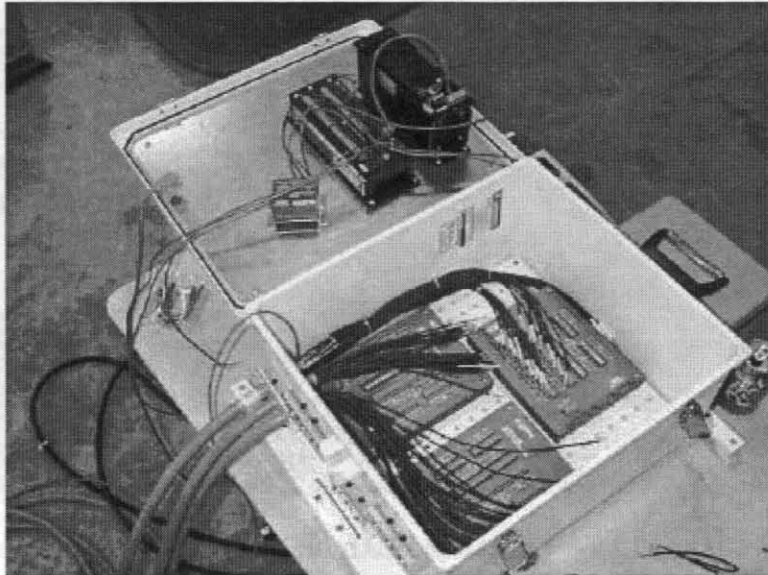


**Figure 2.17** The data acquisition box showing wiring details used for the multiplexers

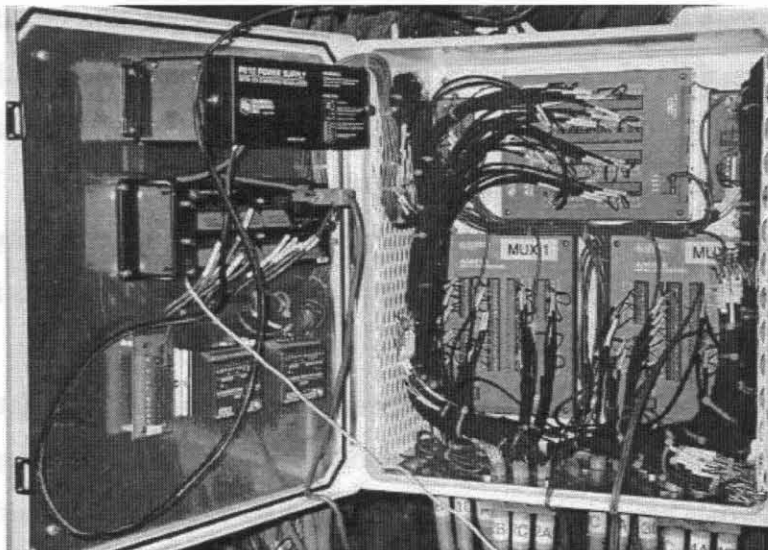


**Figure 2.18** The finished data acquisition box

A relay circuit was built and is shown in the upper right hand side of Figure 2.18. The purpose of this relay circuit is to control when the excitation voltage is applied to the gages. This was necessary to conserve battery power. When a 5 Volt on-voltage is received from a datalogger I/O port, the switch sends the 12 Volt excitation voltages to the terminal boxes. As described in the section on terminal boxes, the excitation voltage is then reduced to 4 Volts in the terminal boxes.

Steel grating was installed on the sides of the data acquisition box to allow easy organization of the unused wires. Extra leads from the cables were bundled and tied neatly to the side grating. An aluminum plate with short stand-offs was attached to the lid of the main data acquisition box. The battery, datalogger, and vibrating wire interfaces were attached to the lid. Although the manufacturer did not intend this use of the enclosure, it allowed for a more efficient use of space. Two sets of extra 12 Volt terminals were installed. These are shown in the lower left side of the lid and the upper right area inside the box in Figure 2.18.

The battery pack used to run the instrumentation system is a model PS12 from Campbell Scientific, Inc. It includes a 12 Volt 7.0 Amp-hour lead acid battery, an AC transformer and a charging circuit. The battery pack is shown at the top of the data acquisition box lid in Figure 2.17. After transport to the site the system was completely dependent on battery power. As a result a larger capacity deep cycle 12 Volt battery was used to power the strain-gaged bars and instrumented stirrups independently of the battery in the data acquisition system.

The datalogger is the CR10X model and is shown right under the battery pack in Figure 2.17. It has 6 differential analog inputs, 8 digital I/O ports, 2 excitation ports, and 3 pulse ports. The CR10X accepts a program from a PC over an RS232 port and then runs independently. Data can be downloaded to a PC or laptop. The datalogger is capable of recording up to 62,000 measurements before downloading is required. The PC208W software provided by Campbell Scientific was used to program as well as download data.

The vibrating wire interfaces (AVW1) are attached below the datalogger in Figure 2.17. These devices provide completion bridges for the thermistors and excitation and signal conditioning for the vibrating wire strain gages.

### **2.1.3.5 Remote Control of Data Acquisition System**

To obtain long-term data from the instrumentation it was necessary to make the system self-sufficient. A way of charging the battery was needed and it was determined that solar panels

were the appropriate solution. Two solar cell arrays obtained from the University of Missouri-Columbia SunTiger solar car team were mounted in an aluminum case. The aluminum case consisted of an 18 1/2 x 43" sheet of 1/8" thick aluminum with 1/2 square aluminum bar outlining the plate. Grooves were machined into the aluminum bar and a rectangle of 1/8" thick tempered glass was sealed into the frame with silicon. A porous fabric pouch containing desiccant was attached inside the frame. The solar arrays are capable of producing an open circuit voltage of 10 Volts each and 20 Volts in series.

The solar panel casing was mounted on an aluminum frame that was attached to the barrier curb on the east side of Bridge A5529. The frame is three feet wide, three feet deep and extends five feet away from the bridge. The frame and the solar panel are shown in Figure 2.19.

The frame is made up of four aluminum angles that converge on an aluminum pipe. The solar panel case was mounted on the aluminum pipe with an assembly that allowed tilting about two axis and rotation in the base pipe. This allowed adequate degrees of freedom and movement to track the sun and obtain maximum recharging capacity.

A controller was designed and built at the University of Missouri – Columbia to connect the solar panel output to the strain gage excitation battery or the datalogger battery when either voltage falls below preset limits. The system was designed so that remote uploading of programs and downloading of data could be carried out using an optional cell phone.

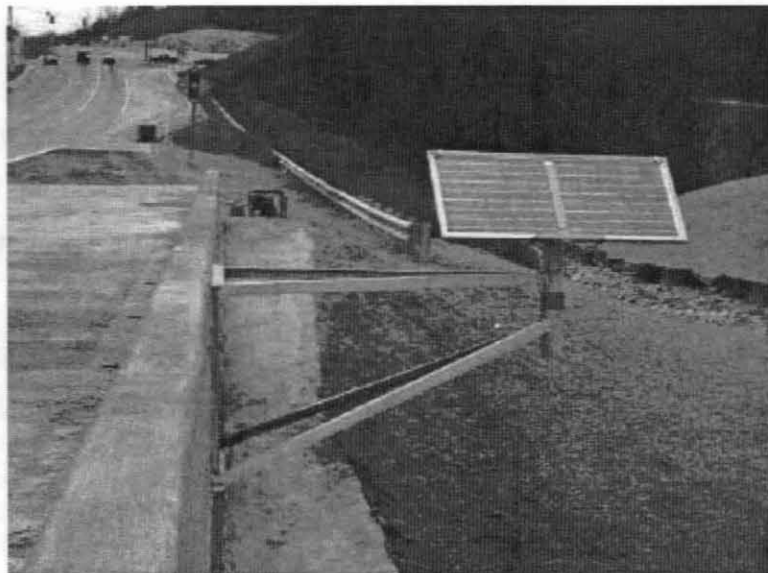


**Figure 2.19** Solar power source for long-term remote data acquisition

## 2.1.4 External Instrumentation

### 2.1.4.1 Deflection Measurements

The deflection device consists of a passive-end plate, a live-end plate with pulley and weight, a piano wire stretched between the two, and several reference angles. The piano wire is 0.020" in diameter.

The passive-end plate is a 5" x 5" x  $\frac{1}{8}$ " steel plate that was painted to protect it from the weather. As shown in Figure 2.20 the piano wire is clamped between two aluminum plates. The plate was epoxied to the top flange of the girders approximately two feet from the end. The clamping plates, bolts, and nuts holding the wire at the passive-end were coated with epoxy so that the wire would not move.

The live-end of the deflection system used a similar 5" x 5" x  $\frac{1}{8}$ " plate epoxied to the top flange of the girder approximately two feet from the end. The live-end plate holds a 2" diameter pulley around which the piano wire was wrapped once before hanging down, attached to a weight. The weight is a block of concrete that weighs approximately 50 pounds. The purpose of the weight and pulley assembly is to maintain a constant tension in the piano wire so that relaxation or temperature change cannot cause a change in the deflected shape of the wire.

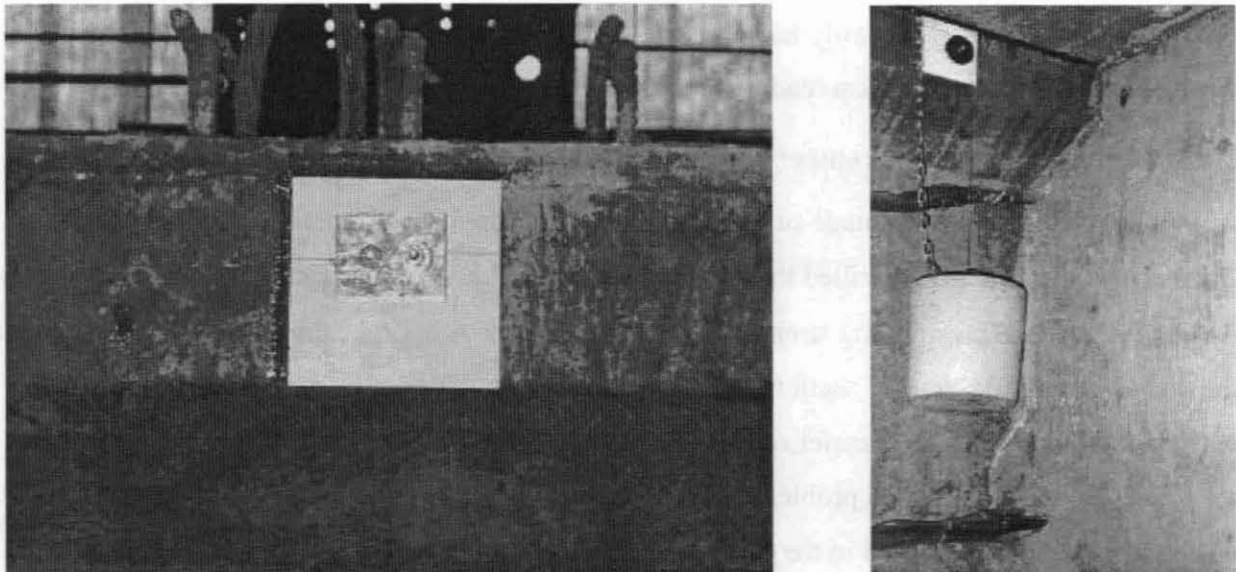


**Figure 2.20** Taut-wire deflection device showing the passive (left) and active (right) ends

Steel angles were used to reference the deflection of the beam relative to the piano wire. The angles were short lengths of steel angle painted and epoxied to the top flange of the girder. Reference angles were placed at the  $\frac{1}{6}$ ,  $\frac{1}{3}$ ,  $\frac{1}{2}$  and  $\frac{3}{4}$  points of each of the four instrumented girders. The deflection measurements were made using a digital caliper as shown in Figure 2.21.

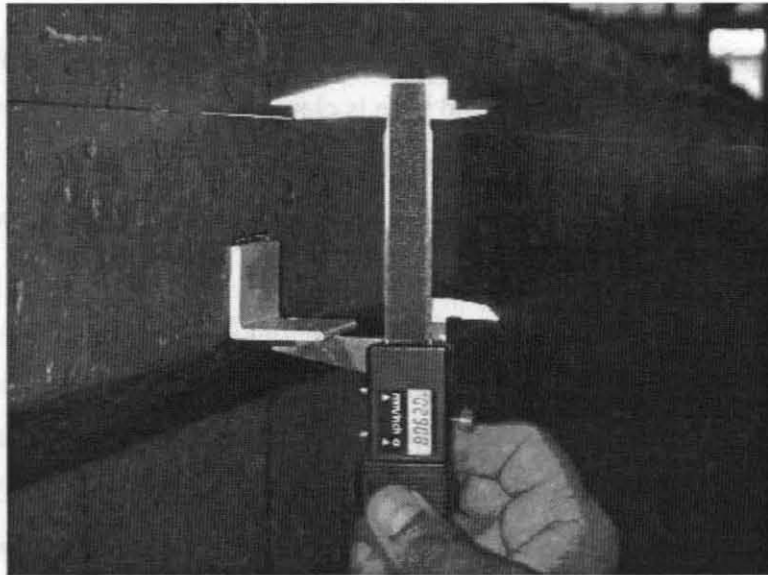


**Figure 2.21 Digital calipers used to measure girder deflections**

Measurements were easily taken before the bridge was constructed. After the girders were installed, taking deflection readings required a man-lift or a thirty-foot ladder.

#### **2.1.4.2 Strand Slip Measurement**

Measurements were made of prestressing strand slip during transfer. A 1" x 1" x 1" channel section with a hole drilled through the legs of the channel was used. The channel section was attached to the prestressing strand using a hose clamp. A digital caliper was used to measure the distance from the channel section, through the holes, to the steel mold. The measurement was made before and after transfer of the prestressing force.

There were numerous problems with the end slip measurement. There is a large amount of elastic strain energy stored in the prestressing strands between the two girders cast, prior to release. When the strands were cut, this energy caused the strands to unravel. As a result, many of the end slip channel sections moved during this rapid release of energy. For the second set of instrumented girders that were fabricated (Span 1-2 short girders) three cable clamps were used

to reduce the amount of movement of the end slip channel sections. This approach still did not work as well as anticipated. The strands, channel sections, and cable clamps are shown in Figure 2.22. The end slip measurement made after transfer is shown in Figure 2.23.

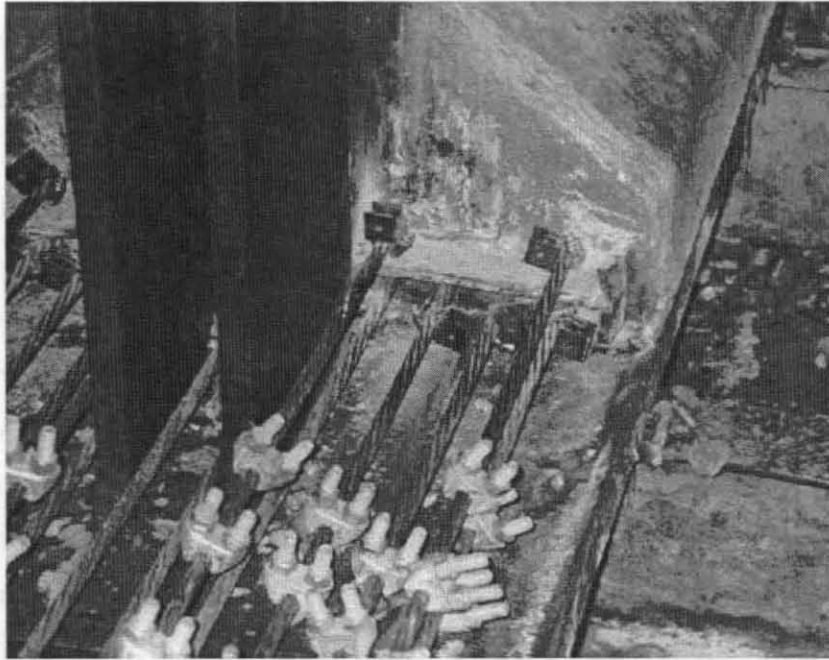


**Figure 2.22** Arrangement for measurement of end-slip

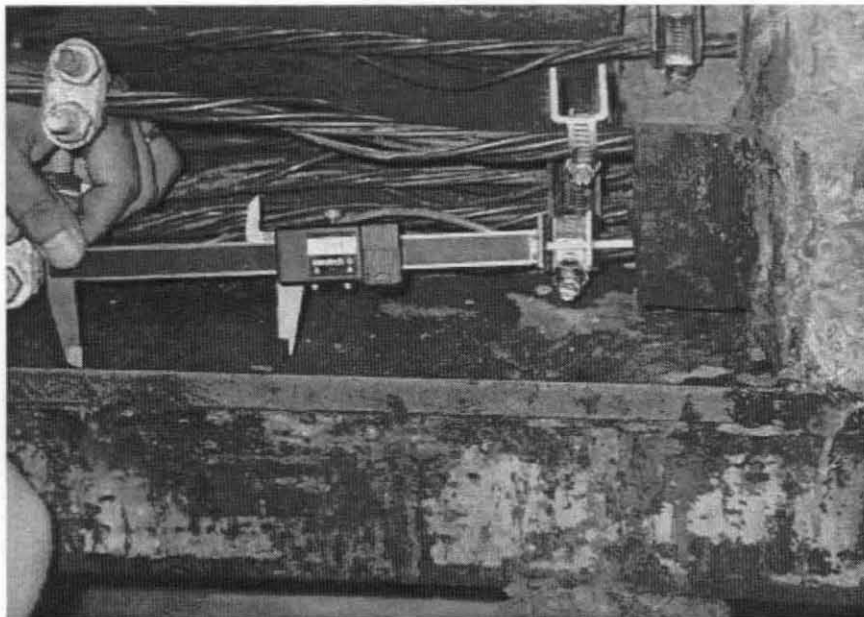


**Figure 2.23** Digital calipers used to make end-slip measurements

Also it was noted that the steel mold separated from the end of the concrete girder in some cases. This could be seen by a small crack between the mold and the concrete. Both of these effects made end slip measurements unreliable.

#### 2.1.4.3 Transfer Length

A Whitmore gage and a row of brass studs were used to determine transfer length. The brass studs are DEMEC points normally used for mechanical surface strain measurement in concrete. A small hole was drilled in one end of the studs for measurement with the Whitmore gage. A calibrated aluminum bar was used to set the brass studs at precise initial gage locations. The bar was epoxied to the girder first and then studs were placed in precisely spaced holes. Screws on the backside of the bar pressed the studs against the concrete while the epoxy set. The studs were epoxied onto the bottom flange of the instrumented girders at a spacing of 2".

Measurements of displacement between brass studs were made using a Whitmore gage. The Whitmore gage used a resolution of 0.0001". The concern regarding use of a Whitmore gage is that the reading is very sensitive to how the measurement is taken. Angle of the gage and position of one's hands affects the reading. Care was taken so that consistency in the reading could be obtained. A photograph showing the transfer length measurement is highlighted in Figure 2.24.



**Figure 2.24** Transfer length measurement being made using the Whitmore gage

Measurements were made at the two-inch intervals, but represent average strain over a ten-inch gage length. A set of readings was taken before and after transfer of the total prestressing force.

#### **2.1.4.4 Thermographic Survey**

A thermographic survey of the Span 1-2 (short girders), instrumented girders was carried out using an infrared video camera. Electrotest Inc carried out the work. An Amber Raytheon infrared camera was used. Figure 2.25 shows personnel from Electrotest Inc. taking infrared video of the girders. The objective of the thermographic survey was to obtain temperature gradients on the exterior surface of the steel girder molds. From this information the location of hot spots and temperature differentials can be established at different times.



**Figure 2.25 Electrotest Inc. personnel recording infrared thermographic video images**

Infrared pictures of half of both Span 1-2 instrumented girders were taken at one-hour intervals for twenty-four hours after casting. Normally during curing at Egyptian Concrete, heavy insulated tarps are laid over the girders. For the halves of the two beams that were being thermographically monitored, light plastic tarps were used instead so they could be lifted to

make infrared measurements. The thermographic images were recorded and then individual digital images were downloaded into the computer.

## 2.2 Laboratory Studies

### 2.2.1 General

The specimens for all laboratory tests carried out at the University of Missouri – Columbia were cast from the first load of concrete used to cast the Span 2-3 (long girders) girders. Figure 2.26 shows the casting of the cylinders, beams, and slabs used in the laboratory tests. Twenty 6” cylinders, six shrinkage test beams, and two 24” x 24” x 6” slabs were cast. The slabs were used for sawing notched beam specimens for fracture properties and for coring 3” compression cylinders.

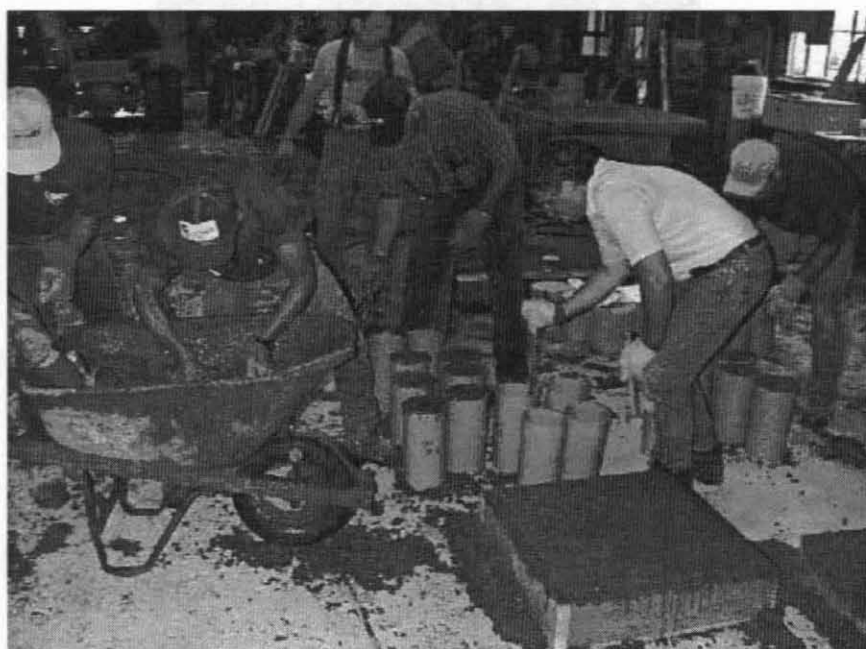


**Figure 2.26 Casting of the cylinders and slabs used for the laboratory tests**

Creep and shrinkage tests were completed on a normal strength concrete (NSC) mix to compare the differences in responses between NSC and HPC mixes. Mix proportion details for both the NSC and HPC mixes are presented in Chapter 3.

## 2.2.2 Compression Tests

### 2.2.2.1 Six Inch Cylinder Test Setup

Due to the large loads required to test a 6" HPC cylinder in compression, it was necessary to carry out these tests at the MoDOT Materials Testing Laboratory in Jefferson City, Missouri. A Forney universal testing machine with a maximum load capacity of 500 kips was used. The load was measured using a pressure transducer on the hydraulic line. The deformation of the concrete cylinder was measured using three LVDTs uniformly spaced around the specimen (120° apart). The LVDTs were attached to an aluminum ring that was clamped to the specimen using three setscrews. The cores of the LVDTs were connected to another aluminum ring that was clamped on the concrete specimen at an eight-inch gage length away from the first ring. The compression setup for tests on 6" cylinders is shown in Figure 2.27. The age at testing was 59 days.

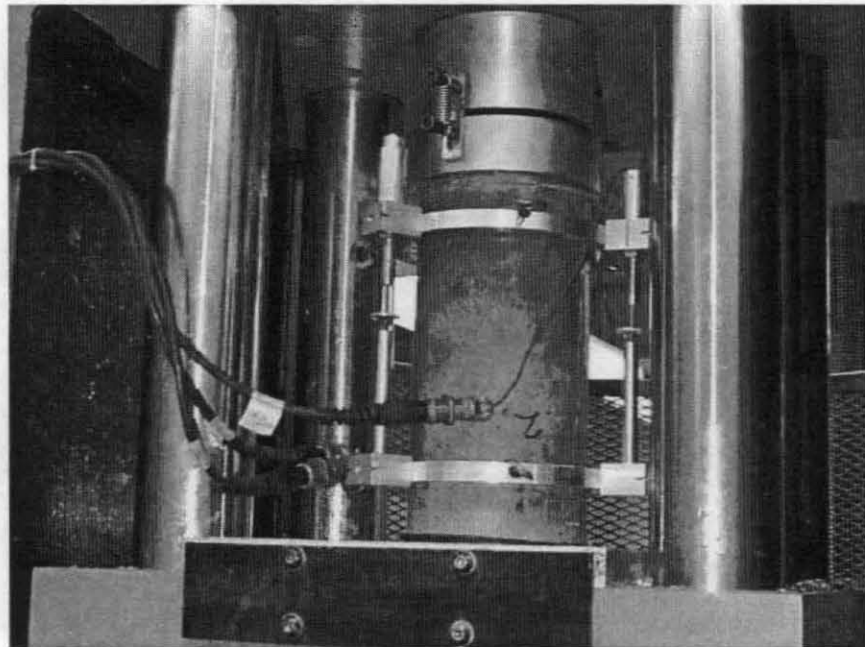


**Figure 2.27** Compression test on 6" diameter cylinder test conducted at the MoDOT Materials Testing Laboratory

### 2.2.2.2 Three Inch Cylinder Test Setup

The compressive tests on three-inch cylinders were carried out using a 110 kip capacity MTS machine. The age at testing was 131 days. The specimens were cored out of the 24" x 24" x 6" slabs. Six 3" cylinders were tested. A 3-LVDT assembly similar to the one used for the 6" cylinders was also used for the 3" cylinder compression tests. The gage length for the LVDTs was 4".

These compression tests were conducted using closed loop control and circumferential strain as the feedback control parameter. This ensures stable fracture and allows post-peak response to be recorded. Load was measured using a 100-kip capacity load cell. Ram displacement was measured using an LVDT. The 3" cylinder compression test set-up is shown in Figure 2.28.

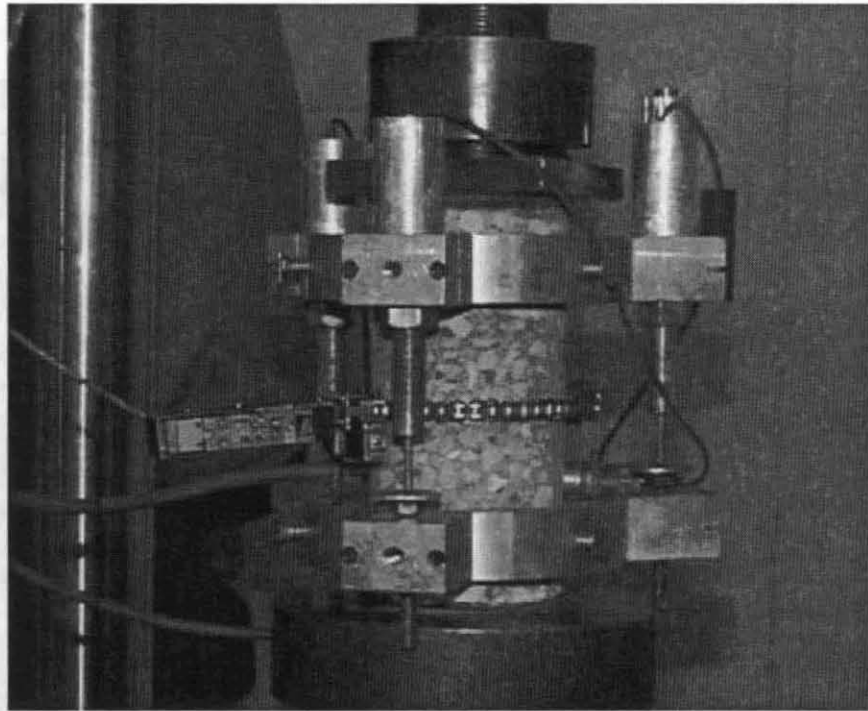


**Figure 2.28** Compression test on 3" diameter cored cylinders conducted using circumferential strain control

## 2.2.3 Creep Tests

### 2.2.3.1 Creep Load Frames

The creep load frames were fabricated at the University of Missouri – Columbia. The frames consist of three 1" diameter steel rods that connect four 1" thick triangular steel plates. Creep frames used are shown in Figure 2.29.

The load was held by three sets of railroad car springs. They had a full load capacity of 12,000 lbs and a spring constant of 3800 lb/in. Each set of springs consisted of three concentric springs. The capacity and spring constant reported are for all three concentric springs acting together. The springs were tested in a 110 kip capacity MTS machine using a 20 kip capacity load cell. The spring constants were experimentally determined and the three spring sets for each frame were chosen so that their stiffnesses matched closely. The springs were then sand blasted and painted.

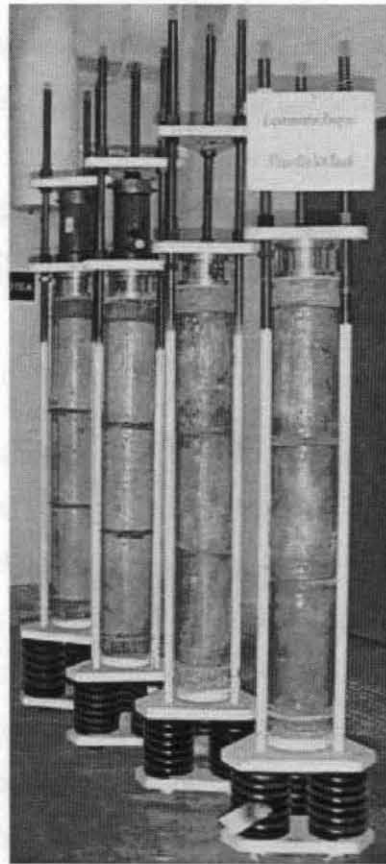


**Figure 2.29** Custom fabricated creep test frames

The frame is loaded using a 30-ton capacity hydraulic jack. The jack is positioned between the top two plates. Nuts hold the top plate while the jack is used to compress the rest of the setup including the springs. Once the desired load is obtained, nuts are tightened down on the plate under the hydraulic jack. The load is held between the second plate and the bottom plate by the springs. The hydraulic jack is then unloaded and can be removed.

The plate just above the springs contains a circular seat in which a  $\frac{3}{4}$  diameter ball bearing rests. A circular 6" diameter, 1" thick steel plate rests on the ball bearing, is free to pivot, and therefore minimizes potential bending effects. Two-inch long dummy cylinders are used above and below the three test cylinders to eliminate triaxial effects at the specimen ends (due to the differential Poisson's effect between the steel platen and the concrete). Two six inch square Teflon sheets were placed between the steel and the concrete dummy cylinders to further reduce friction.

Load cells specifically made for the creep test frames were designed and built at the University of Missouri – Columbia. A 2" tall aluminum ring is the main component of the load cell. The outer diameter of the ring is 5.25" and the inner diameter is 4.25". Two  $\frac{5}{8}$ " thick 6" diameter circular end plates were attached to the ring on either end. The inside of the aluminum ring was instrumented with a double full bridge of strain gages. Four axial strain gages and four Poisson's strain gages attached in one wheatstone bridge gives the load cell enough resolution to precisely measure the loads used in the creep frames. A 9 pin Bendix connector was attached to the outside of the ring to allow for a convenient interface.

#### **2.2.3.2 Creep Specimens**

The cylinders were initially cured along with the girders under the insulated tarp. The concrete specimens were kept in their plastic molds with plastic lids until 14 days after casting. The specimens were then removed from the molds, capped on both ends and sealed using paraffin wax. The goal of the sealing process was to eliminate the drying shrinkage component of the time dependant specimen deformation. Similar cylinders some of which were sealed and some left unsealed were monitored under an unloaded condition as comparison specimens to the creep test. The unloaded specimens are described in the section on shrinkage.

After sealing, brass studs were attached to the outside of the specimen with a rapid setting epoxy. The studs were attached in three sets at 120° spacing around the specimen.

Two types of concrete were tested for creep response, the HPC mix cast during the fabrication of the girders, and a normal strength concrete used for comparison. A total of four creep frames were used to test each combination of two concrete mixes and two load levels. The mix proportioning of both types of concrete is given in Chapter 3.

#### **2.2.3.3 Measurement**

A 10" gage length Whitemore gage was used to measure deformation of the specimens. The Whitemore gage measures the distance between the two brass studs and is capable of measuring displacements with a resolution of 0.0001". An initial reading was taken before the specimens were loaded. After loading, deformation and load measurements were recorded at varying intervals. Initially the intervals were small (one hour close to the start of the test) and later the intervals were larger (one month or more towards the end).

#### **2.2.3.4 Load Levels**

The two load levels used were determined by finding the expected average stress in the mid-span cross-section at two different times in the life of a Span 2-3 interior girder. The first load level was chosen to represent noncomposite, simple span stresses due only to prestress force and dead load. The average stress for the first load case was found to be approximately 1300 psi of compression. This stress level corresponds to a load of 36,755 lbs for a 6" diameter cylinder. The second load level was chosen to represent composite stresses due to prestress force, and dead load of girder and slab. The average stress in the mid-span cross-section of a Span 2-3 girder under these conditions was found to be approximately 900 psi of compression. This stress level corresponds to a load of 25,446 lbs for a 6" diameter cylinder.

These load levels were not meant to provide a parametric study of the creep response of HPC by any means. The goal of the creep tests was to obtain an understanding of the unrestrained creep characteristics of HPC as they pertain to this experimental program and provide some basis to interpret these results with the time-dependant deflections and strains measured on Bridge A5529.

#### **2.2.4 Shrinkage Tests**

A total of 8 types of specimens were tested for shrinkage. The parameters of the shrinkage specimens are: concrete strength (normal vs. HPC), specimen geometry (cylinders and beams), and sealing (waxed vs. unwaxed). The combinations of these three parameters make up

the 8 specimen groups. Three specimens of each group were monitored, to make a total of 24 shrinkage specimens.

The shrinkage cylinders are standard 6" diameter, 12" long cylinders. The specimens were prepared in the same way and at the same time as the creep specimens. This included capping both ends of all of the shrinkage cylinder specimens. The only difference in cylinder preparation between creep and shrinkage was that half of the shrinkage specimens were not waxed. A measurement of the drying shrinkage could therefore be made. Figure 2.30 shows the cylinder shrinkage specimens and a measurement being made using the Whitmore gage.

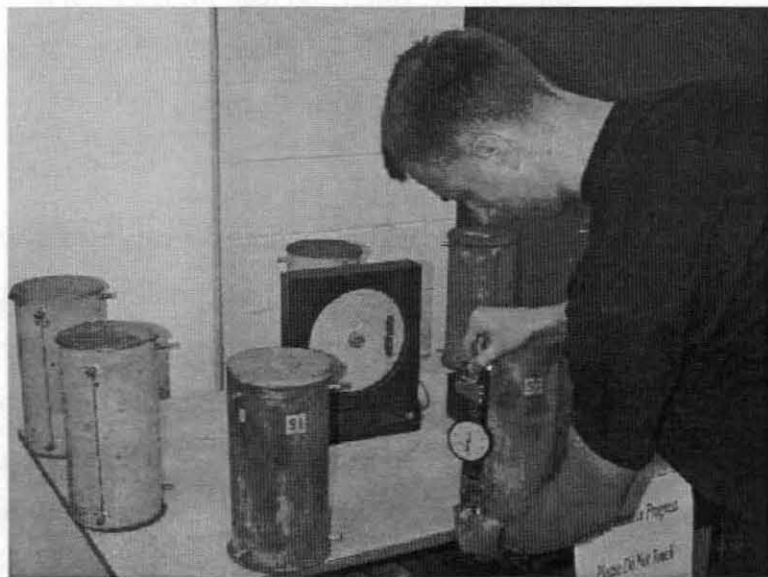


**Figure 2.30 Strain measurements on shrinkage cylinders**

The beam shrinkage specimens are  $3 \frac{1}{2} \times 4 \frac{1}{2} \times 16$ " prismatic specimens. The beams were demolded and half of them waxed at the same time as the other specimens. Preparation of the beam specimens was similar to the cylinders. The difference in preparation was that brass studs were attached to two sides ( $4 \frac{1}{2}$  dimension) of the beam. The beams were set on Teflon sheets to reduce the amount of friction between the concrete and the surface on which it rested. Measurement of beam specimen deformation was carried out using the Whitmore gage using a 10" gage length as described in the section on creep measurement. A beam shrinkage specimen is shown in Figure 2.31.

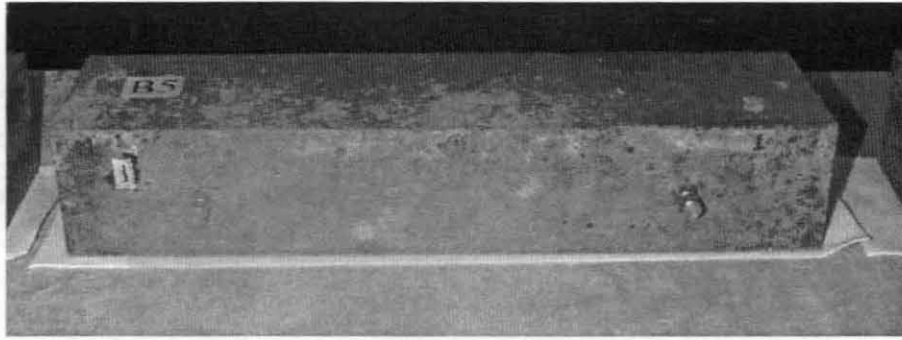


**Figure 2.31** Beam shrinkage specimens showing Demec points used for strain measurements

### 2.2.5 Fracture Tests

The fracture test specimens were sawed from the HPC slabs. The fracture tests were carried out approximately 56 days after casting. The notched beams used for the fracture test were 24" x 4" x 4" in size. The beams had a 2" deep notch in the center of the specimen, and were tested under three point bending. A clip gage was used to measure crack mouth opening displacement (CMOD). Mid-span deflection of the beam was measured using an LVDT attached to the box beam under the specimen. The test setup for the fracture tests is shown in Figure 2.32.

Fracture parameters that were found from the data include  $K_{IC}^S$ ,  $CTOD_C$ , and  $G_f$ . Recommendations in the RILEM draft standards were followed for the fracture test.

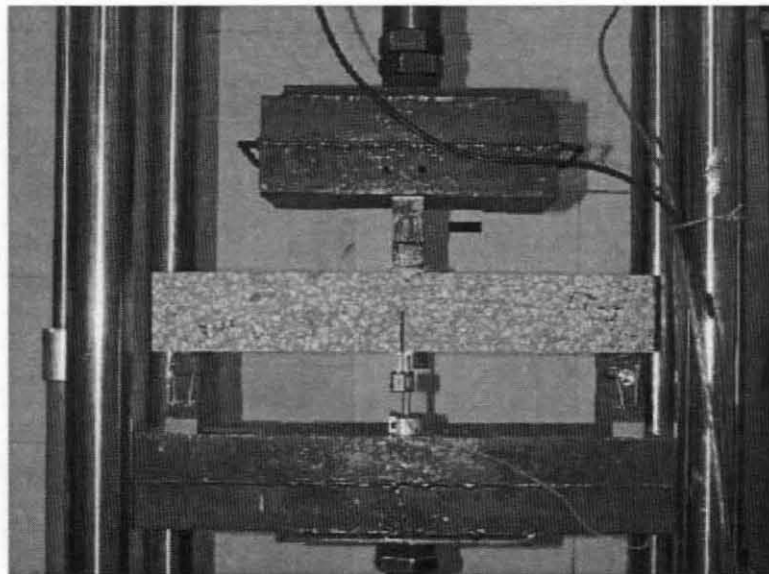


**Figure 2.32** Test set-up showing CMOD controlled notched beam

### **2.2.6 MoDOT Tests**

Several laboratory tests were also carried out at the MoDOT Materials Division. These tests included compressive strength tests at different ages of the concrete, modulus of elasticity measurements, freeze-thaw durability, and chloride penetration. The results of these tests are available in Chojnacki, 1999.

### **3. MATERIAL PROPERTIES**

#### **3.1 HPC Mix Design**

The provisions that MoDOT specified for the mix design were different than those usually used for a prestressed concrete girder bridge using NSC. Some of the special provisions are summarized in the following paragraphs:

A minimum cement content of 6.4 bags per cubic yard of concrete was specified. The water-cement ratio was not specified. The precaster was allowed to design mixes using water reducer (high or low range), other approved additives, fly ash, ground granulated blast furnace slag, or silica fume.

The precaster was required to submit specifications for the materials, mix design, designated slump, air content, water/cement ratio, mixing sequence and mixing times.

The minimum design air content was specified differently than normal high range water reducer mixes. The minimum design air content of the mortar portion could not be less than 8.0%. Based on the mortar content, the 8.0% figure was to be converted to a percentage total air content for the overall mixture.

The slump could not exceed eight inches, and had to be within two inches of the specified approved mix.

The water/cement ratio tolerance was  $\pm 0.020$  of that specified in the approved mix.

The mix was to provide 10,000-psi compressive strength at 56 days and 5,500 psi strength at the release of the prestress force.

The mix designed and used by Egyptian Concrete Co. used a water - cementitious material ratio of  $0.240 \pm 0.020$ . The materials included Type I cement from River cement plant in Selma, Mo., Class A Mississippi River Sand from Crystal City Sand Co. in Crystal City, Mo., Gradation "E" Plattin Limestone from Fred Weber Quarry in Festus, Mo., and city water. All admixtures used for the HPC mix were obtained from W.R. Grace. Admixtures used were Darvair 1400, an air-entraining agent, Daratard 17, a retardant, and Daracem 19, which is a high range water reducer. W.R. Grace Force 10,000 Silica Fume was added at the rate of 50 lbs per cubic yard. The mix proportions for the HPC are included in Table 3.1. The aggregate quantities reported are without moisture and the water content is the effective amount of water including the moisture from the aggregates.

**Table 3.1 – Typical proportioning for HPC and NSC mixes**

Constituent	HPC Mix	NSC Mix
Cement	902 lb/yd <sup>3</sup>	722 lb/yd <sup>3</sup>
Fine Aggregate	905 lb/yd <sup>3</sup>	1193 lb/yd <sup>3</sup>
Coarse Aggregate	1977 lb/yd <sup>3</sup>	1769 lb/yd <sup>3</sup>
Water	26.0 gal	27.3 gal
Water - Cement* Ratio	0.228	0.315
Air Entrainment Admixture	Daravair 1400 As Specified	Daravair 1400 As Specified
Retarder	Daratard 17 2.83 oz / 100 lb Cement	None
Silica Fume	W.R. Grace Force 10,000 50 lb/yd <sup>3</sup>	None
Admixture (HRWR / Other)	Daracem 19 23.57 oz / 100 lb Cement	ADVA Cast 8.47 oz / 100 lb Cement

\* Water – cement ratio includes silica fume as cementitious material

The mix proportions for the NSC mix used for the girders on the sister bridge A5530 are also included in Table 3.1 for comparison. The NSC cylinders and beams used in the creep and shrinkage tests for comparison to HPC were cast from this concrete. The only differences in materials used for the NSC mix were the use of Gradation “E” Derby Doe Run Dolomite from Lead Belt Materials in Park Hills, Mo. and the admixture ADVA Cast was used.

### 3.2 Compression Tests on HPC

To obtain reliable results, both ends of the cylinders were capped for all 6” cylinder compressive tests. Five cylinders were tested at an age of 59 days.

The results from the 3” cylinder compression tests are shown in Figure 3.1, and relevant properties are reported in Table 3.2. The results from the 6” cylinder compression tests are shown in Figure 3.2 and relevant properties are reported in Table 3.3.

The 3” cylinder compression tests exhibited an average compressive strength of 10,784 psi, average strain at ultimate of 0.002059 in/in, and an average modulus of elasticity of 5,870,000 psi. The 6” cylinder compression tests exhibited an average compressive strength of 11,953 psi, average strain at ultimate of 0.001882 in/in, and an average modulus of elasticity of

7,250,000 psi. The results from the compressive tests on standard 6” cylinders are used in further analysis and discussions of the girder behavior.

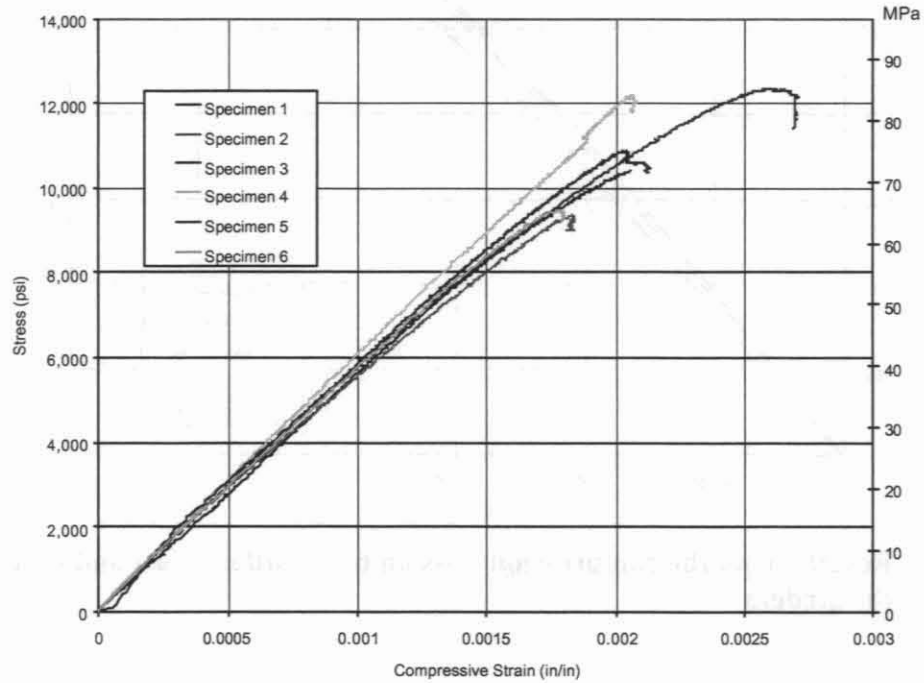


**Figure 3.1 Results from the compression tests on 3” cored cylinders**

**Table 3.2 – Results from the compression tests on 3” cored cylinders**

Specimen Number	Ultimate Strength psi (MPa)	Strain at Ultimate In/in	Modulus of Elasticity psi (GPa)
1	10,410 (71.78)	0.002057	5,594,000 (38.57)
2	9,374 (64.63)	0.001833	5,820,000 (40.13)
3	10,873 (74.97)	0.002024	5,887,000 (40.59)
4	12,199 (84.11)	0.002059	6,124,000 (42.22)
5	12,365 (85.26)	0.002600	5,412,000 (37.32)
6	9,484 (65.39)	0.001779	5,844,000 (40.29)
Average	10,784 (74.36)	0.002059	5,780,167 (39.85)

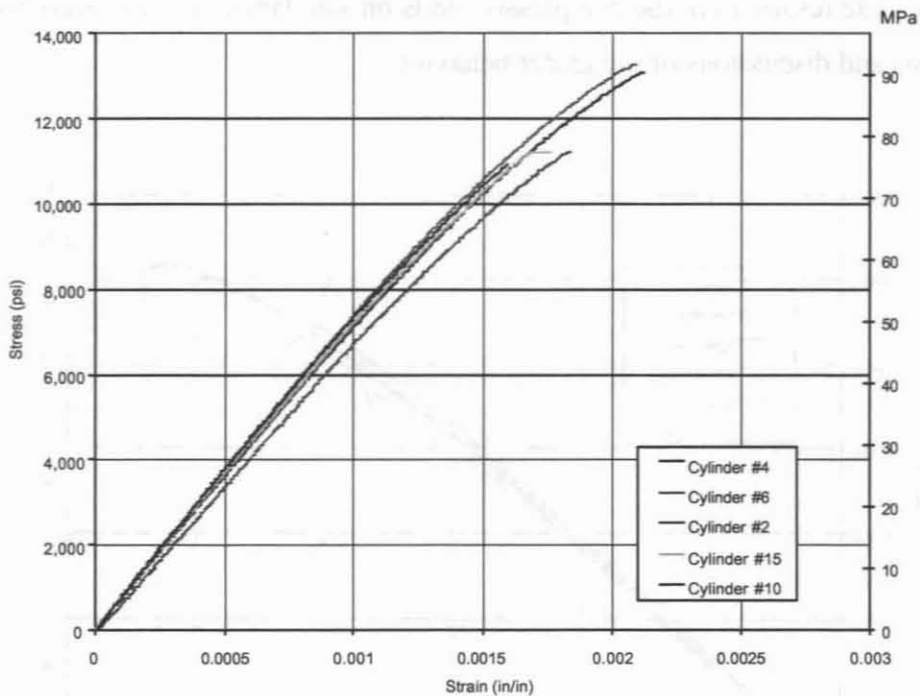


**Figure 3.2 Results from the compression tests on 6” cylinders (cast and cured along with the girders)**

**Table 3.3 - Summary of the results from the compression tests on 6” cylinders (cast and cured along with the girders)**

Specimen Number	Ultimate Strength psi (MPa)	Strain at Ultimate In/in	Modulus of Elasticity psi (GPa)
2	11,222 (73.15)	0.001839	6,720,000 (46.33)
4	13,096 (77.28)	0.002125	7,218,000 (49.77)
6	13,270 (75.57)	0.002091	7,419,000 (51.15)
10	10,954 (76.20)	0.001597	7,530,000 (51.92)
15	11,222 (75.74)	0.001758	7,362,000 (50.76)
Average	11,953 (74.36)	0.001882	7,249,800 (49.99)

### 3.3 Fracture Tests on HPC

Typical load-CMOD and load-deflection responses of the HPC beams in the fracture test are shown in Figure 3.3 and Figure 3.4. The average modulus of elasticity calculated from the elastic response of the specimens during the fracture tests was 5,447,000 psi (37,554 MPa). This modulus is considerably lower than 7,250,000 psi (49,987 MPa), the measured modulus of elasticity during the 6” diameter compression tests. The fracture parameters were calculated and

are tabulated in Table 3.4. There was a significant amount of variation in the measured  $CTOD_C$ . Less variation was noted in the  $K_{IC}^S$  values. The average measured values for  $G_F$ ,  $K_{IC}^S$ , and  $CTOD_C$  were  $0.619 \text{ lb-in/in}^2$  ( $108 \text{ N-m/m}^2$ ),  $1044 \text{ psi-in}^{1/2}$  ( $1147 \text{ kN-m}^{-3/2}$ ) and  $0.000413 \text{ in}$  ( $0.0105 \text{ mm}$ ) respectively.

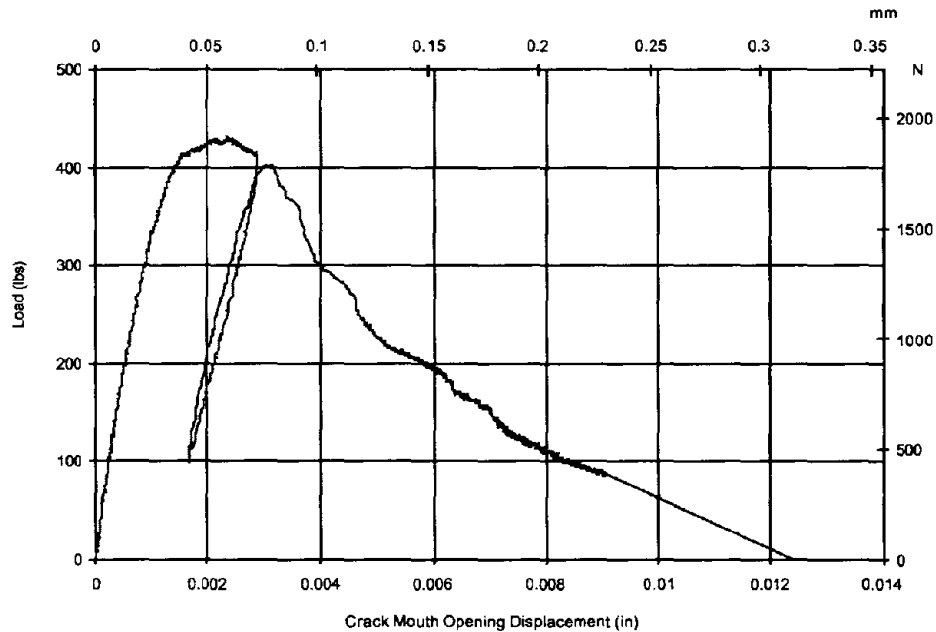


**Figure 3.3 Typical load – CMOD response of a notched HPC beam**

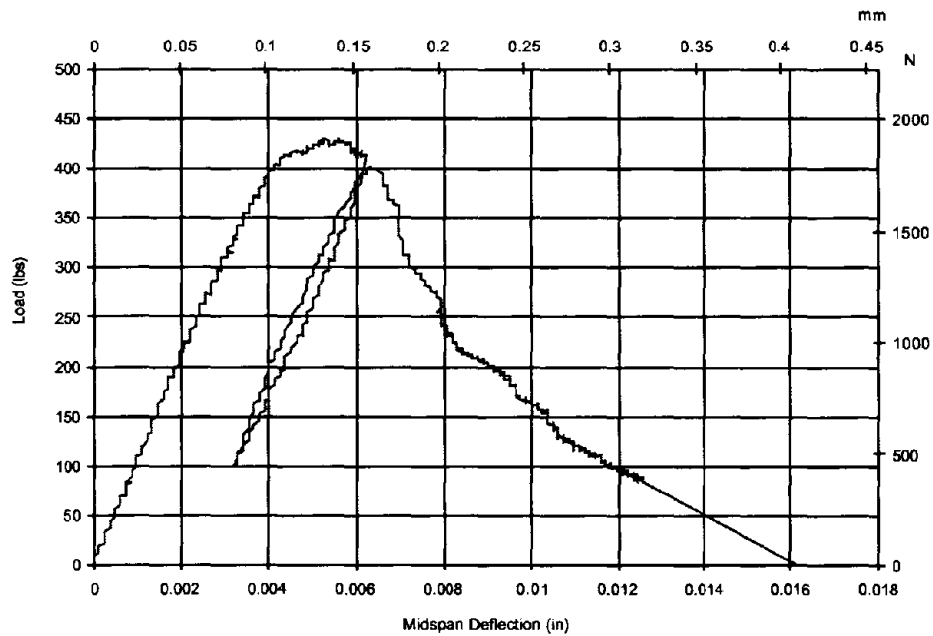


**Figure 3.4 Typical load – deflection response of a notched HPC beam**

**Table 3.4 - Summary of results from the fracture tests**

Specimen Number	Fracture Toughness, $G_f$ lb-in/in <sup>2</sup> (N-m/m <sup>2</sup> )	$K_{Ic}^S$ psi-in <sup>1/2</sup> (kN-m <sup>-3/2</sup> )	CTOD <sub>C</sub> in (mm)
1	0.474 (83.0)	872 (958)	0.000346 (0.00879)
2	0.558 (97)	978 (1075)	0.000456 (0.0116)
3	0.717 (125)	1002 (1101)	0.000341 (0.00866)
4	0.717 (125)	1302 (1431)	0.000553 (0.0141)
5	0.546 (95)	1094 (1202)	0.000540 (0.0137)
6	0.701 (122)	1016 (1116)	0.000241 (0.00612)
Average	0.619 (108)	1044 (1147)	0.000413 (0.0105)

### 3.4 Creep and Shrinkage of HPC

#### 3.4.1 Beam Shrinkage

A graph of the shrinkage strains in the beam specimens is shown in Figure 3.5. As expected, both sets of sealed beams showed less shrinkage than their unsealed counterparts. The HPC sealed beams exhibited 22% less shrinkage than the HPC unsealed beams after 140 days. The NSC sealed beams exhibited 41% less shrinkage than the NSC unsealed beams after 140 days. This implies that a smaller portion of the total shrinkage that HPC exhibits is due to drying shrinkage. HPC uses a much lower water-cement ratio and as a result there is less unused water. Therefore, it would be expected that HPC would exhibit less drying shrinkage, but more autogenous shrinkage.

For both sealed and unsealed beam specimens HPC exhibited less shrinkage at 140 days. The HPC sealed beam specimens exhibited 6% less shrinkage than sealed NSC beams at 140 days. The HPC unsealed beam specimens exhibited 28% less shrinkage than unsealed NSC beams at 140 days. As stated previously, it would be expected that sealed HPC specimens would exhibit more shrinkage than sealed NSC specimens. The effectiveness of sealing the specimens with wax alone was questioned during the course of these tests. It is possible that the sealed specimens do not represent a truly water-tight situation, and as a result may include some drying shrinkage.

The unsealed NSC beam shrinkage specimens reached 345  $\mu$ str after 140 days compared to 250  $\mu$ str of the unsealed HPC beam shrinkage specimens. The sealed NSC beam shrinkage specimens reached 197  $\mu$ str after 140 days compared to 115  $\mu$ str of the sealed HPC beam

shrinkage specimens. These trends are identical with only small increases in additional strains after one year of measurements.

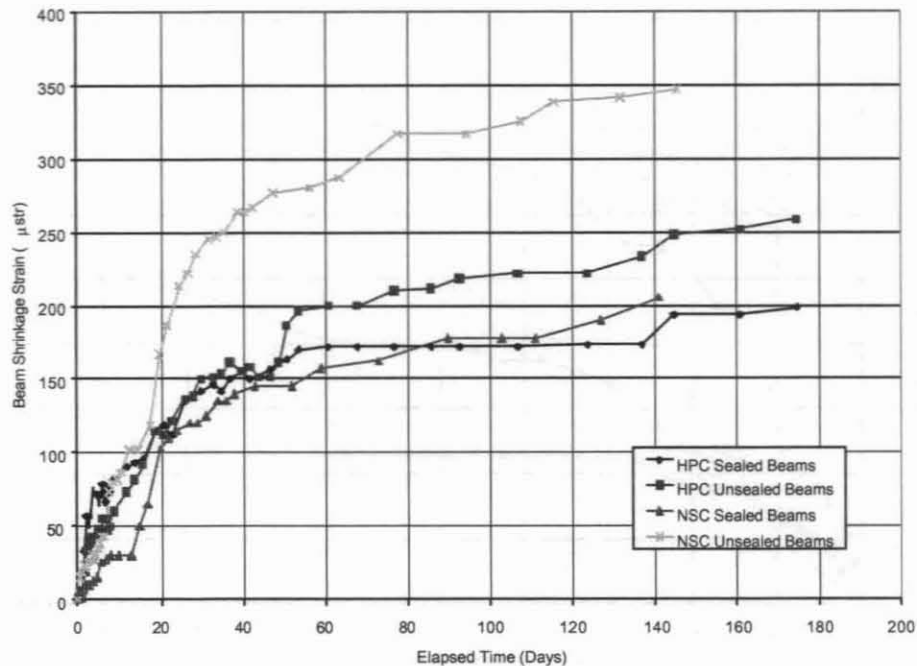


**Figure 3.5 Beam shrinkage as a function of time**

### 3.4.2 Cylinder Shrinkage

The results from the cylinder shrinkage specimens are shown in Figure 3.6. Like the beam specimens the HPC cylinder specimens exhibited less shrinkage in a sealed and unsealed state than the NSC cylinder specimens. The comparison of sealed to unsealed specimens is different however. Sealed HPC cylinders exhibited 49% less shrinkage than unsealed HPC cylinders after 140 days. Sealed NSC cylinders exhibited 50% less shrinkage than unsealed NSC cylinders after 140 days. The results from the cylinder shrinkage tests imply that drying shrinkage makes up the same portion of total shrinkage for HPC and NSC.

The unsealed HPC cylinders exhibited 42% less shrinkage than the unsealed NSC cylinders after 140 days. The sealed HPC cylinders exhibited 41% less shrinkage than the sealed NSC cylinders after 140 days. The unsealed HPC shrinkage cylinders reached 230 µstr after 140 days while the unsealed NSC shrinkage cylinders reached 393 µstr. The sealed HPC shrinkage

cylinders reached 115  $\mu\text{str}$  after 140 days while the sealed NSC cylinders reached 197  $\mu\text{str}$ . These trends are identical with only small increases in additional strains after one year of measurements.

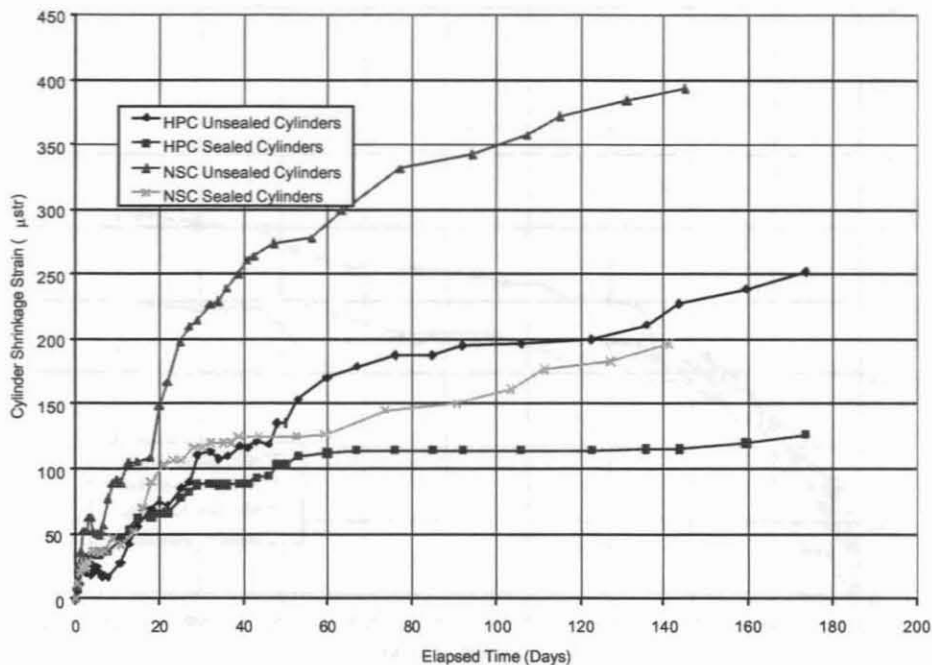


**Figure 3.6 Cylinder shrinkage as a function of time**

### 3.4.3 Total Creep

The initial elastic shortening was noted. HPC at 25 kips load exhibited a compressive strain of 135  $\mu\text{str}$  (implies a modulus of  $5.52 \times 10^6$  psi). HPC at 36 kips load level exhibited a compressive strain of 244  $\mu\text{str}$  (implies a modulus of  $3.70 \times 10^6$  psi). NSC at 25 kips load level exhibited a compressive strain of 123  $\mu\text{str}$  (implies a modulus of  $7.17 \times 10^6$  psi). NSC at 36 kips load level exhibited a compressive strain of 296  $\mu\text{str}$  (implies a modulus of  $4.31 \times 10^6$  psi). For both HPC and NSC the modulus of elasticity found from the load and strain in the creep frame loaded to 25 kip is much larger than the modulus of elasticity from the creep frame loaded to 36 kip. Since each value represents the average of three measurements on each of three specimens it is clear that some errors are involved in these small mechanical strain measurements. It should be noted that these mechanical strain measurements are not as accurate as electrical measurements reported earlier in Section 3.3.

The results of the creep tests are shown in Figure 3.7. As shown in the Figure 3.7, until approximately 90 days the HPC specimens were exhibiting more total creep than the NSC specimens for both load levels.

After 120 days the HPC specimens at 25 kips load level exhibited 4.5% less strain than the NSC specimens at the same load level. After 120 days the HPC specimens at 36 kips load level exhibited 13.5% less strain than the NSC specimens at the same load level. If the initial elastic shortening of the cylinders is removed, these differences become 21% and 24% respectively.

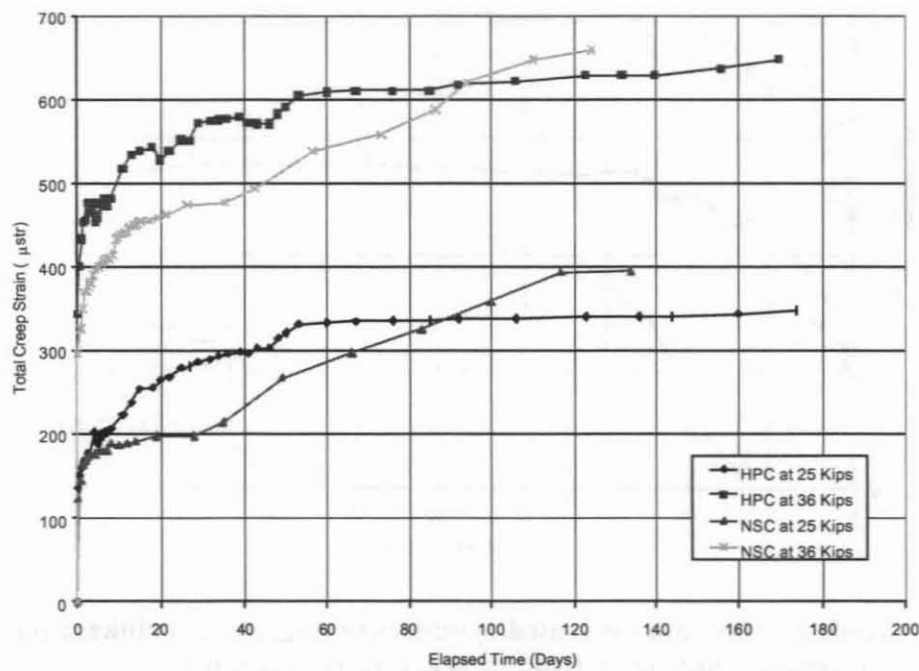


**Figure 3.7 Total creep strain for sealed cylinders (including elastic shortening and autogenous shrinkage) versus time**

### 3.4.4 Basic Creep

Basic creep is the strain caused solely by sustained loading, neglecting the effects of autogenous shrinkage and initial elastic shortening. The effects of drying shrinkage are assumed to be removed by the sealing of the creep cylinders. The strains measured on the sealed shrinkage cylinder specimens were subtracted from the total creep to obtain a measure of basic creep. The basic creep results are shown in Figure 3.8. The HPC cylinders exhibited a steady basic creep curve. The NSC cylinders at both load levels showed erratic results during the

interval between 10 and 60 days, the reasons for which are not clear. The HPC and NSC test frames were subjected to the same humidity / temperature environment in the laboratory. Also there was no change in the sustained load level during this period.

Regardless of erratic results, after 120 days of measurement the basic creep for the HPC and NSC cylinders are comparable at both levels of sustained loads.

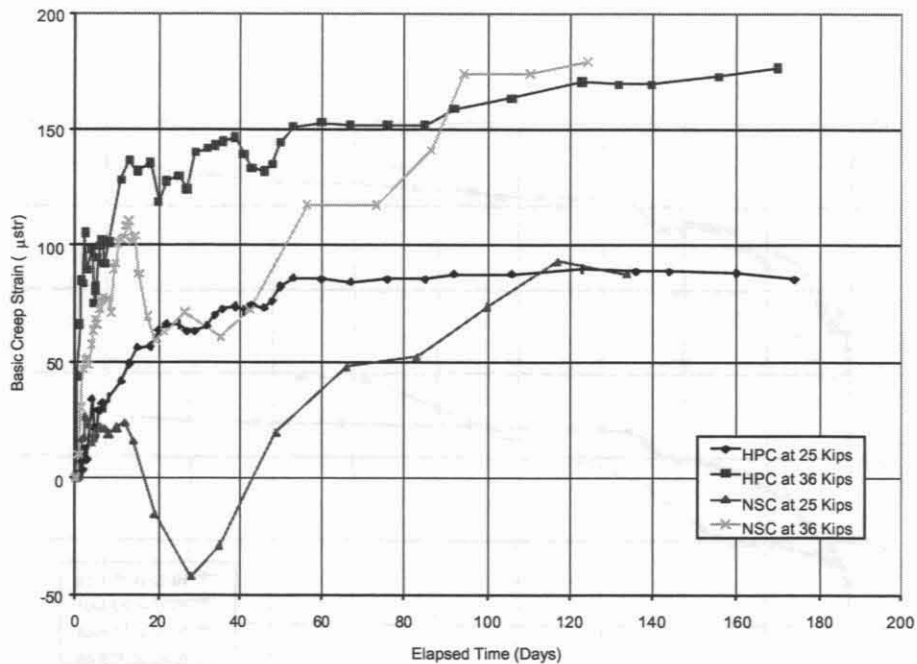


**Figure 3.8 Basic creep strain for sealed cylinders (autogenous shrinkage and elastic shortening subtracted from total creep) versus time**

### 3.5 Prestressing Strands

The prestressing strands are uncoated, seven-wire, low-relaxation, 1/4 inch diameter, Grade 270 strands conforming to AASHTO 203, manufactured by Sumiden W. P. Each reel that was used had a specified area and modulus of elasticity. For the long instrumented girders reels nos. 14246 and 13286 were used which had areas of 0.1527 in<sup>2</sup> and 0.1525 in<sup>2</sup> respectively and both have a modulus of 28.6 x 10<sup>6</sup> psi. Similar information was not available for the short girders, although it is speculated that comparable nominal areas and elastic modulus values are valid.

### 3.6 Reinforcing Bar

Tension tests were performed on the reinforcing steel that was used to fabricate the strain-gaged bars. The ½ diameter (#4) grade 60 reinforcing steel bars were supplied by Ahren's Steel of Columbia, Missouri.

A two-foot long specimen was tested in tension. The ends of the specimen were threaded with ½ -13 threads for approximately one inch. The center of the specimen was lathed down to a diameter of 0.372" for approximately two inches of the specimen. An extensometer with a 0.5" gage length was attached to this section of reduced area.

Tension loading was applied until failure. The extensometer was removed shortly after the specimen was loaded into the plastic region, so as to prevent damage to the extensometer. Figure 3.9 shows a graph of the results of the tension test. The yield strength determined was higher than expected for the Grade 60 rebar. The modulus of elasticity of the steel used for the strain-gaged bars was determined to be  $27.5 \times 10^6$  psi.

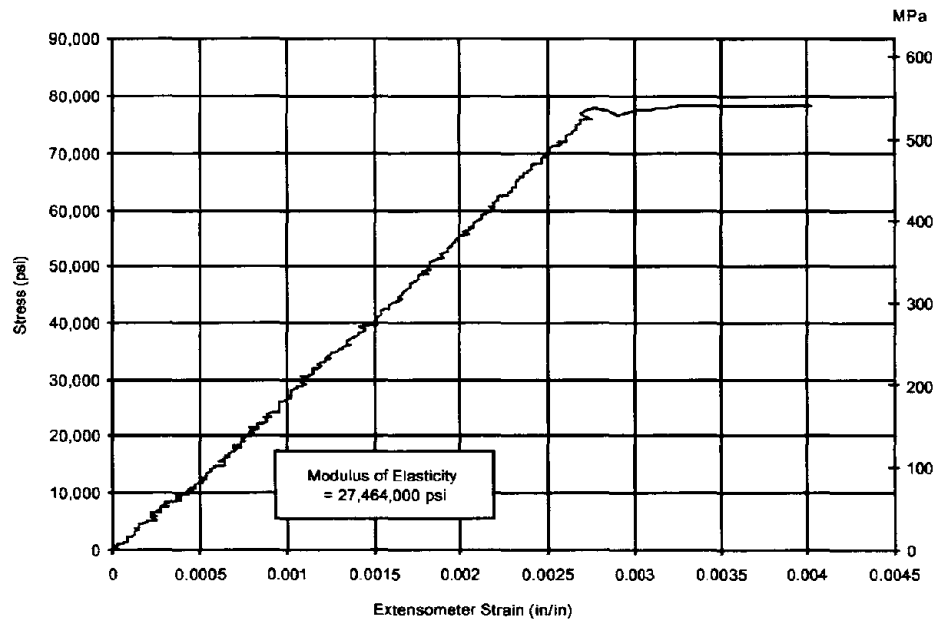


Figure 3.9 Stress-strain response of the reinforcing bar used for the strain-gaged bars

*This unnumbered page is intentionally left blank*

## **4. HYDRATION AND EARLY AGE RESPONSE**

### **4.1 Introduction**

The girders of Bridge A5529 were cast during June - July 1998 by Egyptian Concrete Co. in Bonne Terre, Missouri. The girders were cast in a large building approximately 300' x 100', which provided cover from direct sun and weather during initial curing. The steam used for curing the girders was generated at the north end of the building and piped under the girders going from the north to the south.

Tensioning of the prestressing strands for girders LX and LI occurred on July 23, 1998. Internal instrumentation in these girders was placed and secured after tensioning of the strands and in conjunction with the placement of the shear reinforcement. These two girders were the only girders cast on the 250' bed on that day. They were positioned near the north end of the building, which was near the steam generator, with girder LX sitting north of girder LI. The first batch of concrete was placed at 5:35 a.m. and girder LX was finished at 7:15 a.m.. Girder LI was begun shortly after, and was finished at 8:30 AM. The completion time for the second girder (LI) is referenced as "0" on the time axis of all plots related to hydration temperatures and strains of the long girders.

Girders SX and SI (G1-G2) were cast with three other girders (G3-G5) on the same bed. The instrumented girders, SX and SI were positioned one girder south of the north end of the bed, with girder SX sitting north of girder SI. The instrumentation was set on July 29, 1998 and casting occurred on July 30, 1998. Casting began at 7:40 a.m. Girder SX was finished at 8:45 a.m. and girder SI was cast between 8:45 a.m. and 9:20 a.m.. The completion time for the second girder (SI) is referenced as "0" in the time axis of all plots related to the hydration temperatures and strains of the short girders.

The concrete was mixed in a batch plant adjacent to the casting building. Concrete was loaded into a vehicle referred to as a sidewinder and brought into the main building. Figure 4.1 shows the sidewinder being loaded with concrete at the batch plant. Figure 4.2 shows a top view of the sidewinder and Figure 4.3 shows the concrete placement process. Concrete was placed in several layers and vibrated with hand held vibrators and a large vibrator that attached to the outside of the forms. This large vibrator was able to slide along the outside of the forms along the length of the bed. Both types of vibrators are shown in Figure 4.4. After placement, the top

of the girders were finished and covered with burlap, which was wetted. Girders were then covered with a heavy insulated white tarp, which extended to the ground on both sides. Steam was turned on approximately 12 hours after concrete placement. Steam was applied to the girders for a little more than two days.



**Figure 4.1** The sidewinder being loaded with concrete at the batch plant

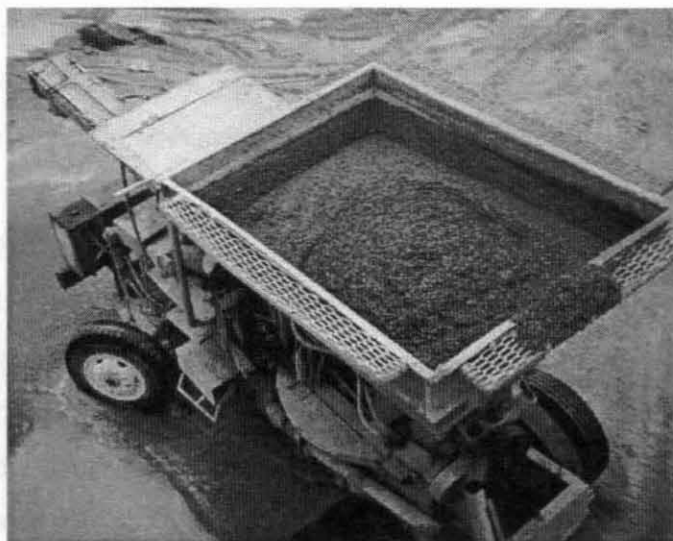


**Figure 4.2** Top view of the sidewinder

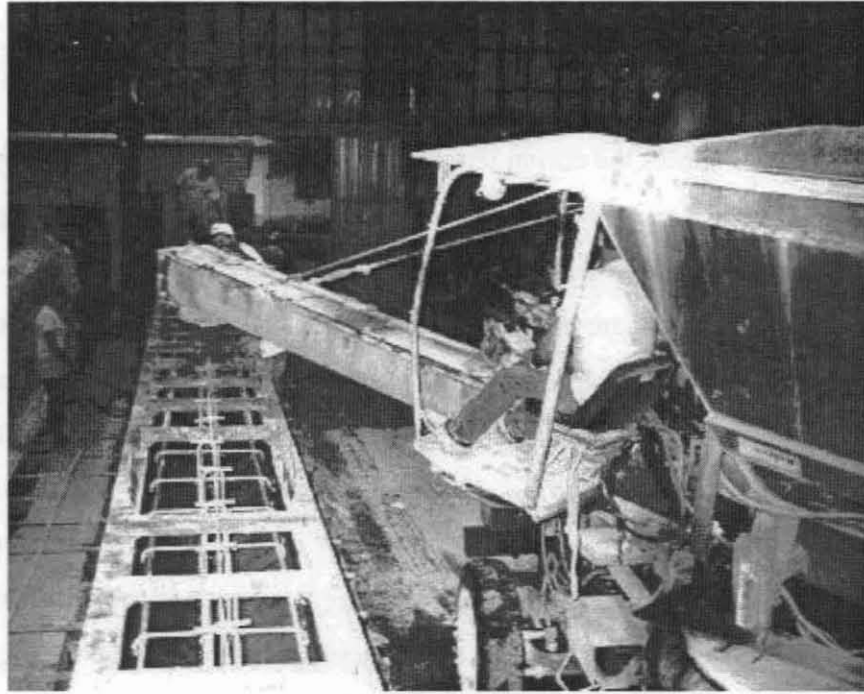
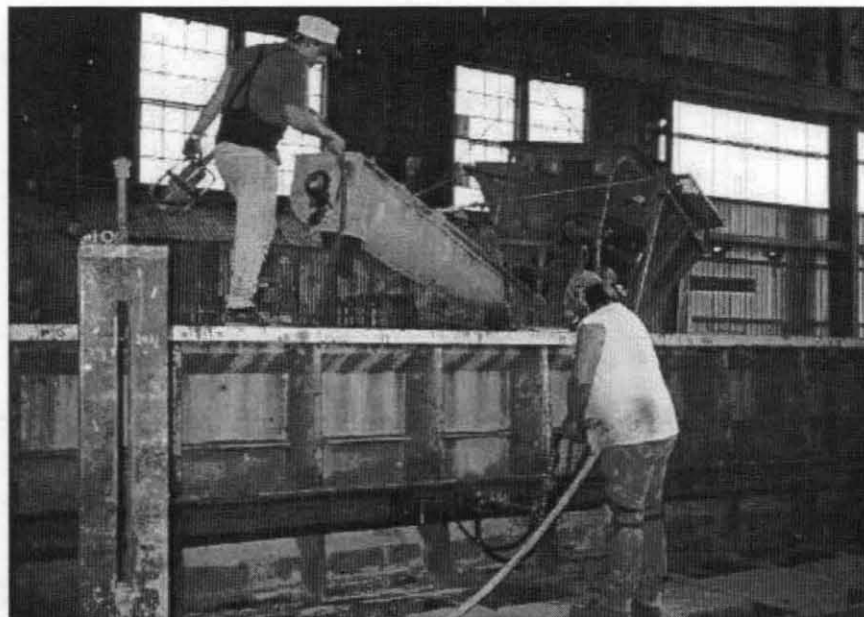


**Figure 4.3** Placement of the concrete in the forms



*(Note the vibrator attached to the side of the forms and the hand held vibrator operated from the top)*

**Figure 4.4** Vibrating the concrete during casting

## 4.2 Data From Instrumentation

### 4.2.1 Temperature

Figure 4.5 shows the curing temperatures as measured by the thermocouples in cross-section SIE. This figure shows the most extreme case of differential curing and temperature gradient of any of the cross-sections examined. It is very likely that this extreme case was caused by conditions that are not common practices that Egyptian Concrete usually follows. The thermographic survey was carried out on the short girders. To allow easy access to the girders a light tarp was used to cover one side of the girders from the midpoint of girder SI to the midpoint of girder SX. Usually Egyptian Concrete uses a heavy, insulated tarp to cover the girders during curing. The end cross-sections were both together in the middle of the section using the light tarp. These light tarps were also raised once every hour to undertake the infrared scans. Although cross-section SXE did not exhibit such drastic differential curing as SIE, it is very clear that the temperature history of cross-section SIE is not typical of the data obtained from the other cross-sections.

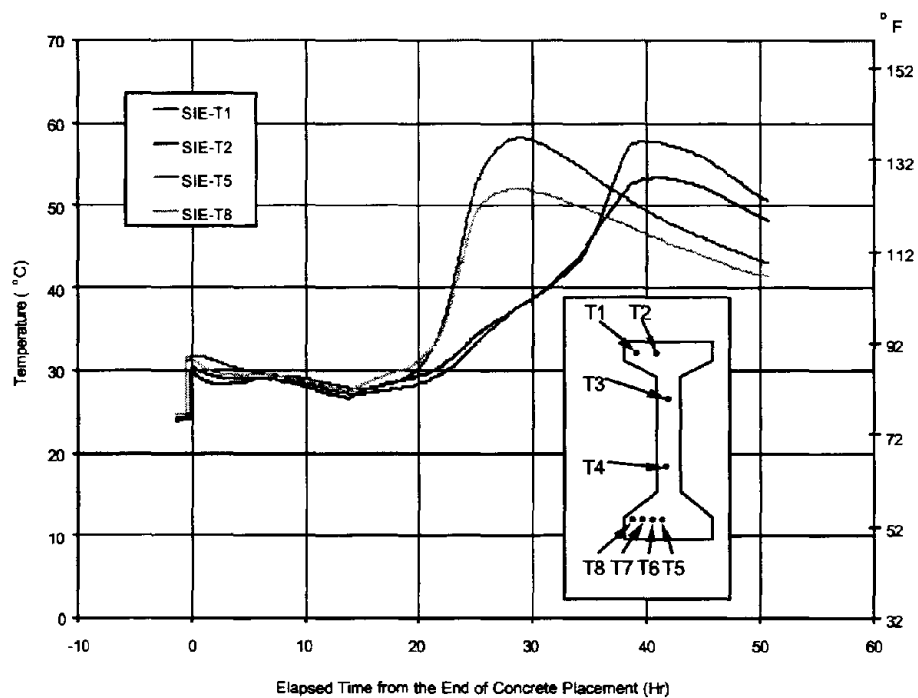


**Figure 4.5 Development of temperatures in cross-section SIE**

Hydration is an exothermic reaction. Although steam was applied externally to the girders the internal temperatures were largely due to the heat generated by hydration. Internal temperature development in the concrete can be correlated to the degree of hydration although this is beyond the scope of this investigation. Hardening and setting are also hydration dependent processes.

Gages SIE-T5, SIE-T6, SIE-T7 and SIE-T8 are in the bottom flange, SIE-T3 and SIE-T4 are in the web, and SIE-T1 and SIE T2 are in the top flange. The bottom flange reaches its maximum temperatures 29 hours after concrete placement. The top flange reaches its maximum temperature 40 hours after concrete placement.

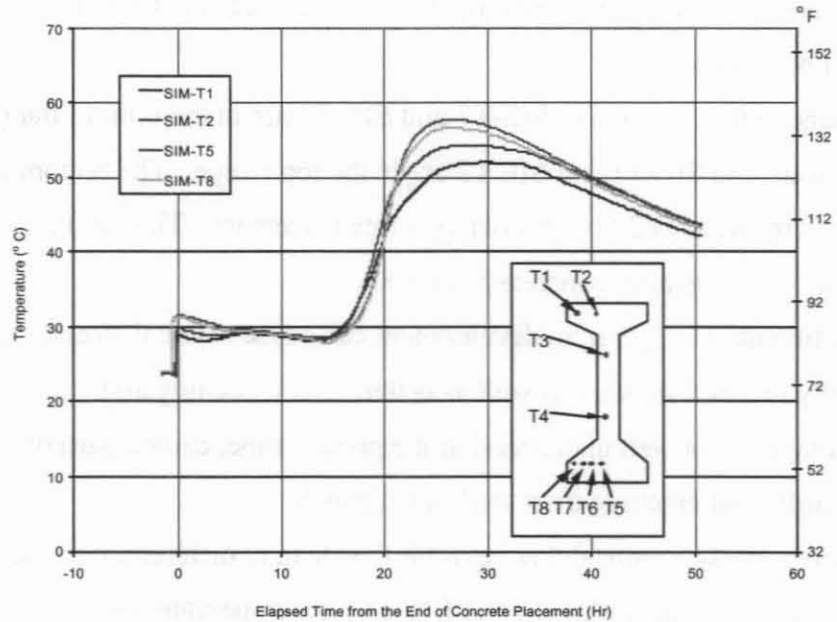
Differential temperature development can cause residual stresses in the girder, both due to thermally induced stresses, as well as differential hardening and volumetric changes. These aspects, although not well understood at the present time, can be partially responsible for the types of girder end cracking discussed in Chapter 5.

Some cross-sections did not exhibit this distinct differential temperature history. These cross-sections included SIM, LIE, and LXM. The temperatures in cross-section SIM during curing are shown in Figure 4.6. The top flange temperatures reach a maximum between 28 and 29 hours after concrete placement. The bottom flange temperatures reach a maximum between 26 and 27 hours after concrete placement. The maximum temperature difference measured in the cross-section was  $7.4^{\circ}\text{C}$  and occurred at 23.4 hours after concrete placement. This gradient was the smallest maximum gradient measured in any of the eight cross-sections.

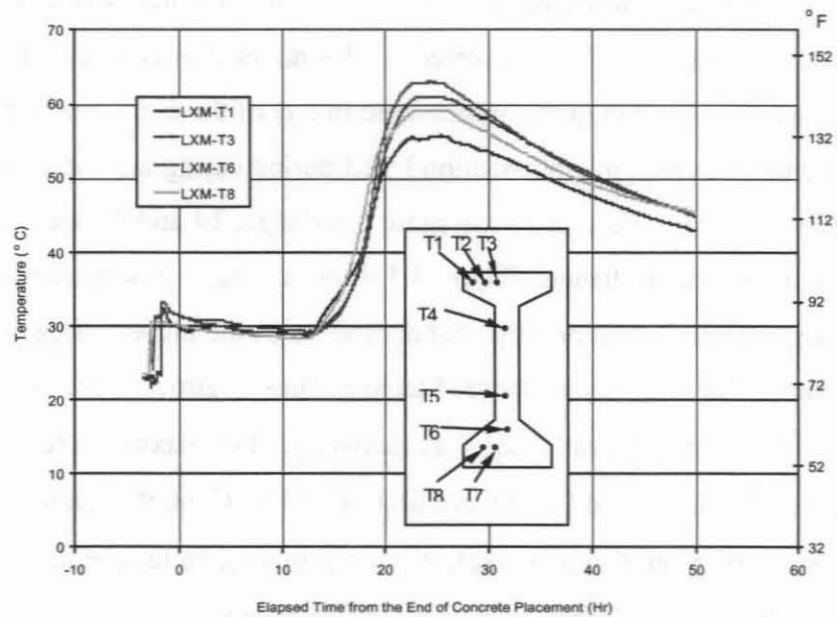
The temperatures in cross-section LXM during curing are shown in Figure 4.7. For the long girders, gages T1, T2, and T3 are in the top flange, T4 and T5 are in the web, and T6, T7 and T8 are in the bottom flange. Figure 4.7 shows the lack of noticeable differential heat development like cross-section SIM, but demonstrates the higher temperatures realized in the longer girders. The maximum-recorded temperatures in girders SIE, SIM, SXE, and SXM were  $62.7^{\circ}\text{C}$ ,  $57.8^{\circ}\text{C}$ ,  $58.9^{\circ}\text{C}$ , and  $58.6^{\circ}\text{C}$  respectively. The maximum recorded temperatures in girders LIE, LIM, LXE, and LXM were  $61.1^{\circ}\text{C}$ ,  $63.5^{\circ}\text{C}$ ,  $60.9^{\circ}\text{C}$ , and  $65.6^{\circ}\text{C}$  respectively. This shows a little more than  $3^{\circ}\text{C}$  higher average maximum temperature in the long girders.

The effect of the different covering methods must also be considered when comparing the maximum temperatures. Cross-sections SIE and SXE, which would be most affected by the different tarp used, exhibited higher peak temperatures than cross-sections SIM and SXM. In the

long girders the mid-span cross-sections exhibited higher temperatures, which would be expected because a larger mass of hydrating concrete surrounds the mid-span cross-sections.

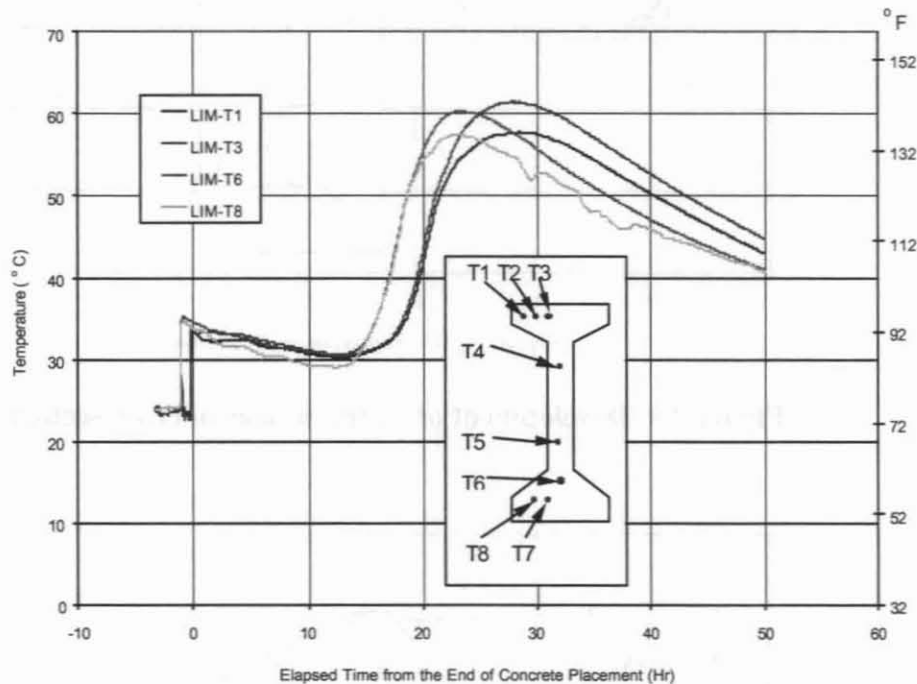


**Figure 4.6 Development of temperatures in cross-section SIM**



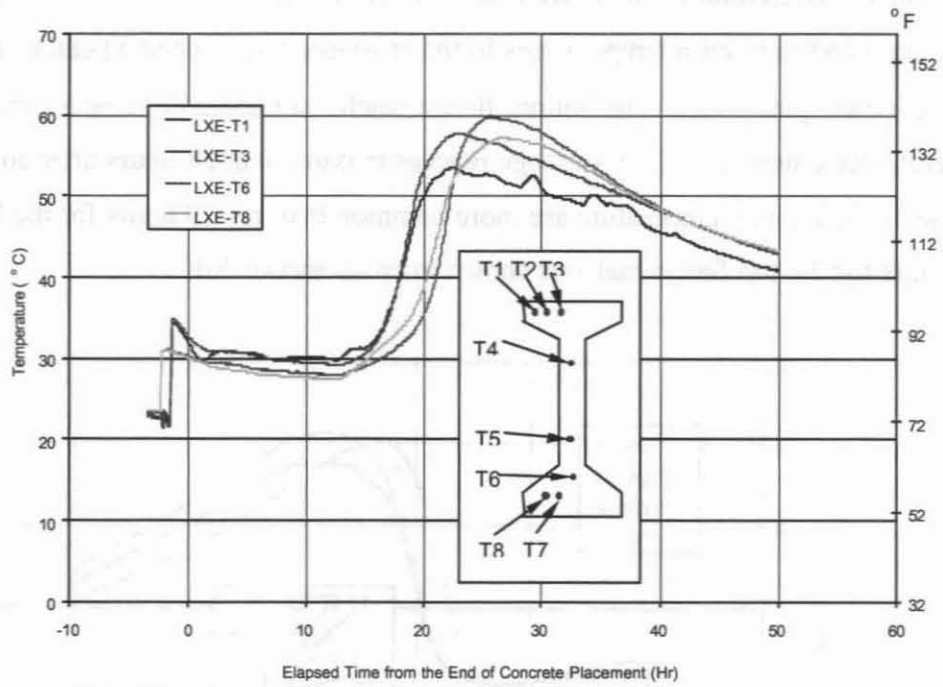
**Figure 4.7 Development of temperatures in cross-section LXM**

Figure 4.8, which shows temperature development in cross-section LIM, gives an example of differential curing more common than cross-section SIE. The difference between the maximum and minimum temperatures in the cross-section reached a peak of 17° C at 19 hours after concrete placement. The bottom flange reaches a maximum temperature at 23 hours after concrete placement, and the top flange reaches maximum at 28 hours after concrete placement. These times to peak temperature are more common than the 29 hours for the bottom flange and 40 hours for the top flange that was shown in cross-section SIE.



**Figure 4.8 Development of temperatures in cross-section LIM**

Figure 4.9 shows the only exception to what was typically observed (typically bottom flange temperatures peaking earlier than the top flange temperature). Cross-section LXE shows the top flange reaching maximum temperatures before the bottom flange. Temperature gradients of almost 19° C were recorded at 20 hours after concrete placement. Figure 4.10 shows the curing temperatures in cross-section LXE as measured by the thermistors, which closely matched those measured using thermocouples. Gage LXE-V1t is positioned in the middle of the top flange unlike LXE-T3 that is offset about 2 inches from the center. Gage LXE-V1t shows a higher temperature and reaches a maximum higher than any of the other gages in the cross-section.



**Figure 4.9 Development of temperatures in cross-section LXE**

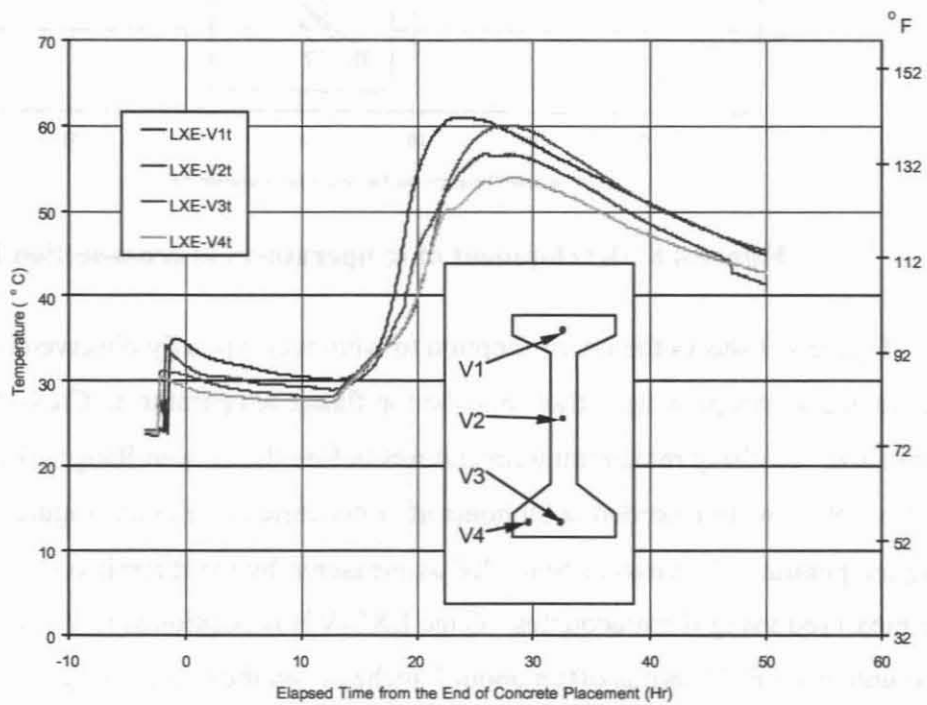


**Figure 4.10 Thermistor temperatures in cross-section LXE**

It is evident that positioning of the gages is critical. It should be stated therefore that even though the exact locations of all gages were recorded before casting, small movements could have occurred during concrete placement. It is also likely that, although 12 temperature measurements in a cross-section were made, the actual maximum temperatures during casting may have occurred at location(s) other than where the gages were placed.

Figure 4.11 and Figure 4.12 show the difference between the maximum and minimum recorded temperatures in the cross-section. This measure of the temperature gradient shows when the maximum gradients occurred. The cross-sections that did not exhibit noticeable differential curing also show the least amount of temperature gradient. This is because the maximum temperature gradients occur when the temperature in one flange is increasing rapidly while the other flange is not heating as quickly. The maximum gradient generally occurs between 19 and 22 hours after concrete placement.

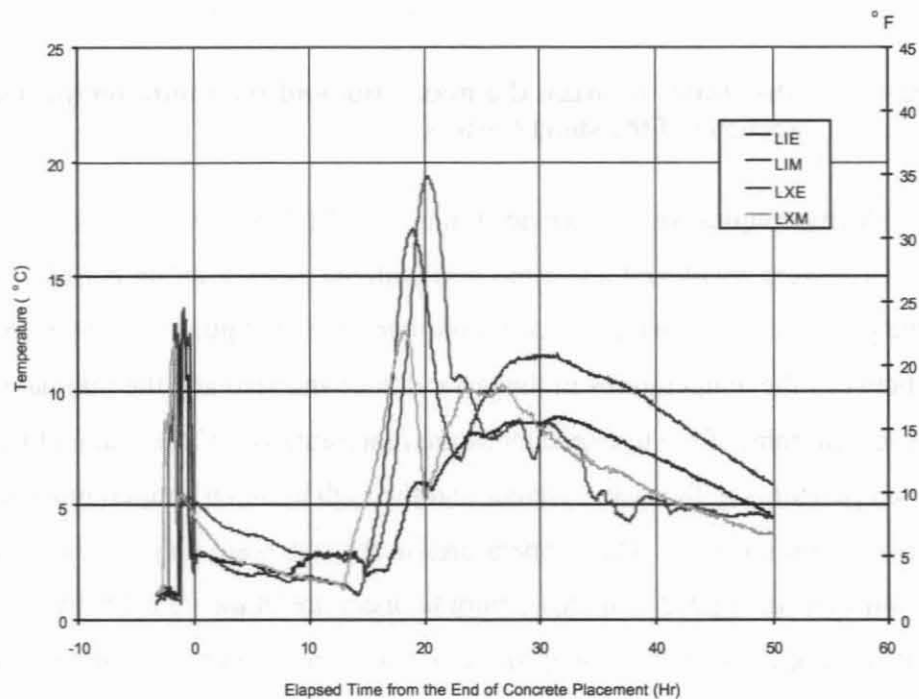


**Figure 4.11** Difference between the maximum and minimum temperatures in the cross-sections of the long girders

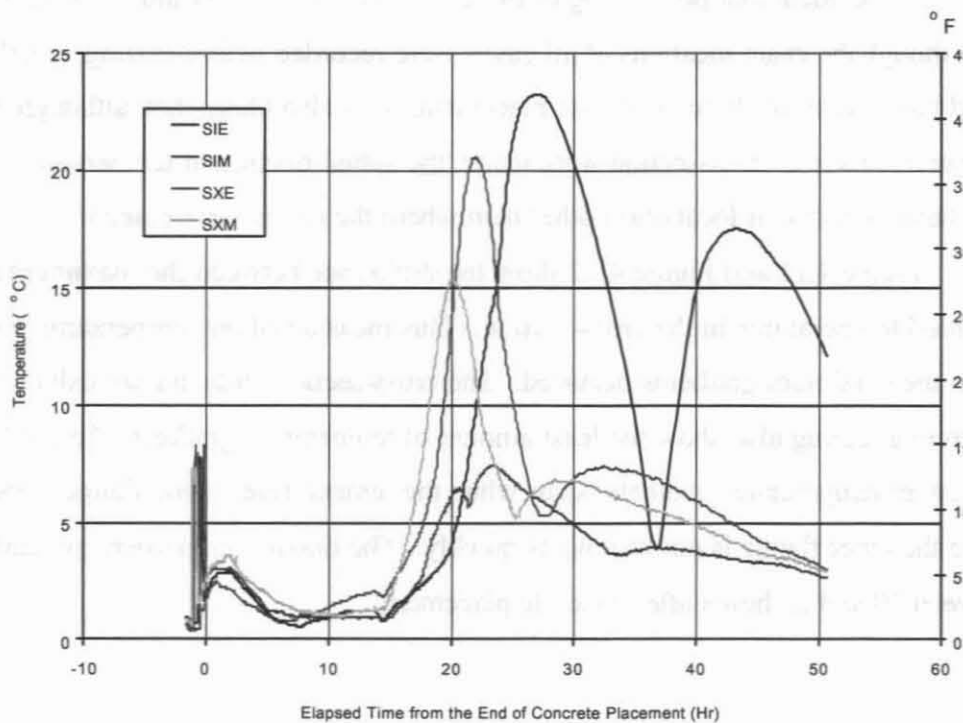


**Figure 4.12 Difference between the maximum and minimum temperatures in the cross-sections of the short girders**

Thermocouples were also placed in one of the 2' x 2' x 6" slabs and one standard 6" cylinder that were positioned under the tarp with the girders during curing. Storing test cylinders with the girders during curing is a common practice at Egyptian Concrete. A comparison was made between the temperatures in the test cylinder and slab and the internal temperatures of the girders to determine if the test specimens are representative of the material in the girder. A graph of the temperatures in the slab, cylinder and the high and low temperatures in cross-section LXM are shown in Figure 4.13. The temperatures in the slab were very representative of the temperatures in the girder. The maximum temperature in the cylinder was comparable to the lower peak temperatures in some girder cross-sections. Figure 4.13 shows that it may not be necessary to specially match cure cylinders to reproduce heat development history in the girders. It is possible to achieve comparable temperature histories simply by curing the cylinders in the same environment as the girders.

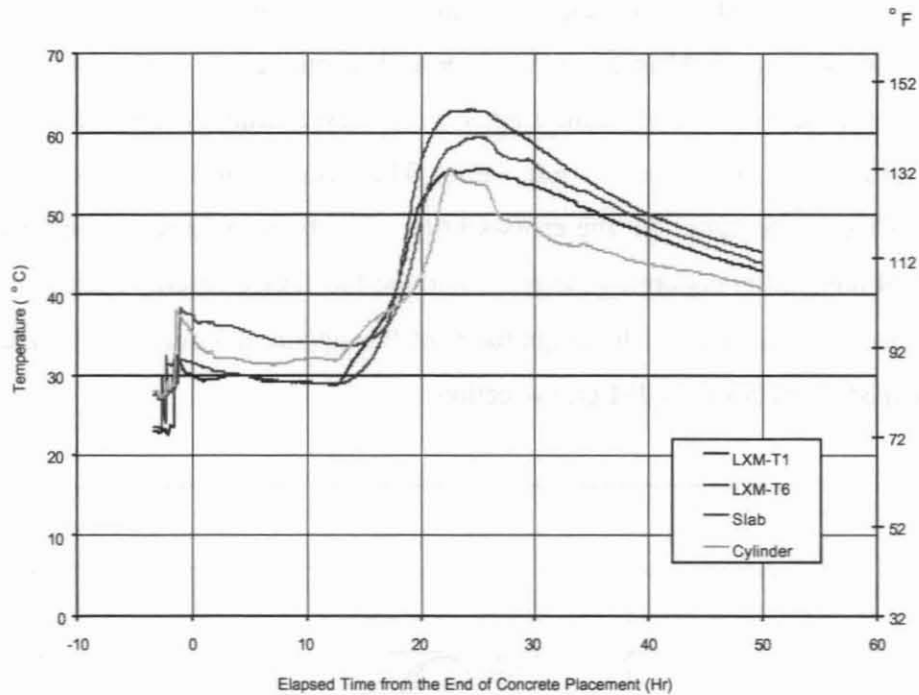


**Figure 4.13 Test slab and cylinder temperatures compared to girder temperatures**

#### 4.2.2 Strains

Readings from the strain-gaged bar, vibrating wire strain gage, and instrumented stirrups were recorded during curing. The apparent strain during curing cannot be considered an accurate representation of the strain in the concrete. Before hardening the concrete is plastic, and is able to flow like a liquid. After hardening the concrete is solid with time-dependent strength and stiffness development. Strain takes on a very nebulous meaning when concrete is in this early age transition. Strains recorded during these early ages are hence termed “apparent strains” to highlight this fact. However, it is interesting to study how strain develops at these early ages when heat development and liquid to solid transition takes place. Even if strain magnitudes during these early ages are not relevant, relative magnitudes and signs offer valuable clues to potential distributions of residual stresses built-up in the girders.

The apparent strain in the strain-gaged bar, vibrating wire strain gage, and instrumented stirrup show what types of strains are induced in these gages by movement in the concrete, and therefore relative magnitudes and peak times are meaningful.

Figure 4.14 shows the apparent strain observed by the strain-gaged bars in cross-section LIM. Cross-section LIM is the example described previously as representing what happens in a typical cross-section. In all strain graphs compressive strain is represented as a negative strain value and tension as a positive strain value. The trend in the apparent strains is similar to the trend in the temperatures for the cross-section. The bottom flange reaches maximum first at about 24 hours after concrete placement and the top flange reaches maximum around 30 hours after concrete placement. The magnitudes of this apparent strain reach a maximum compressive strain of  $360 \mu\text{str}$  for the LIM cross-section.

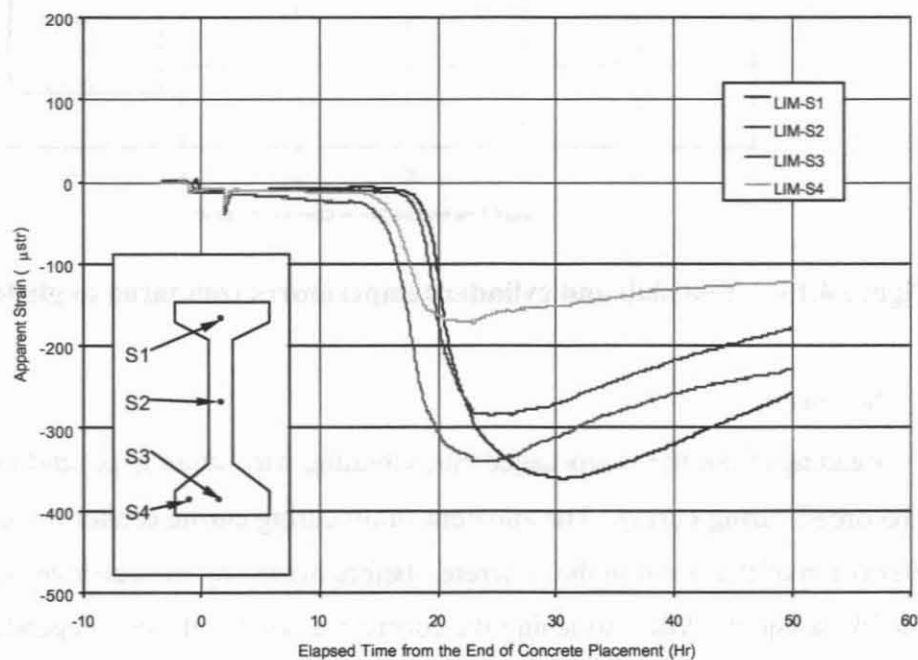
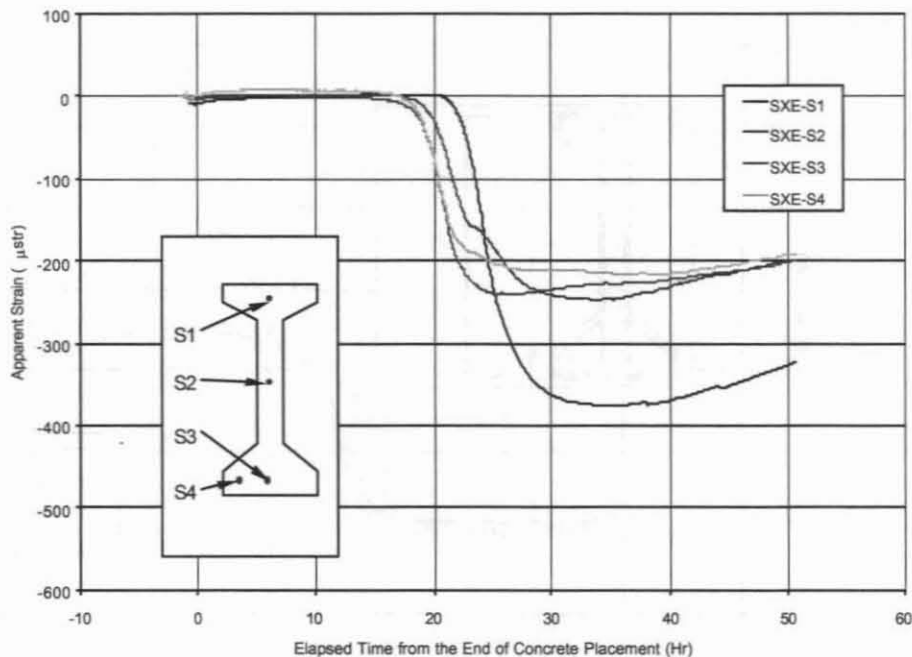


**Figure 4.14 Apparent strain from strain-gaged bars in cross-section LIM**

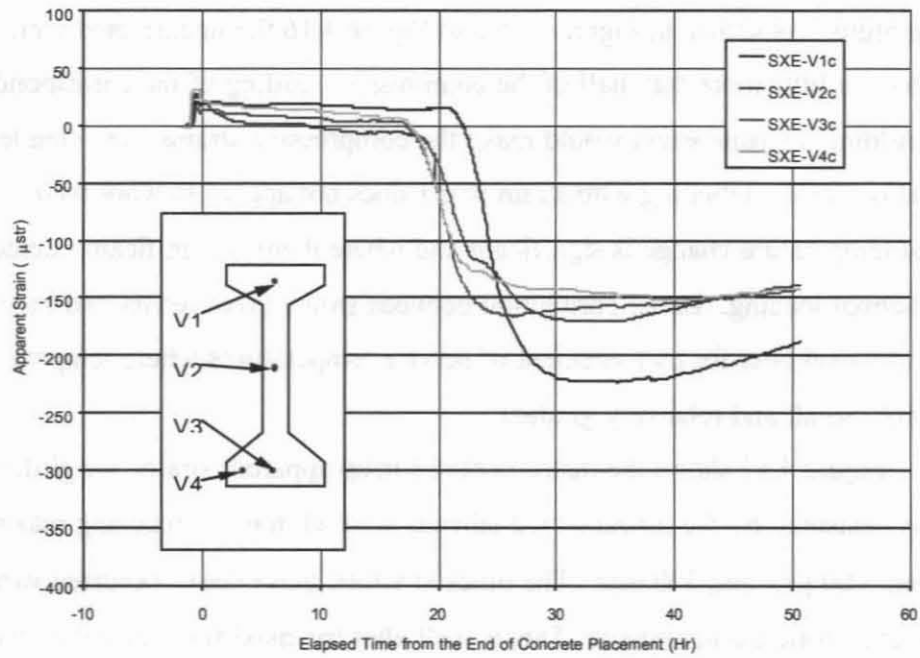
The vibrating wire strain gage operates on the principle that the natural frequency of a wire is dependent on its length (strain). But, since the length of that wire changes with temperature, the vibrating wire strain gage output is temperature dependent. The manufacturer gives a correction for this effect. The correction is based on the fact that the wire is made of steel and the coefficient of linear thermal expansion of steel is  $12.2 \mu\text{str}/^{\circ}\text{C}$ . Therefore the correction provided by the manufacturer is to add a tensile strain of  $12.2 \mu\text{str}/^{\circ}\text{C}$  to the uncorrected reading.

Figure 4.15 and Figure 4.16 show vibrating wire strain readings uncorrected for temperature. As shown in Figure 4.15 and Figure 4.16 the uncorrected vibrating wire strain gage reading is a little more than half of the compressive reading of the corresponding strain-gaged bar. Adding a tensile strain would make the compressive strains even smaller. The temperature correction for the vibrating wire strain gages does not appear to work well in situations where rate of temperature change is significant and where there is significant interaction of mechanical and thermal loading. Better correlation between strain gages rebars and the vibrating wire gages were obtained later for measurement of service temperatures where temperature changes are relatively small and relatively gradual.

Figure 4.17 shows the instrumented stirrup apparent strains for girder SX. The apparent strains measured by the instrumented stirrups were all tensile, reaching maximum values between 100  $\mu$ str and 300  $\mu$ str. The times at which these peaks occurred varied from 30 to 45 hours after concrete placement. This is well after the maximum measured temperatures occur in most cases.



**Figure 4.15** Apparent strain from strain-gaged bars in cross-section SXE



**Figure 4.16** Apparent strain from vibrating wire strain gages in cross-section SXE

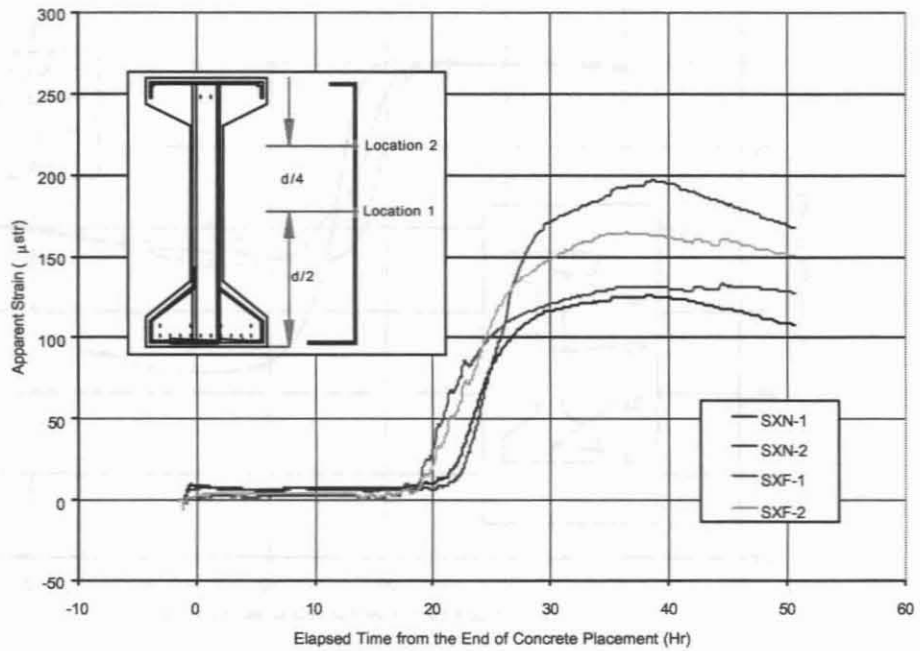


**Figure 4.17** Apparent strains in stirrups used in girder SX

## **4.3 Thermographic Survey**

### **4.3.1 General Information**

A thermographic survey of the two short span girders was carried out during the curing process. Electro-Test Inc did the work. An Amber Raytheon infrared camera was used to obtain external temperatures along half of each of the two short instrumented girders. Data was to be taken at one-hour intervals for twenty-four hours after casting. This time period extended from the morning of July 30, 1998 to the morning of July 31, 1998. The objective of the survey was to define temperature gradients and hot spots along the exterior of the girders during curing.

Data submitted by Electro-Test Inc. included bitmaps of infrared images, Amber Therm data files from the infrared camera, a videotape of the collection process, and spreadsheets indicating maximum and minimum temperatures for each section surveyed during the time period.

### **4.3.2 Limitations of the Thermographic Survey**

Unfortunately, there were several limitations (Eatherton, 1999, White, 1999) to the analysis that could be done with the information provided by Electro-Test Inc. The software needed to access the Amber Therm data files was unavailable. Visual data, from bitmap files or the video, could not easily be compiled into a composite infrared picture of the whole girder because the color scale used to define temperature changed. The set of bitmap files provided by Electro-Test Inc. were not complete enough to allow a composite picture, regardless of the difficulty with color scale.

The spreadsheet data provided by Electro-Test Inc. on maximum and minimum temperatures was inadequately referenced to allow direct point-to-point correlation as originally planned. First, the position on the girder for the various readings was not well referenced. The temperatures were related to a section number, which refers to the spaces in between ribs on the girder forms. This made it difficult to relate the temperatures to exact locations without exact measurements of the rib spacing. Secondly, the method for which the maximum and minimum temperatures were found involved defining a line along the depth of the girder in each section. The exact location of this reference line in each section was not documented. Additionally, this reference line was not consistent through the course of the survey.

### 4.3.3 Results From the Thermographic Survey

Considering the limitations of the data provided, the conclusions that can be made from the thermographic survey are largely qualitative and general. Figure 4.18 shows the side of the girders. The space between two girders can be seen on the forms as a darker section at the location of the terminal boxes and wires seen in the background of the picture. The high temperatures marked by the light colors coming out from under the girders shows the effect of steam. The slightly darker vertical lines are the ribs in the forms and the dark horizontal line is a cross-brace on the ribs.

Figure 4.19 shows an infrared photograph of one of the sections of the girder after approximately 13.5 hours of curing. This photograph shows the relatively small temperature gradient in the section at this time. Also temperatures are quite low still, which is collaborated by the internal thermocouples. The gradient in the temperatures on the form is not well defined because the lower temperatures of the ribs and tarps above the girder widen the temperature scale.



Figure 4.18 Infrared photograph showing the side of girders SI and SX

Figure 4.20 shows an infrared photograph of one of the sections of the girder after approximately 19.5 hours of curing. The rise in temperature of the steel mold in contact with the

concrete and the ribs is noted. The slightly darker contour on the part of the form that touches the concrete is the isotherm temperature of 32.9° C (91.2° F). This shows that the bottom flange is warmer than the top flange. The region inside the isotherm contour is the hottest part of the form on this picture and occurs at the junction between the bottom flange and the web.

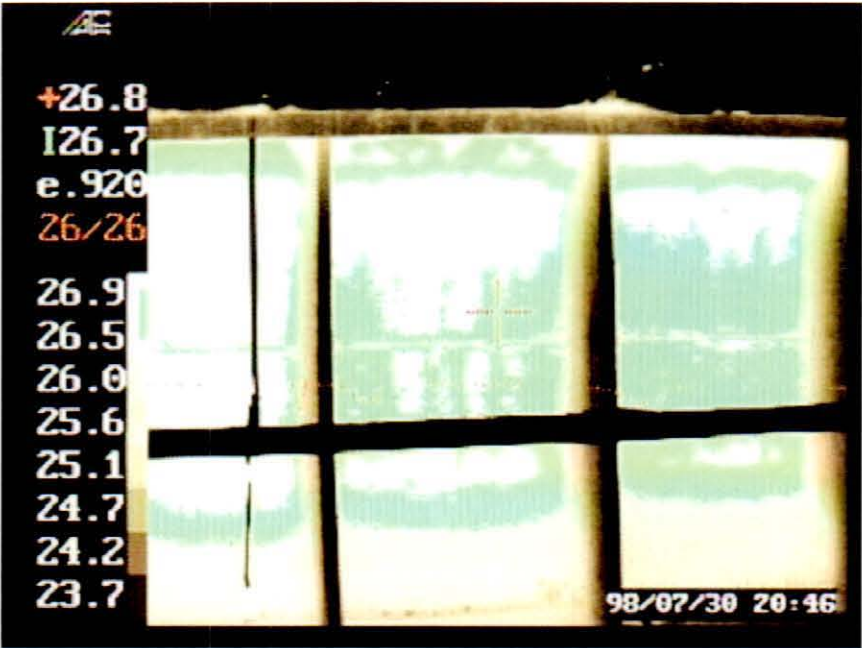
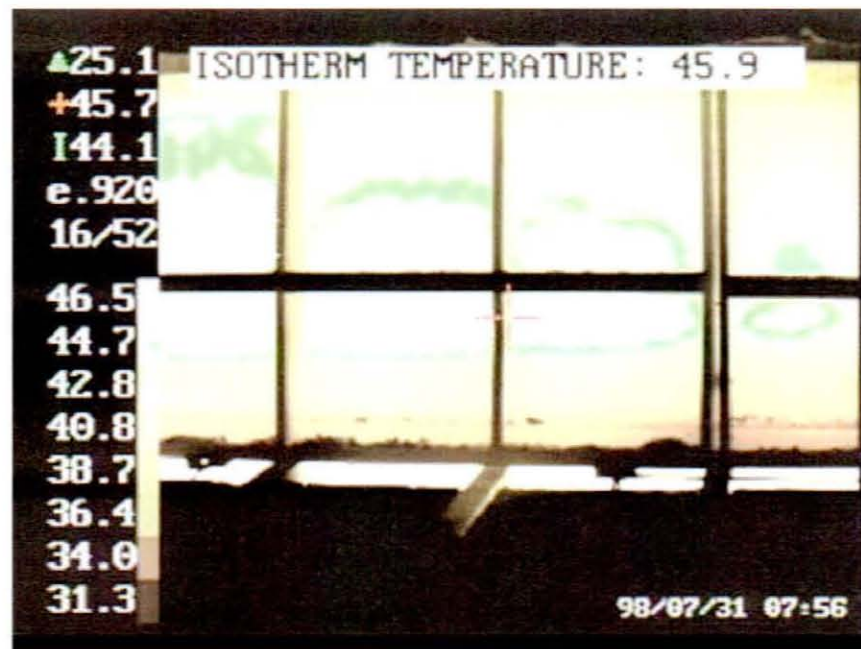


Figure 4.19 Infrared photograph of girder after approximately 13.5 hours of curing



Figure 4.20 Infrared photograph of girder after approximately 19.5 hours of curing

Figure 4.21 shows an infrared photograph of the girder at the end of the thermographic survey, 22.5 hours after casting. The temperatures were seen to rise until the end of the survey, so it is probable that these final readings do not represent the true peak in the cross-sectional temperatures. The darker contour in this figure is the isotherm temperature of 45.9° C. It is clear that the junction between the bottom flange and the web is still the hottest spot in the section.



**Figure 4.21 Infrared photograph of girder after approximately 22.5 hours of curing**

The data provided by Electro-Test Inc. with the limitations described previously has been examined. The location in the girder as specified in the received data was ambiguous. The locations along the girder shown in Figure 4.22 and Figure 4.23 may not have a high degree of accuracy. Since only half of each of the two short girders, SI and SX, were surveyed, it is assumed that the data shown in Figure 4.22 and Figure 4.23 represent data from the halves of two girders joined to show the temperatures along one representative girder. This point was not well documented by Electro-Test Inc.

Considering the possibilities of errors just described the maximum reported temperatures in the representative girder are presented in Figure 4.22 for several times during the curing of the girder. The drop in temperatures after the concrete cools in the evening is exhibited in the maximum temperatures at 17.5 elapsed hours. The temperatures begin to rise to the last reading

which showed an overall maximum temperature of 44.5° C (112.1° F) on the surface of the steel mold. This is to be compared with maximum-recorded internal temperatures in the prestressed girders of around 60° C (140° F).

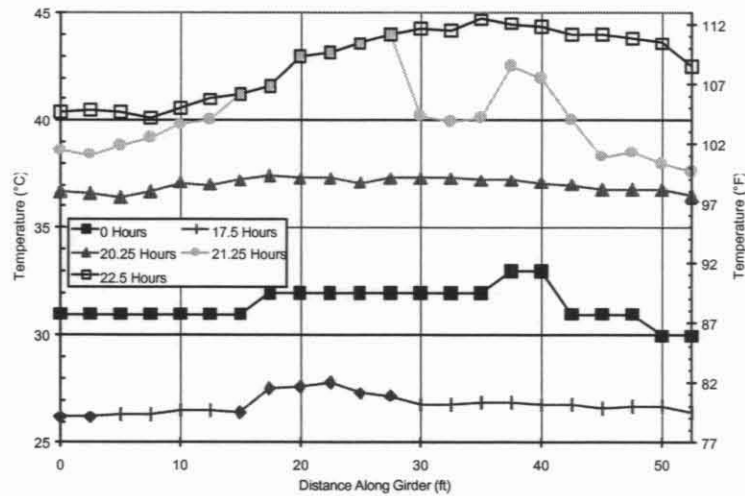


**Figure 4.22** Maximum temperatures along the length of the girder during curing (thermographic readings)

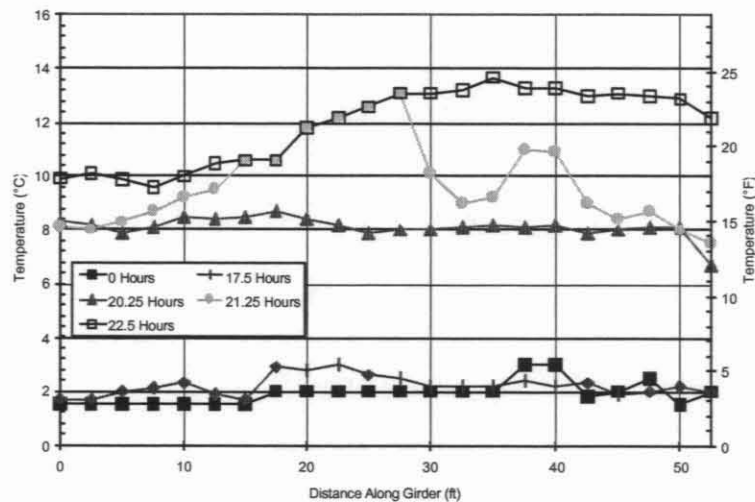


**Figure 4.23** Temperature gradients along the length of the girder during curing (thermographic readings)

Figure 4.23 shows the difference between the maximum temperatures and the minimum temperatures. It is important to note that the minimum temperatures may include the temperatures on the ribs of the forms or the tarp above the forms also. The maximum gradient shown by this measurement was almost 14° C (25.2° F). This is consistent with internal temperature measurements.

*This unnumbered page is intentionally left blank*

---

## 5. STRESS TRANSFER

### 5.1 Introduction

The time when the prestressing strands are cut is a critical time in the life of a girder. Internal strain readings were recorded and several external measurements were made to monitor the performance of the girders during this important period.

The long girders were cast at 8:30 a.m. on July 24, 1998 and transfer occurred at 4:00 p.m. on July 27, 1998, 3 days 7 1/2 hours after casting. Normally it is the practice of Egyptian Concrete Co to cut the prestressing strands earlier, but due to the specification that the concrete strength be at least 5,500 psi at transfer, more curing time was thought necessary. The strength of the concrete however significantly exceeded the specified strength at transfer. The short girders were cast at 9:20 a.m. on July 30, 1998 and transfer occurred at 4:30 p.m. on August 3, 1998. This allowed 4 days and 6 hours of curing before transfer.

The strands were cut using torches. The process of stress transfer is illustrated in Figures 5.1 and 5.2.

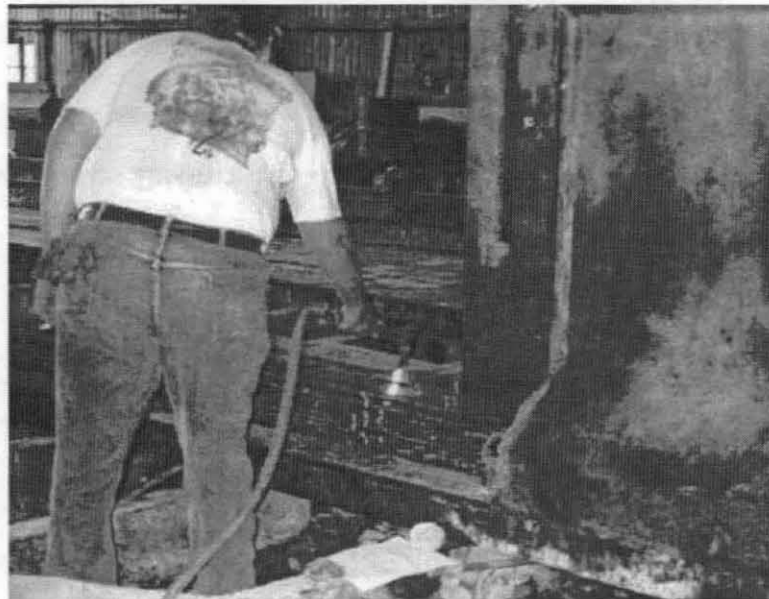


**Figure 5.1** Transfer of the prestress force

The sequence in which the strands are cut is important in preventing cracking caused by large stresses at intermediate steps of transfer. The order in which the strands of the short girders were cut is shown in Figure 5.3. All of the girders in Span 1-2 were cast together on the same

bed. The instrumented girders, SI and SX, were in the second and third spots from the north on the bed. Due to the equipment and manpower restrictions only two cuts are made simultaneously. Therefore each set of strands to be cut were cut at the ends, then the next interior space between girders, and then at the interior-most spaces. A diagram of the girder positions and cutting locations is shown in Figure 5.3 for the short girders. For example, Strands 1 and 2 would be cut at the far ends of the 5 girders first. Strands 1 and 2 would next be cut at the next inner space, Location 2, and then at the interior-most space, Location 3, before cutting Strands 3 and 4.



**Figure 5.2** Close-up of the process of cutting prestressing strands with a torch

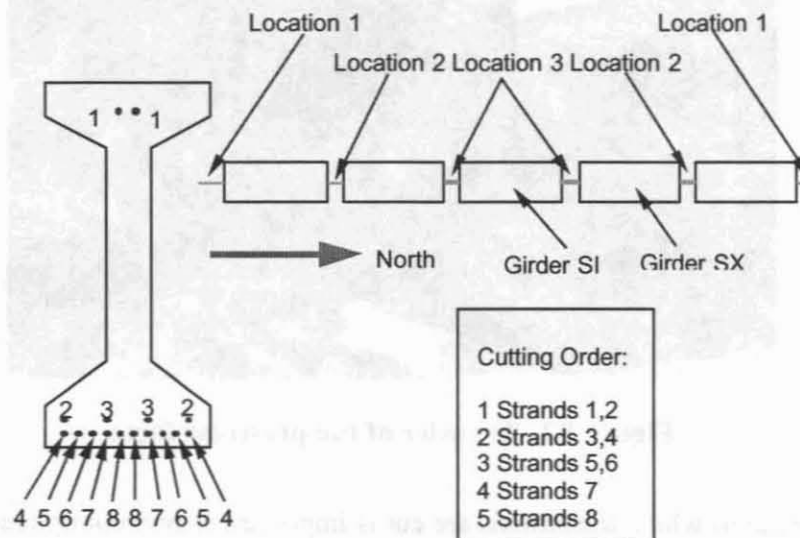


**Figure 5.3** Strand cutting sequence for short girders

The times that the strands were cut are given in Table 5.1 as an elapsed time from an arbitrary start time about a minute before the first strand was cut. The recorded time is the beginning of the strand breaking. Each strand takes between 2 and 7 seconds to fully fracture. The exact start time, which corresponds to zero elapsed time, was 4:26:12 p.m.

**Table 5.1 Elapsed time in minutes for prestress transfer operations of short girders**

Strand	Location 1	Location 2	Location 3
1	1.47 Minutes	2.52 Minutes	3.55 Minutes
1	1.68	2.67	3.70
2	1.92	2.85	3.83
2	2.08	3.03	3.98
3	4.80	5.70	6.63
3	5.00	5.85	6.80
4	5.12	6.05	7.00
4	5.30	6.22	7.15
5	7.77	8.73	9.70
5	7.98	8.95	9.88
6	8.13	9.13	10.05
6	8.32	9.33	10.20
7	10.82	11.42	11.93
7	10.98	11.58	12.12
8	12.73	13.28	13.87
8	12.90	13.48	14.13

The cutting sequence and girder locations for the long girders are shown in Figure 5.4. The two long girders were cast on a bed separately. Thus, only two locations for the cutting of each strand was necessary. The strand cutting times are given in Table 5.2. Near the end of the cutting sequence the hold downs were cut. These have been labeled in the table by girder and side of the girder where the hold down was located. Each girder had two hold downs, one on the north half and one on the south half. Tables 5.1 and 5.2 are useful while reviewing strain responses shown in Figures 5.5 – 5.10.

## 5.2 Internal Strain During Transfer

### 5.2.1 Strains During Transfer

Figure 5.5 illustrates progress in growth of strain accumulation with the cutting of each strand during transfer for the SXE cross-section. The steps show clearly the level of strain after

each strand was cut. The data shown was acquired at 3 second intervals for the short girders and 2 second intervals for the long girders. The datalogger uses an integration technique to reduce the amount of noise in signals that also filters out dynamic effects. The strain measurements, while intended to pick up strain variations after individual strand cuts, were not intended to measure dynamic effects due to the energy released by the prestressing strand during transfer.

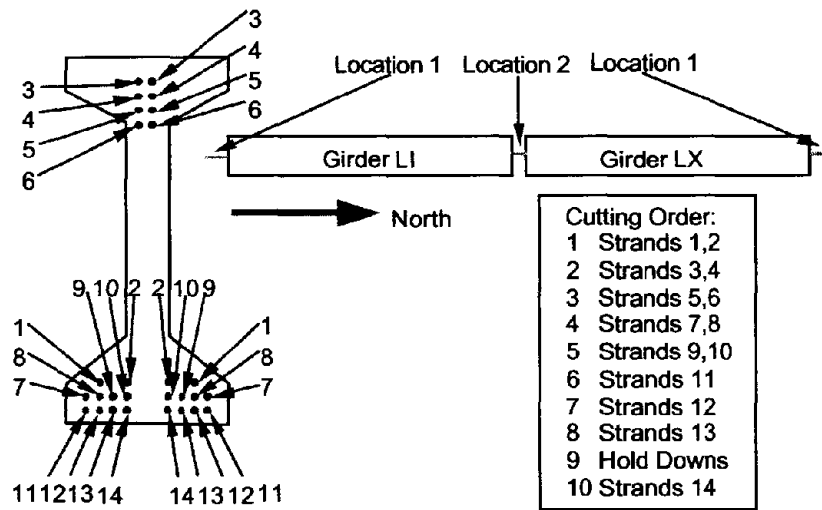


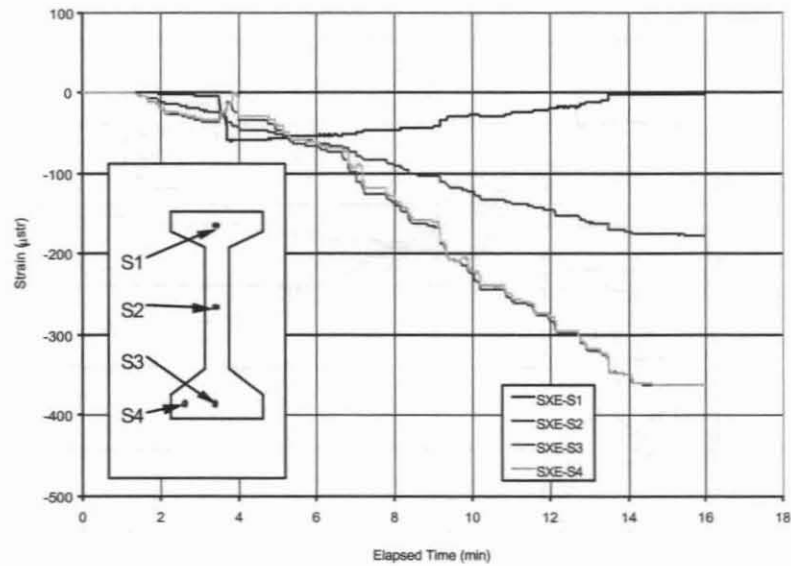
Figure 5.4 Strand cutting sequence for long girders

Table 5.2 Elapsed time in minutes for prestress transfer operations of long girders

Strand	Location 1	Location 2	Strand	Location 1	Location 2
1	1.03	2.23	9	11.55	12.65
1	1.22	2.40	9	11.73	12.77
2	1.42	2.57	10	11.92	12.93
2	1.65	2.73	10	12.18	13.07
3	3.55	5.42	11	13.75	14.47
3	3.73	5.63	11	13.93	14.65
4	4.28	5.85	12	15.30	15.98
4	4.48	6.02	12	15.48	16.17
5	6.80	7.73	13	16.77	17.43
5	6.88	7.88	13	17.03	17.57
6	7.05	8.07	LX N HD *	18.82	
6	7.20	8.28	LI N HD *	19.00	
7	9.32	10.42	LI S HD *	19.98	
7	9.52	10.62	LX S HD *	20.32	
8	9.73	10.77	14	24.03	24.82
8	9.90	10.92	14	24.23	25.02

\* HD - Hold downs for draped strands N - North S - South

Figure 5.6 shows the accumulation of strain during transfer for cross-section SIM. The accumulation of strain for cross-section SXE was similar to SIE and the accumulation of strain in cross-section SXM was similar to SIM so graphs for these cross-sections are not included. The end cross-section exhibited slightly more curvature than the mid-span cross-sections as will be shown clearly in later figures. The effect of dead load is a factor in the differences in curvature between the end and mid-span cross-sections. Also affecting these curvatures is the frictional effects at the girder ends.



**Figure 5.5 Strains during transfer of prestressing force for cross-section SXE**

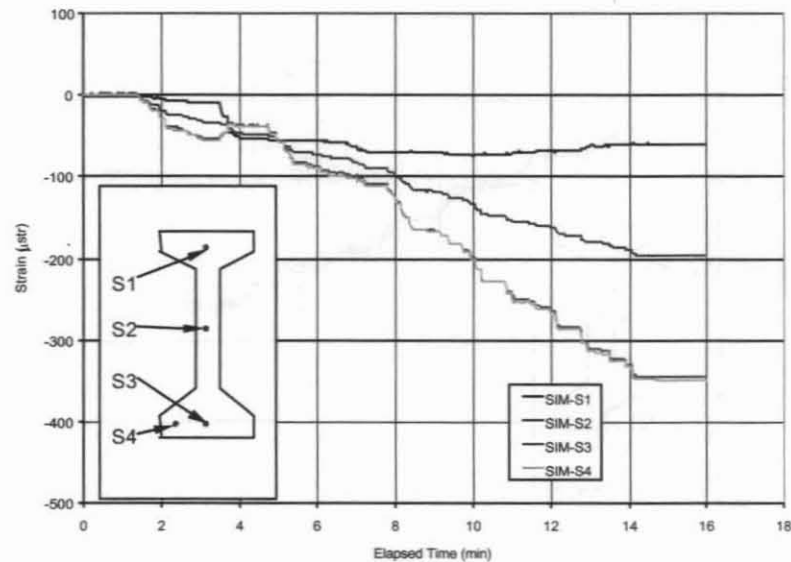


**Figure 5.6 Strains during transfer of prestressing force for cross-section SIM**

Figures 5.7 and 5.8 show the strains during transfer for cross-sections LXE and LIM respectively. Again, the response of cross-sections LIE and LXM were similar and are therefore not presented. The accumulation of strain during transfer was significantly different for mid-span cross-sections and end cross-sections in the long girders. This is due to the draped strands and the hold downs. The effect of the hold downs on the mid-span cross-section strain gradient is quite dramatic. The hold downs permitted virtually no curvature in the mid-span cross-section until they were cut. The section compressed as a unit until the hold downs were cut and camber was allowed.

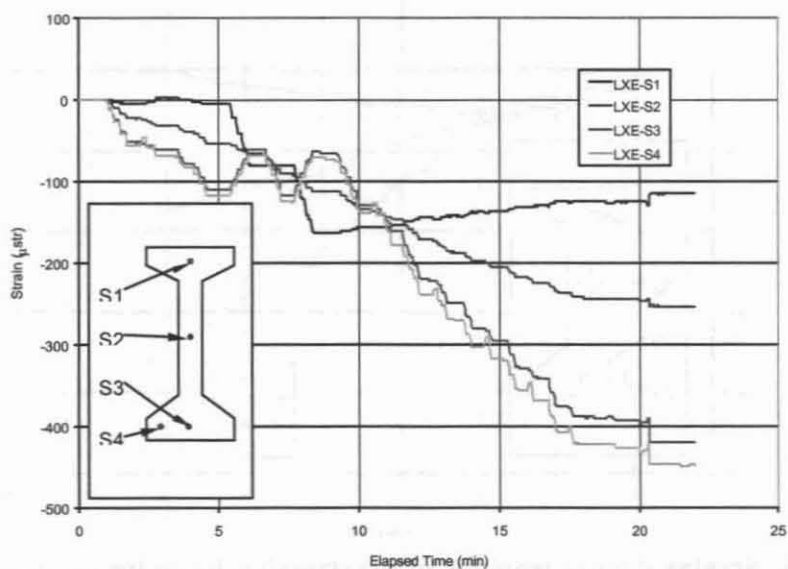


**Figure 5.7** Strains during transfer of prestressing force for cross-section LXE

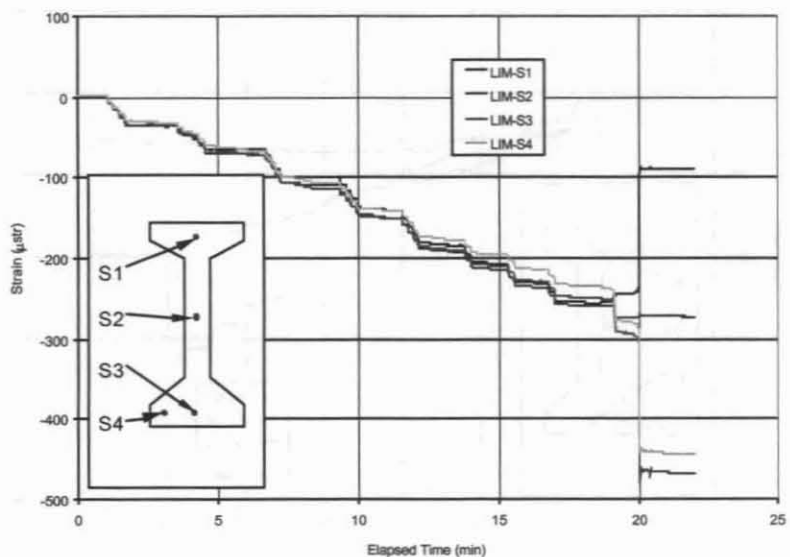


**Figure 5.8** Strains during transfer of prestressing force for cross-section LIM

Stirrup strains for girders SI and LI during transfer are shown in Figure 5.9 and Figure 5.10. The near stirrups, SIN and LIN, reached tensile strains of 25  $\mu$ str. In the section on end cracking it will be discussed that much larger vertical tensile strains may be seen closer to the end of the girder due to prestress forces.

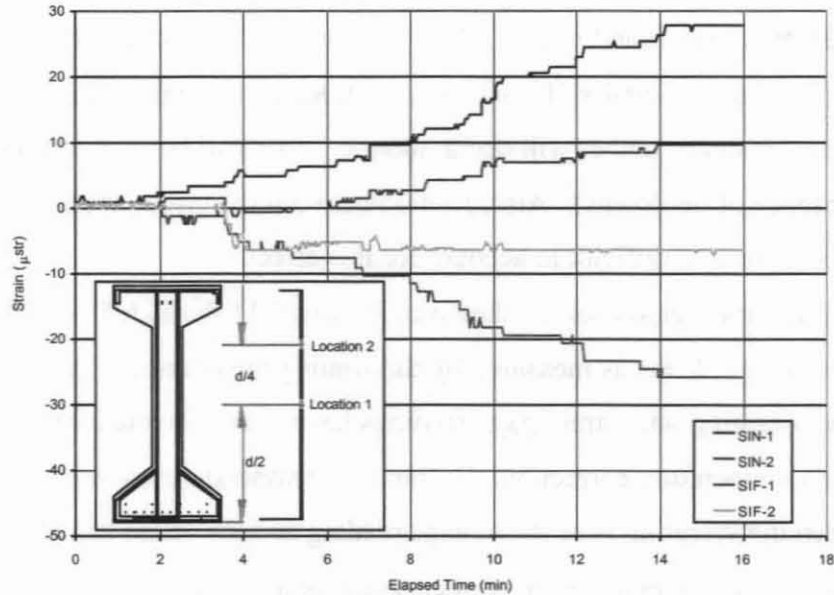


**Figure 5.9** Stirrup strains during transfer of prestressing force for girder SI

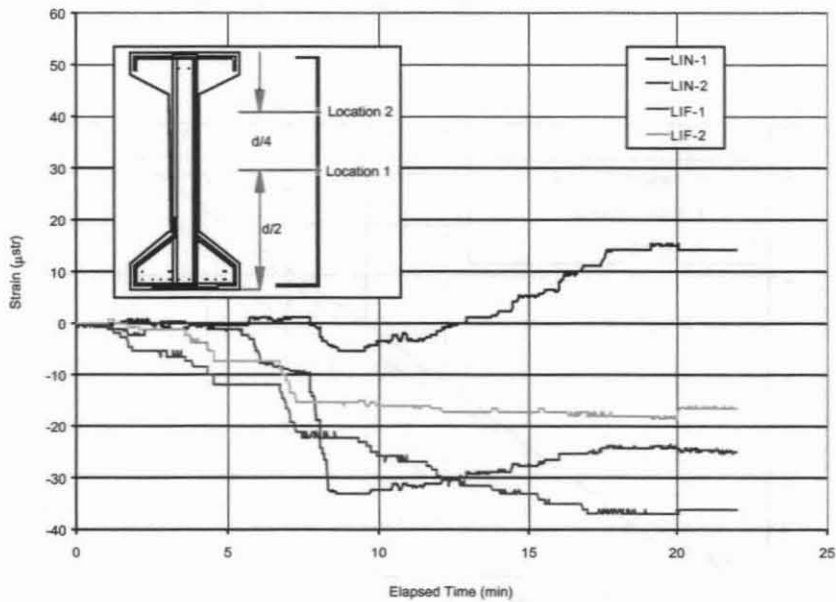


**Figure 5.10** Stirrup strains during transfer of prestressing force for girder LI

## 5.2.2 Analysis of Strains During Transfer

A theoretical solution for the strain gradient in each cross-section was obtained. One assumption that was made involves the modulus of elasticity of the concrete at the time of transfer. The 28-day compressive strength was taken to be 12,000 psi and the modulus at 3.125 days and 4.25 days was found using appropriate equations (Branson, 1977). The modulus for the short girders, 4.25 days, was found to be  $6.179 \times 10^6$  psi and the modulus for the long girders, 3.125 days, was found to be  $5.964 \times 10^6$  psi. The dead load was neglected in the solution, although after transfer some camber will occur and the girder will be carrying some of its own weight (in the absence of tie-downs). Also, friction between the girder and the bed has been ignored largely because it is difficult to account for this effect.

The resulting strain gradients are shown in Figures 5.11 through 5.14. These figures also show the actual strain gradients as measured by the strain-gaged bars and the vibrating wire strain gages. The vibrating wire strain gage readings have been corrected for temperature using the manufacturer's temperature correction. Without the temperature correction the average difference between the vibrating wire strain gage reading and the strain-gaged bar reading was  $+45\mu\text{str}$ . After applying the temperature correction for an average  $5^\circ\text{C}$  drop in temperature the average difference between the vibrating wire strain gage reading and the strain-gage bar reading was  $-28\mu\text{str}$ .

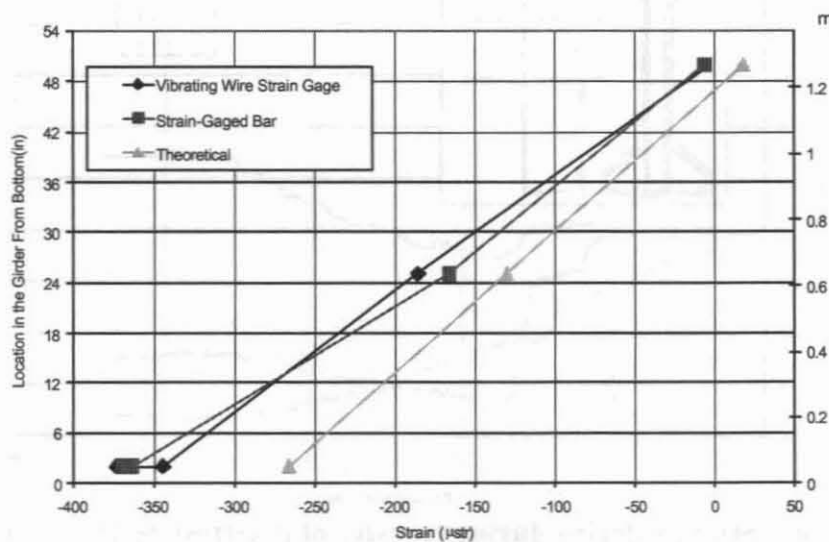


Figure 5.11 Strain distribution and gradient after transfer for cross-section SIE

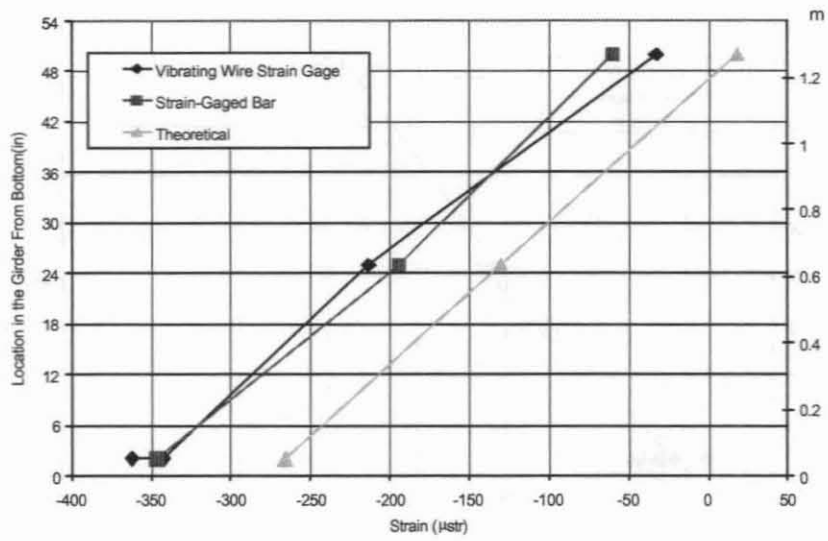


Figure 5.12 Strain distribution and gradient after transfer for cross-section SIM

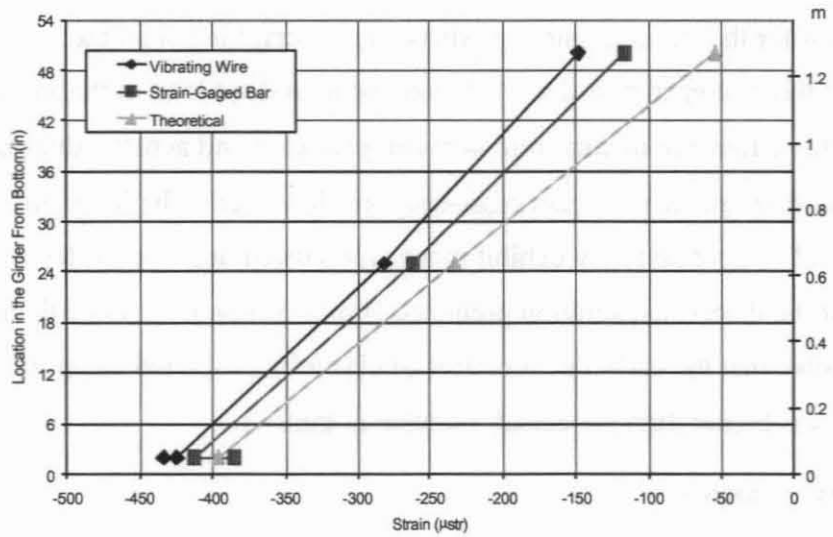
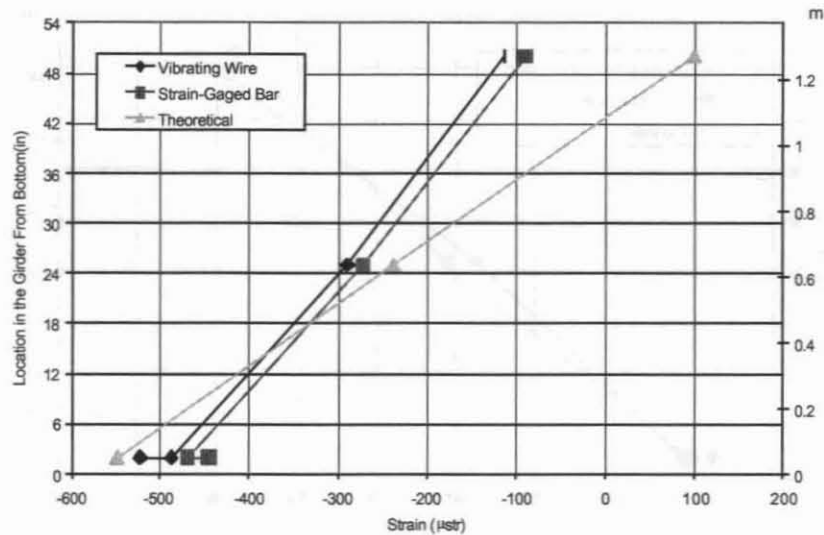


Figure 5.13 Strain distribution and gradient after transfer for cross-section LIE



**Figure 5.14** Strain distribution and gradient after transfer for cross-section LIM

From Figures 5.13 and 5.14, it is clear that in the long girder mid-span cross-sections the theoretical solution for the strain gradient predicts larger curvatures than the measured strains exhibit. Some of this discrepancy is due to the exclusion of dead load in the analytical computations. This difference in curvature between predicted and actual values is not as pronounced in the short girder mid-span cross-sections, however. The long girders experience a larger magnitude of camber and may exhibit more pronounced dead load effect.

In general the theoretical solution predicted strains of less magnitude than the measured strains. It is possible that the early-age modulus of elasticity estimated using the ACI formula (Branson, 1977) was higher than the actual modulus at transfer.

### 5.3 Camber Measurements

Measurements of deflection were made before transfer, after transfer, and after the girders were moved off the bed. The camber measurements are shown in Figures 5.15 and 5.16 for short and long girders, respectively, including both the camber immediately after transfer and the camber after the girders were moved off the bed. A small shift in the deflection was noted for all girders after the girders were moved off the bed (except SX which had a large shift). This shift can in part be attributed to friction between the girders and the bed.

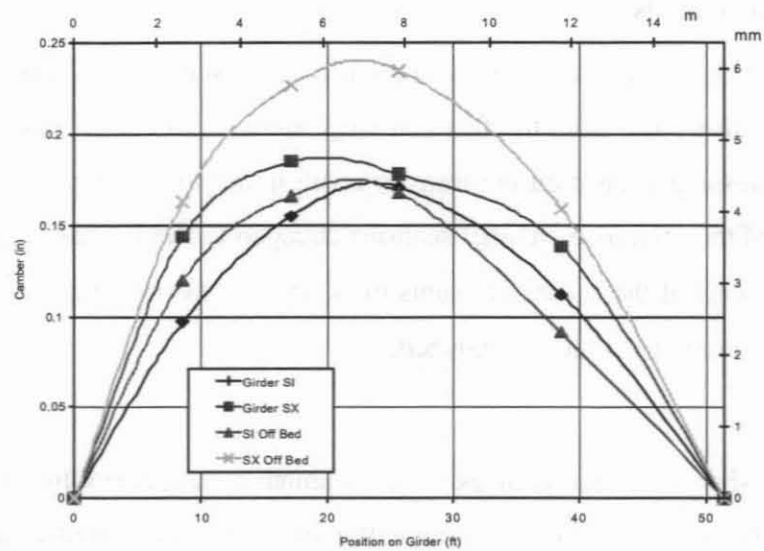


**Figure 5.15** Camber profiles after prestress transfer for the short girders

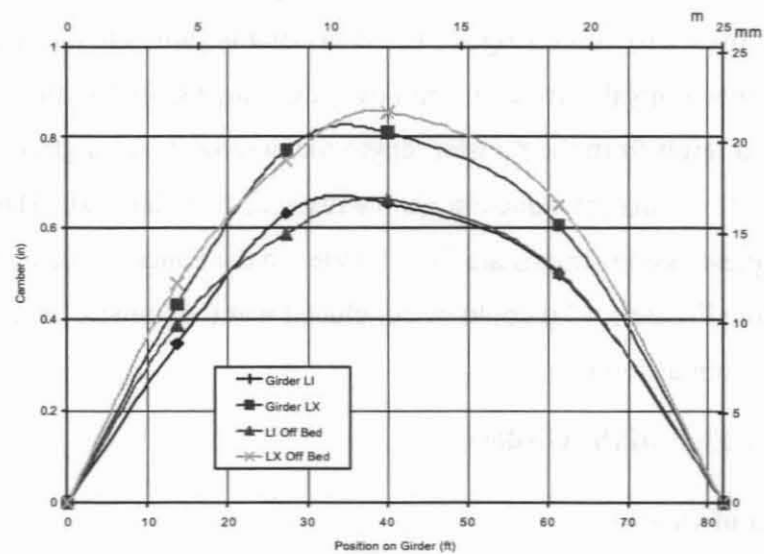


**Figure 5.16** Camber profiles after prestress transfer for the long girders

The expected camber obtained by considering only prestress force with no dead load or friction forces, was found to be 0.86" for the long girders and 0.28" for the short girders. The camber of the girders at mid-span immediately after transfer was 0.633", 0.664", 0.171", 0.178" for girders LI, LX, SI, and SX respectively. The measured camber was lower than the expected values.

## **5.4 End Slip Measurements**

The problems with the end slip measurement were described in Chapter 2. These measurement difficulties stem from the fact that large amounts of elastic strain energy released by cutting the prestressing strands during transfer result in the strand unraveling. This in turn causes movement of the reference channel sections clamped to the strands. Since end slips are small, small movements of the reference points made these measurements unreliable. Hence, these measurements are not plotted or analyzed.

## **5.5 Transfer Length**

Figure 5.17 shows the results of the transfer length measurement for girder LI using the Whitmore gage. Mechanical strain measurement, particularly measurement of small strains, is not as reliable as electrical strain measurements. The transfer length measurements for the other three girders exhibited more scatter than that shown for girder LI. Each data point represents the strain measurement over a 10" gage length. The data point is shown in the center of the 10" gage length but actually represents the average strain over the whole gage length.

The expected result from the transfer length measurement was a gradual increase in strain from zero at the end to a constant value after some distance from the end. This distance to the point at which the prestressing strands are fully bonded to the concrete surrounding them, is the transfer length. From Figure 5.17 it could be concluded that the transfer length occurs at some point beyond 25 in from the end.

## **5.6 Cracking in the Ends of the Girders**

### **5.6.1 Description of Cracks**

After transfer of the prestress force girders LI and LX were moved off the bed to sit inside the casting building near the opening. Some cracks at the girder ends became visible on wetting the girders. This was 6 days after casting and 3 days after transfer. At this time the only forces acting were dead load, prestress force and residual stresses from the hydration / hardening process.

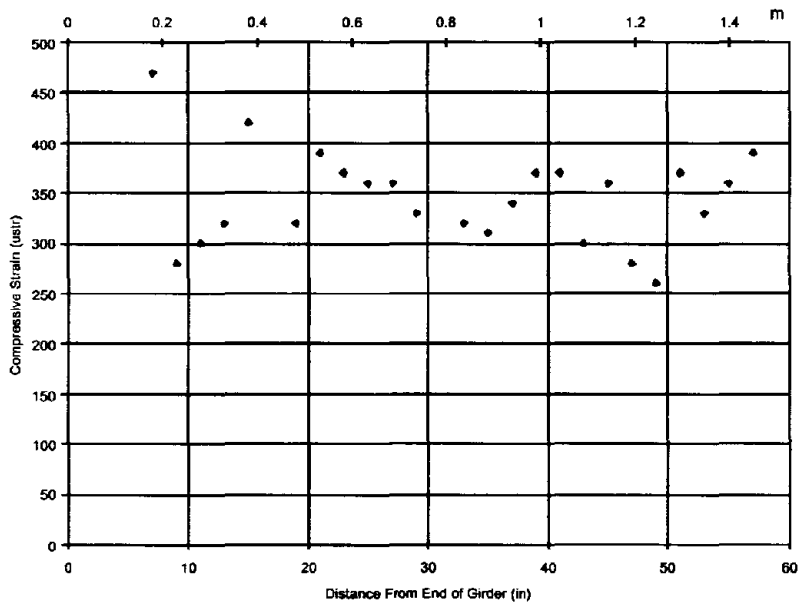


**Figure 5.17 Transfer length measurement results**

Water was retained at the locations of cracks while the surface around them would dry. The cracks would not have been readily visible without this surface wetting process. Spray bottles were used to wet the ends of both girders. The cracks were examined and recorded. Similar cracks were noted on the short girders. These cracks consisted of horizontal cracks in the web but not the diagonal cracks noted in the long girders.

The cracks were of two types. Several horizontal cracks in the web were found which extended up to 12" along the beam. Diagonal cracks were also found which began at the intersection of the top flange of the web and extended up to 24" along the beam angling downward. A photograph of the girder-end cracking is shown in Figure 5.18. The cracks in the ends of the long girder (LI and LX) as they appeared on July 30, 1998 and as updated on August 10, 1998 are shown in Figures 5.19 and 5.20, respectively.

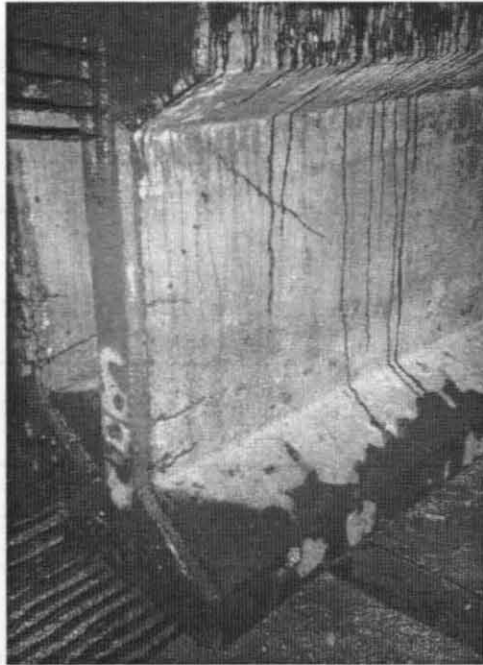


**Figure 5.18** Photograph of girder end cracking

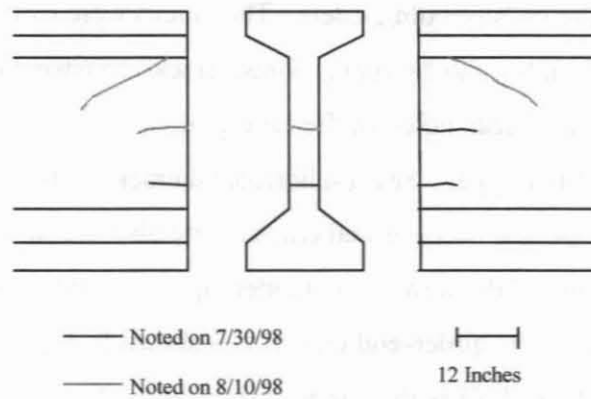


**Figure 5.19** Sketches of girder-end cracks for the “marked end” of girder LI

### 5.6.2 Anchorage Zone Stresses

The prestress force is transmitted to the concrete in pretensioned concrete girders at some distance away from the girder end. Beyond this transfer length a linear stress distribution based on the overall eccentricity of the prestress force can be computed. This linear stress distribution occurs after a distance less than the height of the beam from the point of application of the force.

The stress patterns flow from the point of application into this linear stress distribution causing vertical tensile stresses in the beam near the end of the beam.

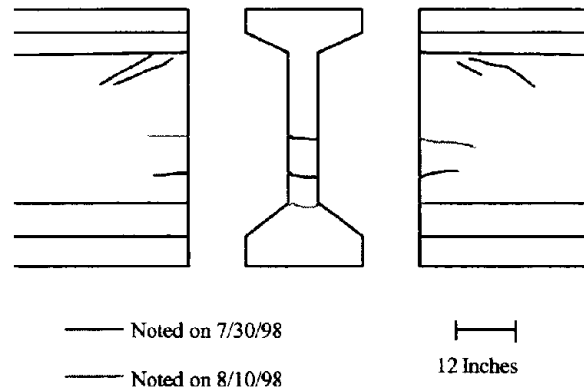


**Figure 5.20 Sketches of girder-end cracks for the “marked end” of girder LX**

Gergely and Sozen (1967) proposed a method for determining the stress in anchorage zone vertical reinforcement for design purposes. This method is based on analyzing a section at the bottom end of the girder and computing the resulting moment on the top face of this free-body. Since it is accepted (based on empirical observations reported by Gergely and Sozen) that the stress distribution becomes linear after a distance equal to the height of the girder from the point of load application, Gergely suggests using a cut of this length. In the method for anchorage zone reinforcement design the moment is then converted into a resultant vertical reinforcement resultant by assuming a moment arm. Gergely suggests using the distance from the centroid of the vertical reinforcement to the end of the cut as a conservative assumption.

Several modifications to the Gergely-Sozen model have been proposed (Earney, 2000). Gergely and Sozen assumed that the stress would be a maximum at the interface of the bottom flange bulb and the web. It was observed, however, in the girders that exhibited this type of horizontal cracking, that the cracks were higher in the web than this (Figure 5.18-5.20). By solving for the unbalanced moment as a function of the amount of web included in the section, it can be shown that the maximum moment occurs higher in the web. This model is shown in Figure 5.21 with the unknown depth above the bottom flange bulb labeled “y”. The unbalanced moment is solved in terms of “y”.

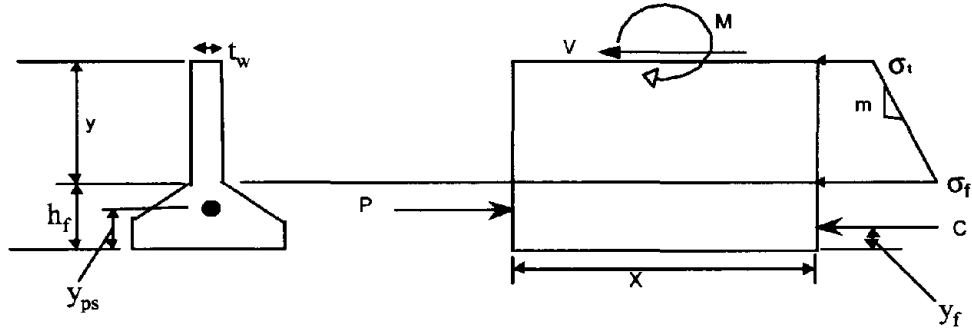


**Figure 5.21 Modified Gergely – Sozen model (Earney, 2000)**

$$M = P(y + h_f - y_{ps}) - C(y + h_f - y_f) - \left( \sigma_f - \frac{y}{3m} \right) y^2 \frac{t_w}{2} \quad (5.1)$$

Computing the first derivative of Eq. 5.1 and setting it equal to zero allows establishing the depth at which the moment reaches a maximum value. This depth is given by:

$$y = \frac{\sigma_f \cdot t_w \pm \sqrt{(\sigma_f \cdot t_w)^2 - 2 \frac{t_w}{m} (P - C)}}{\frac{t_w}{m}} \quad (5.2)$$

All parameters used in Eqns. 5.1 and 5.2 are illustrated in Figure 5.21 and are described in the List of Notations.

In order to find the stress in the girder end due to this moment, a length of girder must be used (labeled “x” in Figure 5.21). Gergely and Sozen had suggested that “x” be assumed equal to the total height of the girder. For a pretensioned girder, it is expected that this length should at least be equal to the transfer length. Since data from stirrup strains during prestress transfer operations for the HPC project (Eatherton, 1999) were readily available, it was possible to evaluate the Gergely-Sozen recommendation for girder length to be considered. Two stirrups were instrumented in the ends of each of the 4 girders as shown in Figures 2.8 and 2.9. One stirrup is located a distance “d/2” from the end of the girder, and the second is located “d” from the end. Additionally, these stirrups are each instrumented at two locations along the height of the stirrup, Figure 2.3. The strains at d/2- and d -away were opposite in sign suggesting that the point of “zero-strain” occurs somewhere between these two locations. As illustrated in Figure 5.22, this point of “zero-strain” is located x/2 from the end for the Gergely – Sozen model. Due to the limited number of experimental data points, the influence of girder geometry, prestressing force used, prestressing profile, and transfer length on the location of “x” cannot be ascertained

for a general case. However, for Type VI MoDOT girders used in the HPC project this location can be established experimentally from the data available (Eatherton, 1999).

The strain data, as well as the calculated distance (based on linear interpolation),  $x$ , are shown in Table 5.3. The use of a linear distribution produces a strain distribution similar to that measured by Marshall and Mattock (1962). If the Gergely – Sozen assumption is used, this distance would be  $d/2 = 27$  inches for both girders. This length is shorter than that computed from experimental measurements of stirrup strain and produces stresses that are significantly higher. Table 5.4 lists the computed values for maximum unbalanced moment for each of these girders, the corresponding location, and the maximum vertical tensile stress produced using the Gergely – Sozen assumption for  $x$ , as well as the experimentally computed length,  $x$ .

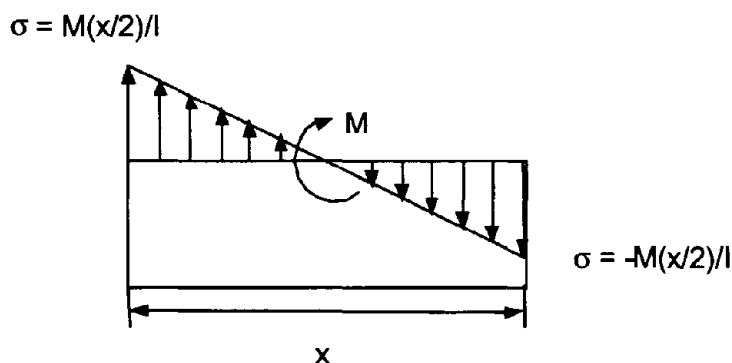


Figure 5.22 Assumed stress distribution from unbalanced moment

Table 5.3 Experimental determination of zero strain location from stirrup strain data

Gage Location	Strain at $d/2$ ( $\mu\text{str}$ )	Strain at $d$ ( $\mu\text{str}$ )	Location of zero strain, $x/2$ , from girder end
Top of Short Girder	10.0	-6.0	43.9
Middle of Short Girder	28.0	-25.0	41.3
Top of Long Girder	--	-18.0	--
Middle of Long Girder	15.0	-36.0	34.9

**Table 5.4 Maximum tensile stress and location due to prestress transfer using the Gergely – Sozen model**

Girder	Location of Max. Moment (in.) From bottom of girder	Maximum Unbalanced Moment, (k-in)	Max. Tensile Stress (psi) Experimental data	Max. Tensile Stress (psi) Gergely – Sozen assumption
Long	23.0	2360	349	747
Short	20.4	1749	315	554

The maximum tensile stresses in the girder ends due to prestress transfer (~350 psi) are approximately 40% to 50% of the tensile strength of concrete (~550-750 psi). While these stresses by themselves may not be sufficient to cause cracking, when they are considered in conjunction with the residual tensile stresses due to hydration/curing gradients, discussed by Earney (2000), horizontal girder-end cracking is possible. These conclusions were also speculated in the Marshall and Mattock (1962) paper and discussed in more detail by Gamble et al. (1997). However experimental data from instrumented stirrups at girder ends were unavailable to them to make quantitative observations.

## 6. STORAGE, TRANSPORT, AND CONSTRUCTION

### 6.1 Transporting the Girders to the Yard

#### 6.1.1 General

The long girders were moved off of the precast bed on July 28, 1998. They were moved to sit inside the casting building for several days before being moved into the yard for long-term storage. The casting building utilizes two overhead cranes to move the girders. When moving the girder into the yard, a truck is brought into the building and the cranes are used to place the girder onto the truck. In the yard a gantry crane is used to lift the girders off the truck and place them in a long-term storage area. This process of transferring the girder from the truck to long-term storage is shown in Figure 6.1.



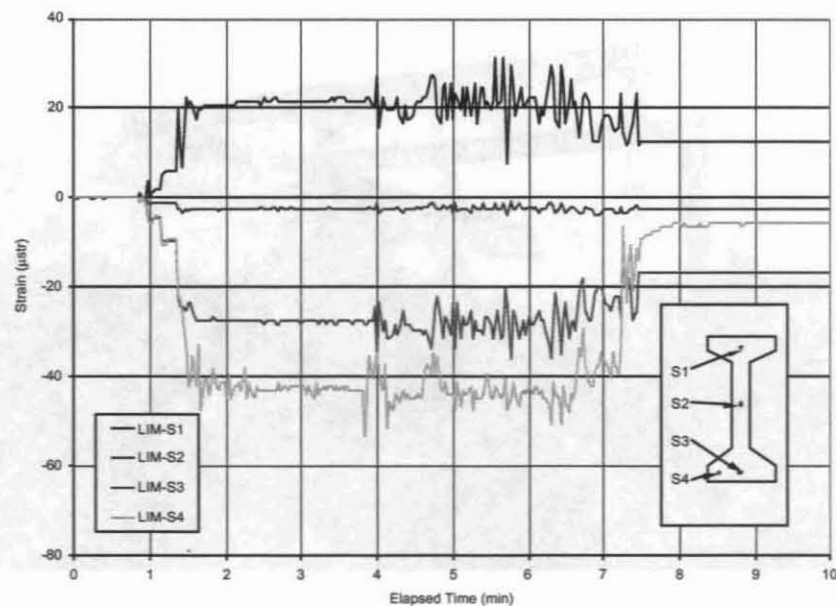
**Figure 6.1 Gantry crane used to move girders**

The short girders were moved off the bed directly onto a truck and taken into the storage yard. This occurred on August 7, 1998. A program was sent to the datalogger that recorded readings from the strain-gaged bars at a data acquisition interval of 2 or 3 seconds. As mentioned in the section on prestress transfer, the datalogger uses an integration technique that removes noise in the data along with some of the dynamic effects. The true maximum and

minimum strains therefore may be marginally larger than the values shown in the figures. Strains were recorded for the movement of the long girders off the bed, and for all girders as they were moved into the storage yard.

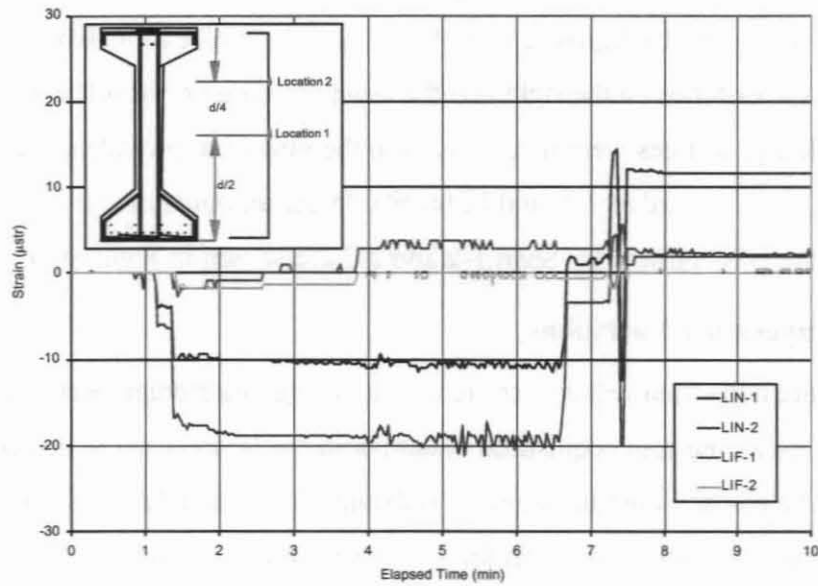
### 6.1.2 Strains During Movement to the Yard

Figure 6.2 shows the strains in the LIM cross-section as girder LI was moved off of the bed into short-term storage at the casting building. As the girder is picked up strains are induced in the cross-section by the change in support conditions. The strain gradient is also be due to a release of friction between the bed and the girder, which, after transfer reduced the amount of curvature in the cross-section. At an elapsed time of 1.5 minutes the girder was just barely lifted. At 4 minutes of elapsed time the girder was raised high and moved over its resting spot. There is a noticeable increase in the amount of activity in the strain readings at this time. The magnitudes of strain shown in Figure 6.2 are representative of the strains noted in the other girders during movement to the yard.



**Figure 6.2 Strains in girder LI while the girder is being moved from the precasting bed**

Figure 6.3 shows the stirrup strain readings in girder LI during the same time frame (as in Figure 6.2). Compressive strains of 20 µstr were noted in the upper instrumentation location of the stirrup at a distance of  $d/2$  from the end of the girder.



**Figure 6.3** Stirrup strains while girder LI is moved from the precasting bed

## 6.2 Storage in the Precast Plant Yard

### 6.2.1 Storage Location

The girders were stored in the precast yard between early August and early October of 1998. For approximately two months the girders sat in the positions shown in Figure 6.4.



**Figure 6.4** Storage of the girders at the precasting yard prior to bridge construction

The girder on the far right in the foreground is girder LX. The girder to its left is LI. The girder on the far right in the background is girder SI, and the girder to its left is SX. The batch plant is shown in the distance on the right and the large building on the left is the casting building. No buildings or trees were near enough to the girders to provide shade. The picture was taken facing north, so girders LX and SI receive larger amounts of sunlight especially in the morning. All of the HPC girders for Span 1-2 and 2-3 are shown in Figure 6.4.

### 6.2.2 Daily Temperature Variations

Temperature and strain values were recorded during this storage period at the precasting yard. Figure 6.5 shows the data acquisition system with the laptop used to download measurements. The elapsed time in Figures 6.6 through 6.11 started at 6:00 p.m. on August 20, 1998. The ambient temperature variation for a five-day period is shown in Figure 6.6. The ambient temperatures for this time period ranged from 19° C (66.2° F) to 42° C (107.6° F). The heat was transmitted by radiation and convection to the girders. Figure 6.7 shows the temperatures at several locations during this same five-day period. The maximum temperatures are noted in the center of the top flange. The temperatures in the top flange reach a maximum at approximately the same time as the ambient temperatures, but are slightly larger, reaching a maximum of 47.6 ° C (117.7° F). The temperatures in the rest of the girder were lower especially in the bottom flange. The temperatures in the web reached a maximum slightly after the top and bottom flange.

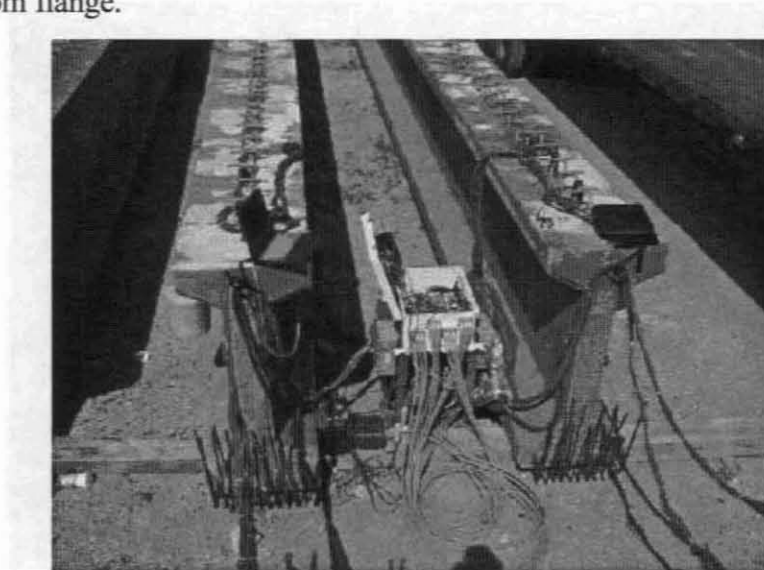
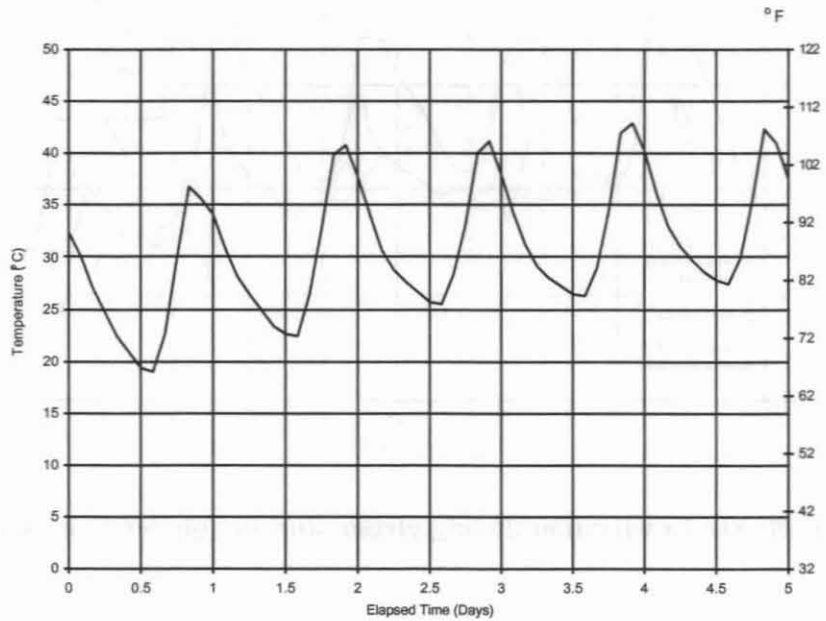
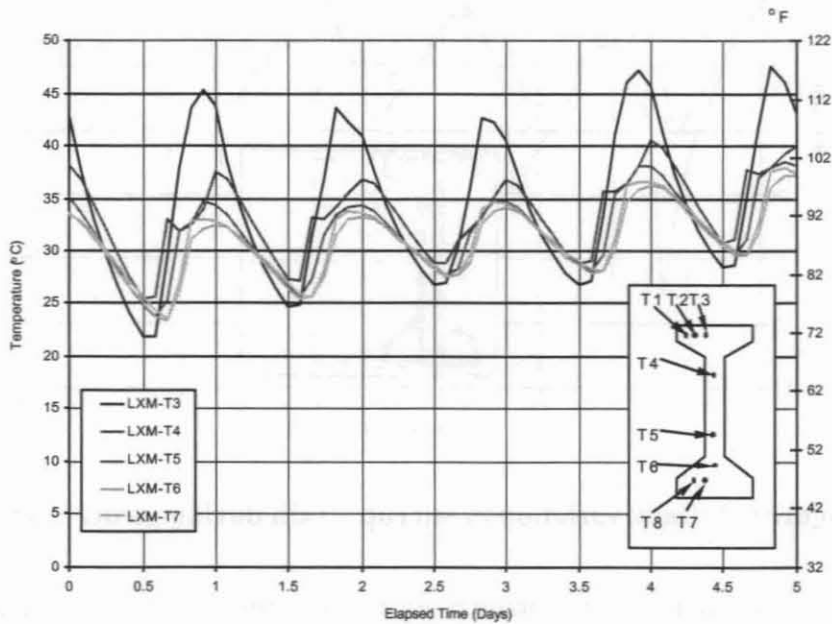


Figure 6.5 Acquiring data during the girder storage period

This process of differential heating created temperature gradients in the girders. The temperature gradient would reach maximums consistently at 2:00 p.m., and for the time period and cross-section shown in Figure 6.7 reached a maximum of 13.3° C (24° F).



**Figure 6.6 Daily variations in ambient air temperature**



**Figure 6.7 Temperature gradients in cross-section LXM due to daily ambient temperature variations**

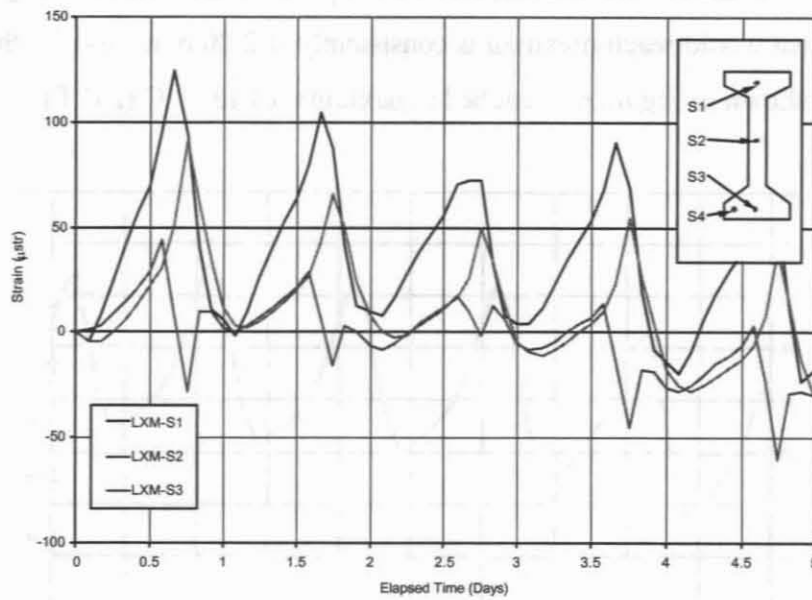


**Figure 6.8 Daily strain variation during girder storage (girder cross-section LXM)**

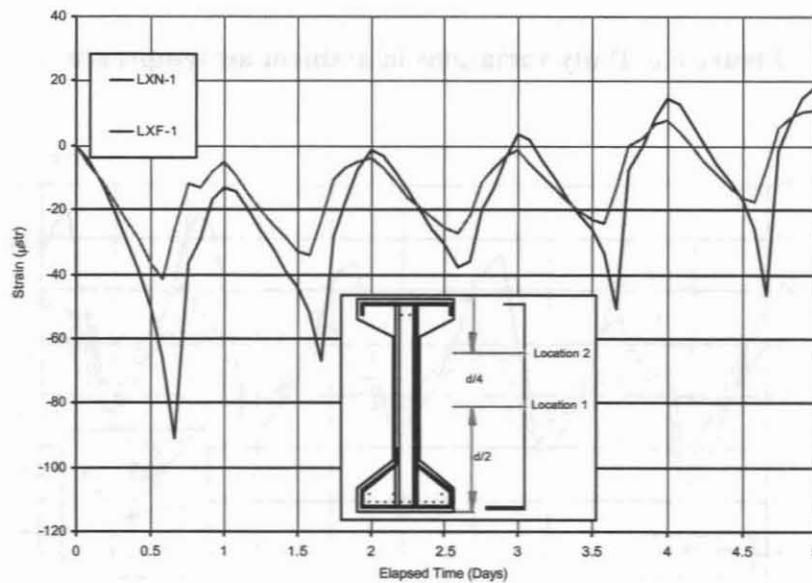


**Figure 6.9 Daily variation in stirrup strain during girder storage**

There was a difference in temperatures for the two girders sitting on the outside of the group compared to the girders sitting in partial shade from the other girders. Girders SI and LX were sitting on the east side of the girder group, as opposed to SX and LI which were sitting to

their immediate west. For girder LI the maximum temperatures were in the top flange and reached magnitudes similar to those shown for girder LX. The web and bottom flange temperatures were up to 5° C below the corresponding location in girder LX. Girder SX exhibited lower temperatures overall than girder SI.

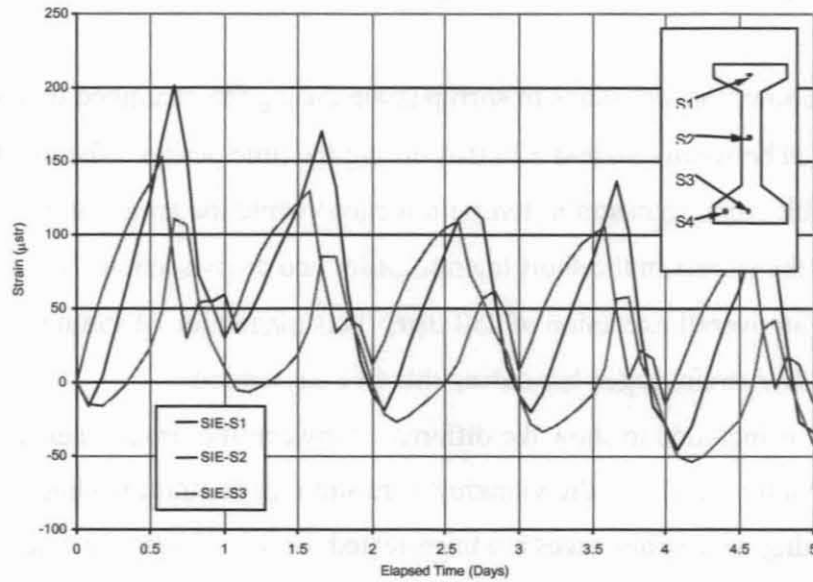


**Figure 6.10 Daily variation in strain during girder storage (girder cross-section SIE)**

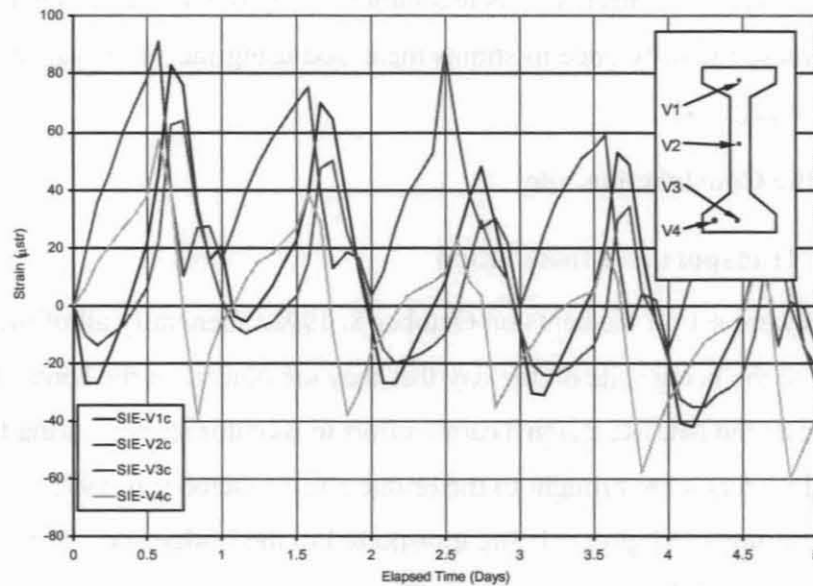


**Figure 6.11 Daily strain variation measured using the vibrating wire strain gages (girder cross-section SIE)**

### **6.2.3 Strains Due to Daily Temperature Variations**

As a result of the temperature changes and temperature gradients, strain gradients were also induced in the girder. Figure 6.8 shows the strains in the same cross-section (LXM) as Figure 6.7. The top flange strain gaged bar (LXM-S1) exhibits an excursion of 148  $\mu\text{str}$  during these five days. It can be seen that the top flange exhibits a larger strain variation than the rest of the section.

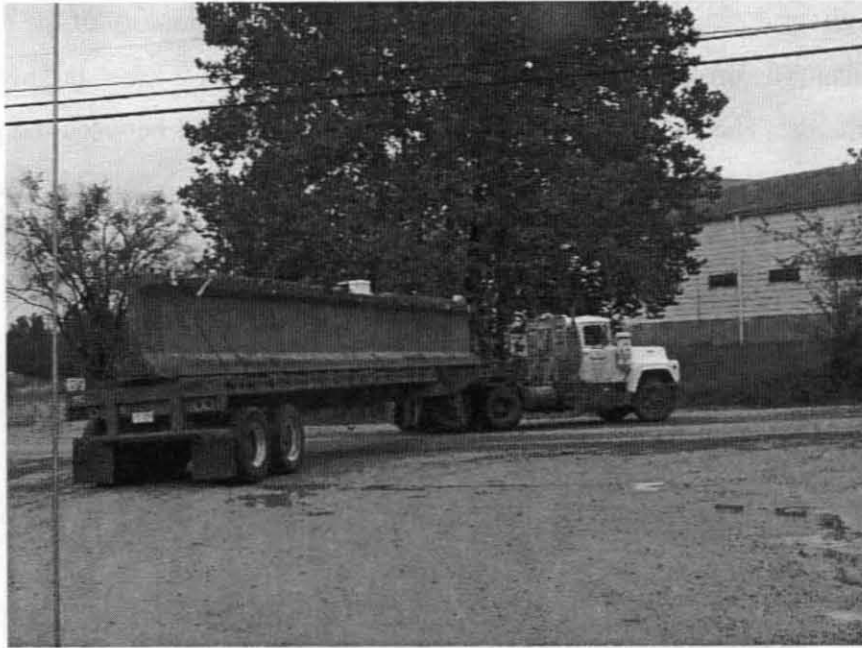
Figure 6.9 shows the variations in stirrup strain during the examined time period. The stirrup strains ranged between  $-90$  and  $+20$   $\mu\text{str}$  during the time period. The trend of the stirrup strains was to exhibit increase in strain (tensile direction) while the temperatures were increasing. Figure 6.10 shows the strains in the short interior girder end cross-section. The top flange strain-gaged bar exhibits an overall excursion of 250  $\mu\text{str}$ . This magnitude of strain was the largest excursion noted in any strain-gaged bar during this five day period.

Figure 6.11 is included to show the difference between the strain reading in the strain-gaged bar and the strain reading in the vibrating wire strain gage strain reading. The values of strain for the vibrating wire strain gages are uncorrected for the effects of temperature. With excursions of  $20^{\circ}$  C the manufacturers temperature correction would be on the order of 250  $\mu\text{str}$  in some places. Maximum temperatures happen at the same general times and the shape of the strain curves are similar for each individual gage, but it is clear by the comparison of magnitudes that a temperature correction is needed. As recommended by the manufacturer, the correction would actually increase the difference in strains measured using the strain-gaged bar and the vibrating wire strain gage.

## **6.3 Transport to the Construction Site**

### **6.3.1 Process of Transport and Installation**

The girders were set on the bents on October 8, 1998. Generally all of the girders would have been brought to the bridge site on the day that they are placed on the bents. However, in order to accommodate the MU Research Team's effort to monitor strains during transport the short-instrumented girders were brought to the bridge site on October 6, 1998. Figure 6.12 shows one of the instrumented girders being transported to the bridge site. The girders were supported at the ends and tightly chained down at two places on each end. Figure 6.12 clearly shows the main data acquisition box sitting atop the girder during transport.



**Figure 6.12** Transporting the girder to the bridge site



**Figure 6.13** Setting the instrumented girders on the bents

Once at the bridge site the girders would sit for a period of time, between a couple minutes and a couple hours, until it was time for the girder to be placed on the bents. Figure 6.13 shows the girder being lifted to be placed on the bents. The data acquisition box (white box) can

be seen on the girder during this stage also. Figure 6.14 shows a close up of the end of the girder being set in place. The prestressing strands were cut at a length of 2 ½ feet and bent vertical 6” from the girder ends. The strands are meant to mesh into each other between the girders and provide better continuity through the diaphragm. The deflection weights were tied up during transport and re-hung after all the girders were placed on the bents. The terminal boxes were secured to the girder with steel straps.

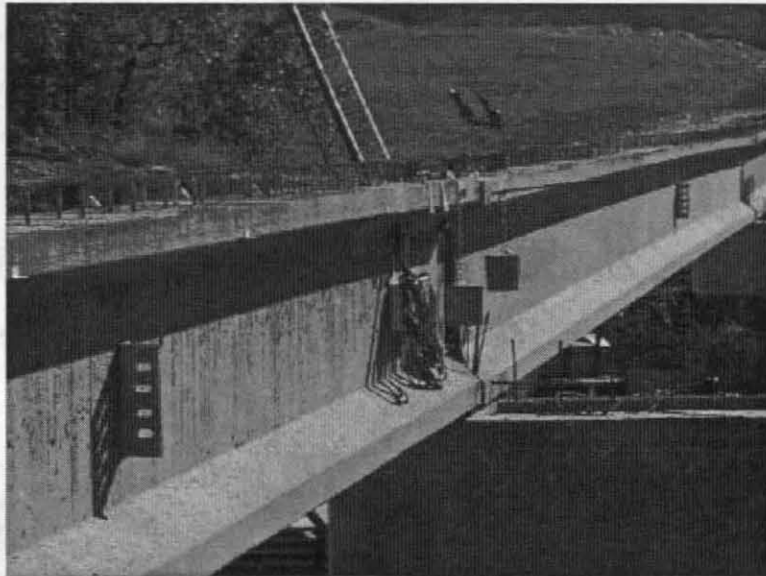


**Figure 6.14 Instrumented girders in place on bents**

### **6.3.2 Transport Strains**

Strains were recorded during the transport of every girder to the bridge site and while the girders were being placed on the bents. Figure 6.15 shows the strains during transport for girder SX (cross-section SXE). The short girder cross-section SXM shows similar trend to the end cross-section. There is an increase in the magnitude of strains in the mid-span cross-section compared to the end cross-section which can be attributed to the tie-downs at the ends. The long girder mid-span cross-section strains were greater in magnitude than the corresponding short girder cross-section. Magnitudes of strain between +50  $\mu$ str to -40  $\mu$ str were noted. Figure 6.15 represents typical behavior also observed for all the other instrumented girders.

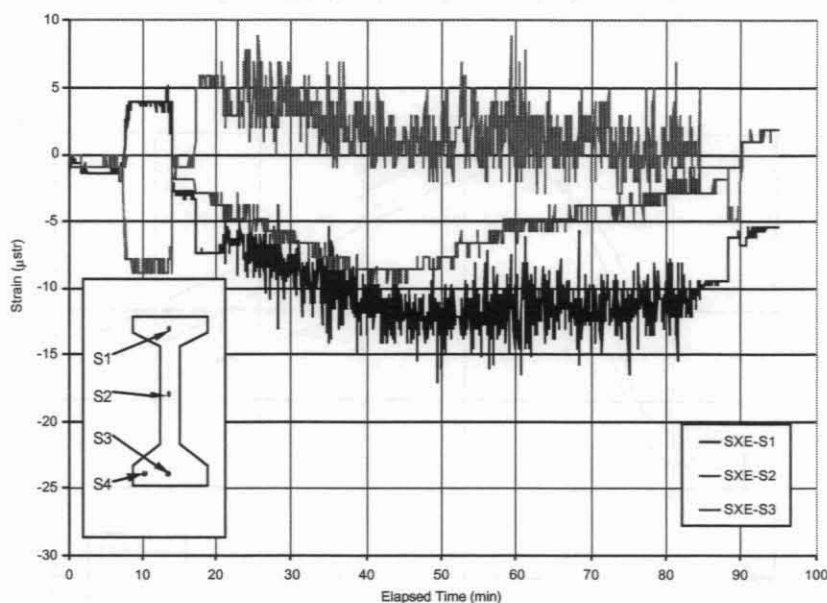


**Figure 6.15** Strains during girder transport to the bridge site (girder cross-section SXE)

## 6.4 Curing of the Diaphragm

### 6.4.1 General

The precast slab panels were set, the deck steel was placed, and the diaphragm forms were installed during October 10-21, 1998. The diaphragms and slab were simultaneously cast on October 21, 1998. This construction took most of the day. Thermocouples and strain-gaged bars were placed in the diaphragm and slab as described in Chapter 2. Temperature and vibrating wire strain gage readings were taken while the diaphragm was being cast and cured. The strain-gaged bar readings were not recorded during this period due to temporary problems with the excitation voltage.

### 6.4.2 Temperatures During Diaphragm and Slab Casting/Curing

The temperatures in the diaphragm during curing were recorded. Figure 6.16 shows the temperatures in three locations during curing. Since the casting of the diaphragm and slab were of extended duration, the elapsed time begins when the casting started, instead of the end of casting, as was the case for the girder curing graphs. The diaphragm instrumentation locations correspond with the heights of the instrumentation in the girders (Figure 2.4). Location 1 therefore is the highest instrumentation, while 2 is in the middle and 3 is in the bottom of the

diaphragm. The maximum measured temperature in the diaphragm reached a magnitude of 58° C (136.4° F).

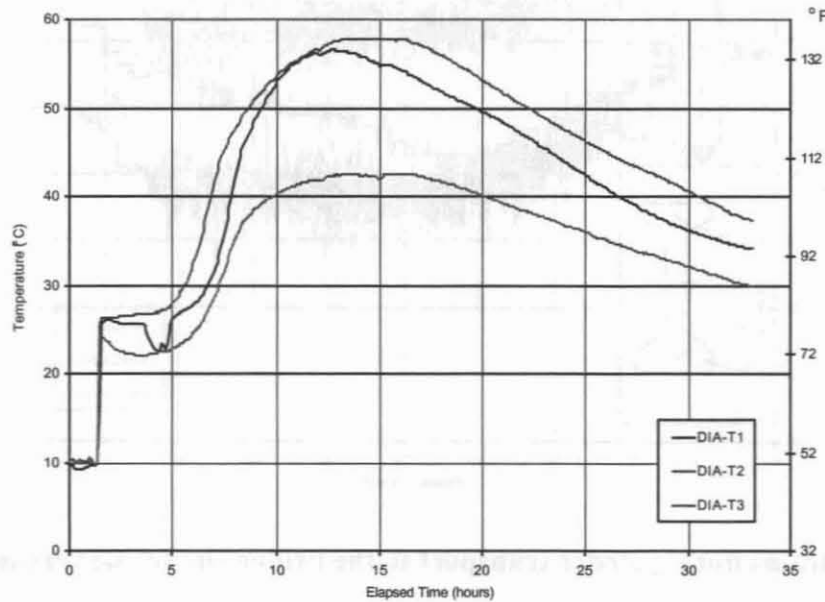


**Figure 6.16 Diaphragm temperatures during diaphragm and slab hydration**

The heat produced by hydration in the slab caused an increase in the temperature in the top flange of the girders. Figure 6.17 shows the temperatures in one of the girder cross-sections during the casting and curing of the diaphragm. The top flange temperatures were much higher than the web and bottom flange. A temperature gradient of 20 ° C (36° F) was exhibited at approximately 11 hours elapsed time.

### 6.4.3 Strains During Diaphragm and Slab Casting/Curing

Figure 6.18 shows vibrating wire strain gage measurements for cross-section LXM. The graph shows data that has not been corrected for temperature effects. While this may not have as much effect on the gages in the web and bottom flange, where the temperatures are more constant, the top flange gages experience a large temperature change.

The increase in curvature due to the large increase in dead load is in Figure 6.18. The shape of the LXM cross-section strain trends is very similar to that observed for cross-section SXM. The magnitude of the SXM strains are smaller, however, as would be expected of a

shorter span. The end cross-section of the short girder (SXE) exhibited strain magnitudes similar to the mid-span cross-section (SXM), Eatherton, 1999.

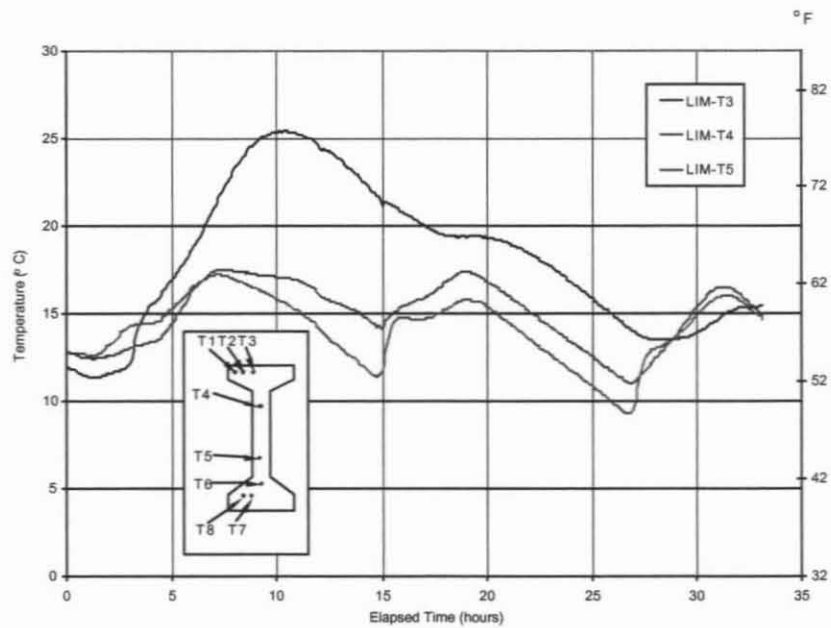


**Figure 6.17 Girder temperatures (LXM) during diaphragm and slab hydration**

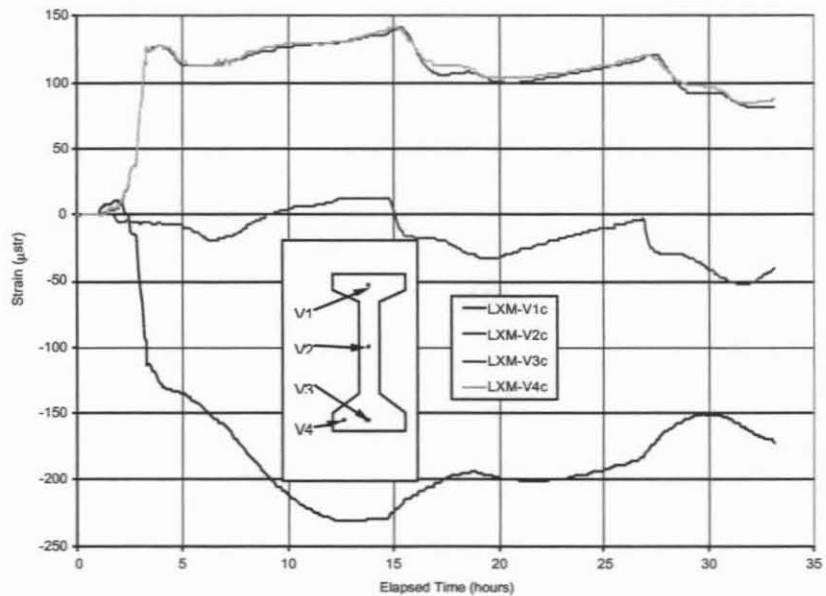


**Figure 6.18 Strains in girder cross-section LXM during the curing of the diaphragm and slab**

1. The first part of the report is a general introduction to the project. This includes the objectives, the scope of the work, and the organization of the report.



2. The second part of the report is a detailed description of the system. This includes the components, the data flow, and the control logic.



3. The third part of the report is a conclusion and a list of references. This includes a summary of the findings and a list of the sources used in the report.

*This unnumbered page is intentionally left blank*

## **7. LOAD TESTING AND SERVICE PERFORMANCE**

### **7.1 Load Test**

#### **7.1.1 Introduction**

A load test was performed on the bridge to examine the elastic response and understand its “as-built” performance. The load test was performed on December 12, 1998. Several loading configurations were implemented, however only some essential and typical results are described here.

#### **7.1.2 Equipment Used To Carry Out Load Test**

The load truck is part of the University of Missouri-Columbia Field Testing System developed in another project to study load rating of bridges (Barker, 1998). The truck is a 1984 Freightliner block and brick truck, previously used to deliver masonry products. It closely resembles an AASHTO H-20 loading vehicle as far as reproducing an equivalent moment envelope is concerned.

The distance between the front axle and the first back axle is 18' 3". The two back axles are 4' 3" apart. The lateral spacing between the wheels varies from front to back. The front wheel spacing is approximately 6', and the back wheel spacing is approximately 7'. Four Intercomp PT300 portable scales were used to determine the individual wheel loads. These scales measure loads up to 20,000 lbs in 20 lb increments.

The same truck loads were used for all loading configurations. The axle weights were found to be 10,400 lbs for the front axle, 15,480 lbs for the first back axle, and 15,900 lbs for the second back axle. This loading represents a total truck load of 41,780 lbs.

#### **7.1.3 Loading Schemes**

Several loading schemes were carried out. Positions were marked on the bridge for 5 traverses along the bridge and 22 locations along the length of each traverse. Some of the markings on the bridge can be seen in Figure 7.1. The traverses were positioned so that the outside wheel line would be exactly over a girder line, except for the center girder line for which the truck straddled the centerline of the bridge. A slow load test was carried out on the traverse that positioned the outside wheel loads on the instrumented exterior girders. Crawl speed load tests were carried out on all traverses. Times were recorded when the truck was over each

position so that the measured strains could be correlated to truck position. A picture of the load test in progress is shown in Figure 7.2.



**Figure 7.1** Load truck and markings on the bridge for the load test

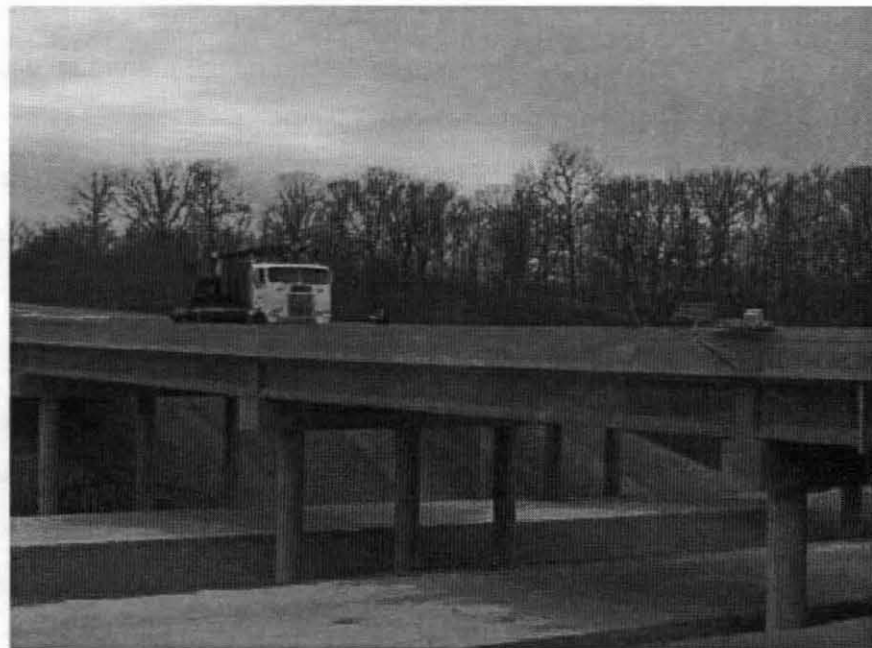


**Figure 7.2** Load test in progress

#### 7.1.4 Expected Strains During Load Test

It was found that the strains induced in the instrumentation during the load test were relatively small with respect to the accuracy with which strain is measured. For this reason the results from every loading scheme are not shown here. The slow load test for which the outer wheel line was directly over the exterior instrumented girders that produced the maximum strain output is examined in this section.

An analysis was performed to determine the expected strains in each gage position. Maximum and minimum moment envelopes were determined for every location along the bridge using structural analysis software. The maximum and minimum moments in the instrumented cross-sections were examined. Appropriate assumptions about the load distribution and effective flange width of the composite section were made. A modulus of elasticity of  $7.25 \times 10^6$  psi, which was determined from the 56-day compression tests, was used. The maximum and minimum calculated strains for each gage location and cross-section for which graphs of load test results will be given, are shown in Table 7.1.

**Table 7.1 Analytically predicted strains based on the load truck used**

Location *		LXM	LIM	SIE	SXM
Location 1	Max	3.1 $\mu$ str	1.2 $\mu$ str	3.7 $\mu$ str	5.2 $\mu$ str
	Min	-14.9	-5.8	-1.0	-11.0
Location 2	Max	11.5	4.5	0.8	8.5
	Min	-2.4	-0.9	-2.9	-4.0
Location 3	Max	40.2	15.7	2.7	29.7
	Min	-8.5	-3.3	-10.0	-14.1

\* Midspan strain gage measurement locations along depth: 1, 2 and 3 are at 50", 27" and 2" from the bottom of the girder, respectively

#### 7.1.5 Results from the Load Test

In general the response of each cross-section to the applied load exhibited a response in the shape that would be expected. Figure 7.3 shows a graph of strains during the load test. During this load test the load truck was positioned for five minutes on each marked location. If the elapsed time is correlated to the location of the load truck on the bridge, this graph becomes an influence line diagram for the strain in a cross-section. The inset in the bottom of the figure makes this correlation between time and the physical position of the truck on the bridge. Since Figure 7.3 shows the strains in the mid-span cross-section of the long, exterior girder, it is

expected that the instrumentation would exhibit negative curvature when the truck is over an adjacent span and positive curvature when the truck is over the span in question.

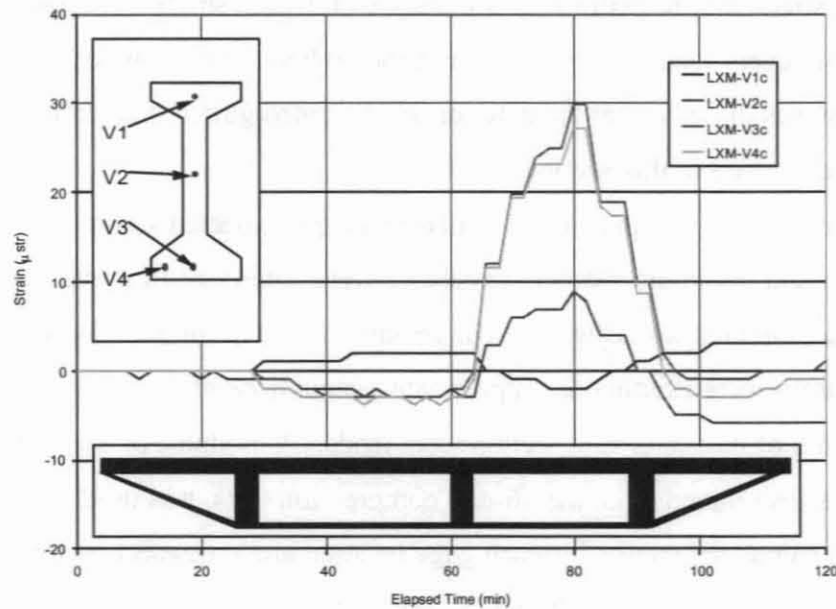


**Figure 7.3** Strains from the load test in cross-section LXM measured by vibrating gages

It must be noted that Figure 7.3 shows the response of vibrating wire strain gages that have not been corrected for temperature. The temperatures during this 2 hour period were monitored and found to generally stay relatively constant. According to the manufacturer, a  $1^{\circ}\text{C}$  change in temperature could cause a  $12\ \mu\text{str}$  change in the strain reading.

Keeping the temperature correction difficulty in mind, the strain in the bottom flange of cross-section LXM exhibits extreme values of  $+30\ \mu\text{str}$  and  $-5\ \mu\text{str}$ . These values represent approximately  $\frac{3}{4}$  of the strains predicted by analysis. The influence of the barrier curb which would make the bridge stiffer than the analysis predicts, could not be readily included in the theoretical strain predictions (Table 7.1).

Figure 7.4 shows the strain in cross-section LIM. The strain-gaged bars measured the strains shown. Again the general trend of curvature agrees with what would be expected. The theoretical predicted strain in location 3 was  $15.7\ \mu\text{str}$ , whereas the measured strain peaks at  $40\ \mu\text{str}$ . It should be noted that the bridge was open to traffic while these measurements were made. Hence, additional transient loads will have affected the static measurements from the load test.

This and the fact that strain-gage-based systems are prone to noise make exact comparisons with theory difficult, particularly when small strain values are registered.

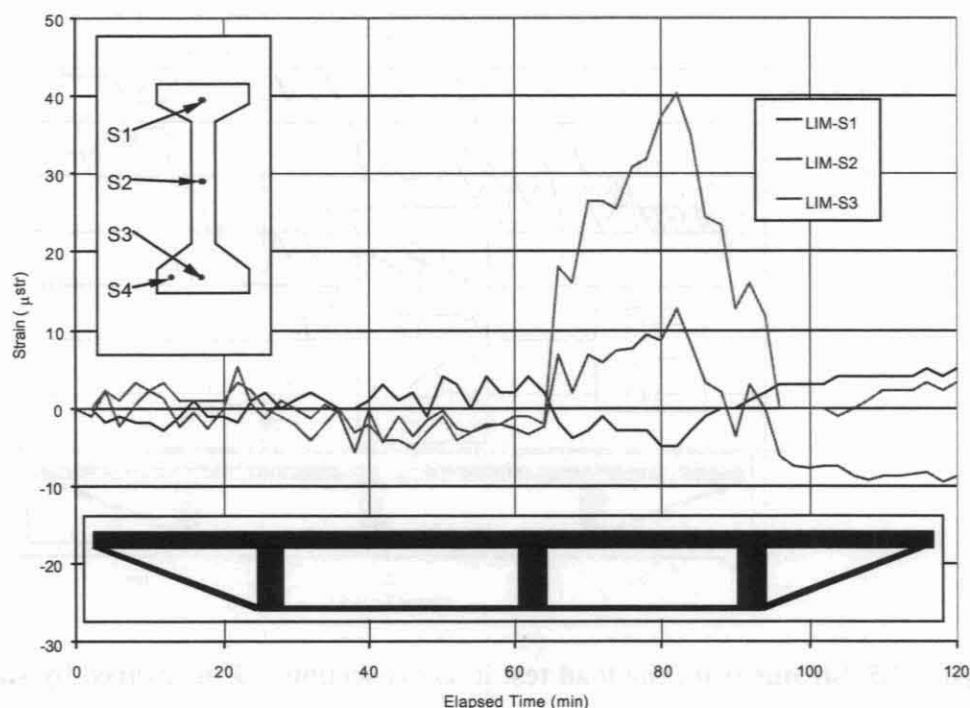


**Figure 7.4** Strains from the load test in cross-section LIM measured by strain-gaged bars

Figure 7.5 shows the strains in cross-section SIE during the load test. The noise is more pronounced in this section where the strains do not exceed  $8 \mu\text{str}$  in either direction. The trends in the curvature are still observed to be consistent as a large negative curvature is induced when the truck is in the adjacent span. In some instances one of the gages responded erratically as observed in Figure 7.6, where gage SXM-V1c seems to drift into tensile strain values (attributed to gage malfunction).

This load-test while limited in scope offers useful insights into the nature of the “as-built” response and the “in-service” performance of the instrumentation, particularly in relation to the service temperature response discussed in the next section.

## 7.2 Service Performance

### 7.2.1 Introduction

The bridge was put in service around November 1, 1998. Strain and temperature measurements were recorded at four-hour intervals while the bridge was in service (for almost

one year). These measurements not only indicate long-term trends in strain gradients, but also shed light on the daily variations in temperature and strain.

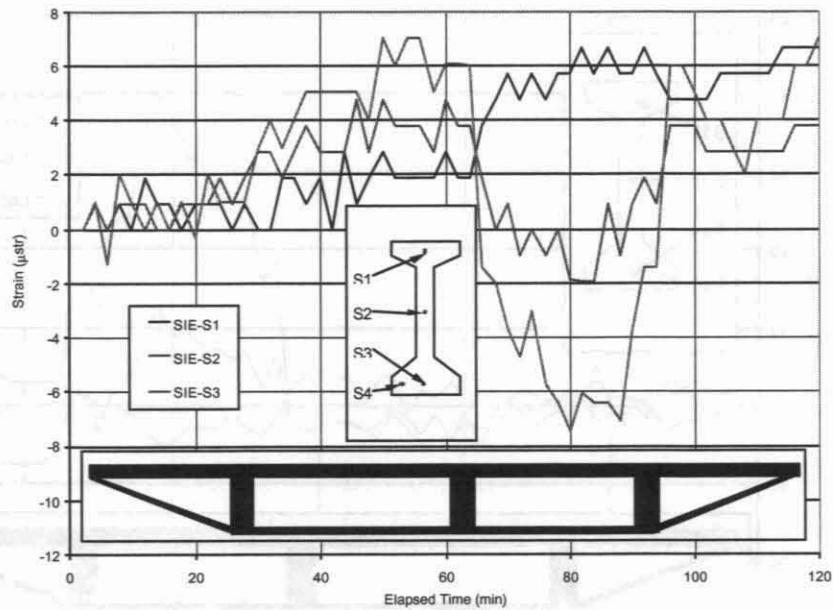


**Figure 7.5** Strains from the load test in cross-section SIE measured by strain-gaged bars

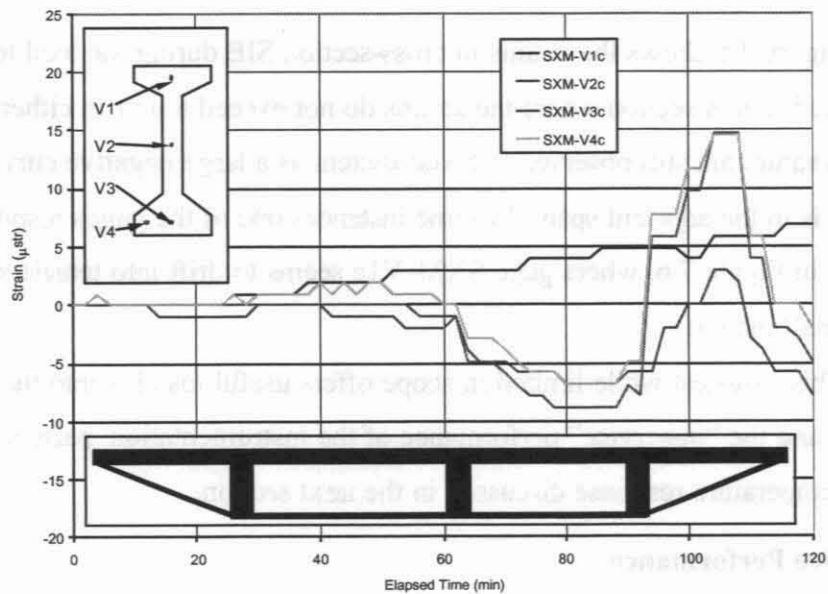


**Figure 7.6** Strains from the load test in cross-section SXM measured by vibrating gages

A three-day period was selected for examination to determine the effects of temperature variation on the strains in the girder cross-sections. This period started on March 17, 1998 at midnight and ended on the night of March 19, 1998. This time period was selected because it had reliable cyclic temperature change data.

### 7.2.2 Daily Temperature Variation

Figure 7.7 shows the temperatures in cross-section LIM. It was observed that the top flange temperatures peaked later, and with less magnitude, than the temperatures in the rest of the girder. The effect of the large mass of concrete, which is the slab, may act as a heat sink to reduce and delay the heat gained and lost by the girder. The overall magnitude of temperature change was approximately 15° C (27° F).

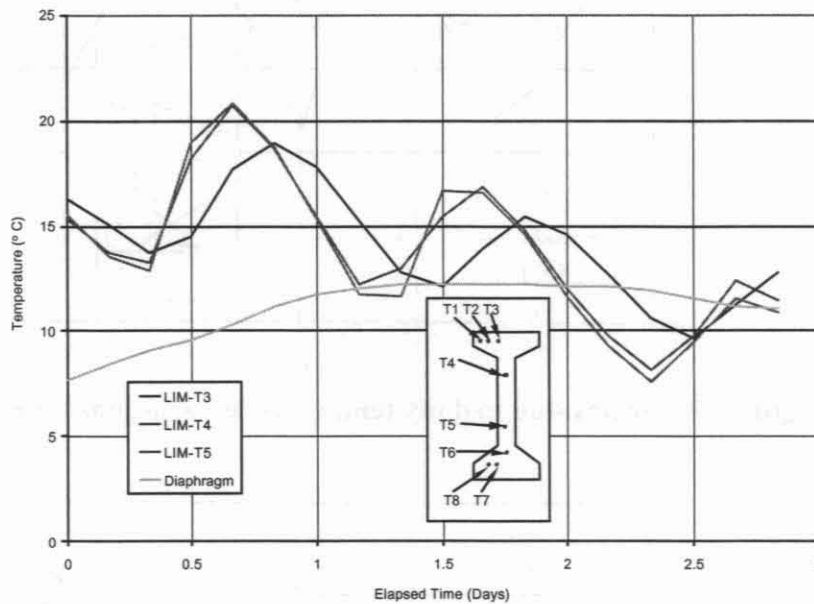


**Figure 7.7 Daily temperature variations in the girder and the diaphragm**

The temperature of gage DIA-T2 is shown as the diaphragm temperature. The lower temperature at the start is a result of lower temperatures prior to the period under examination. Note that the diaphragm does not experience variations in daily temperatures as can be observed for the girders. The massiveness of the diaphragm and the fact that it serves as a thermal drain (conductive heat transfer path to the ground) results in diaphragm temperature response that represents average trends in girder temperature variation with some time lag.

### 7.2.3 Daily Strain Variation

As a result of these temperature changes and temperature gradients, strains are induced in the girders. Figures 7.8 through 7.11 show the strains due to these temperature variations in cross-sections LIE, LXM, SIE, and SIM respectively. The trend of whether the strain at a location increased or decreased with increasing temperatures varied due to the complex system that the girder, slab and diaphragm represent. Strain gradients are also formed because of the temperature gradients.

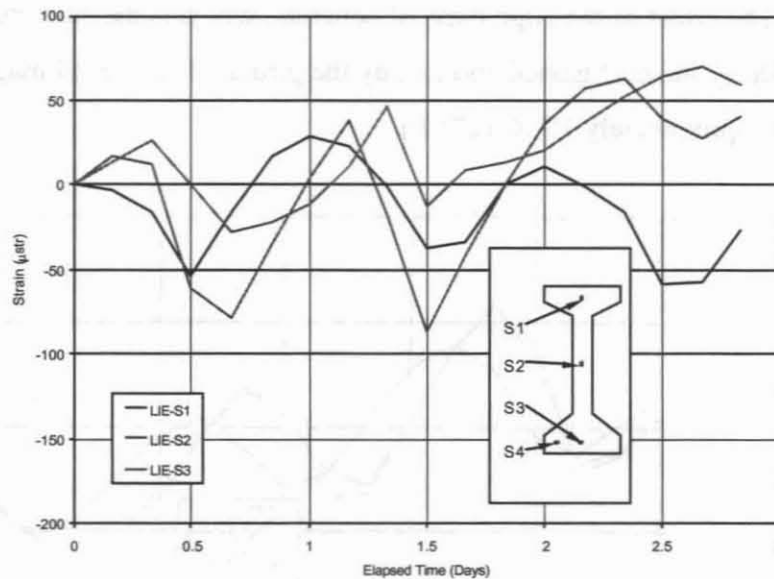


Figure 7.8 Strains due to daily temperature variations (cross-section LIE)

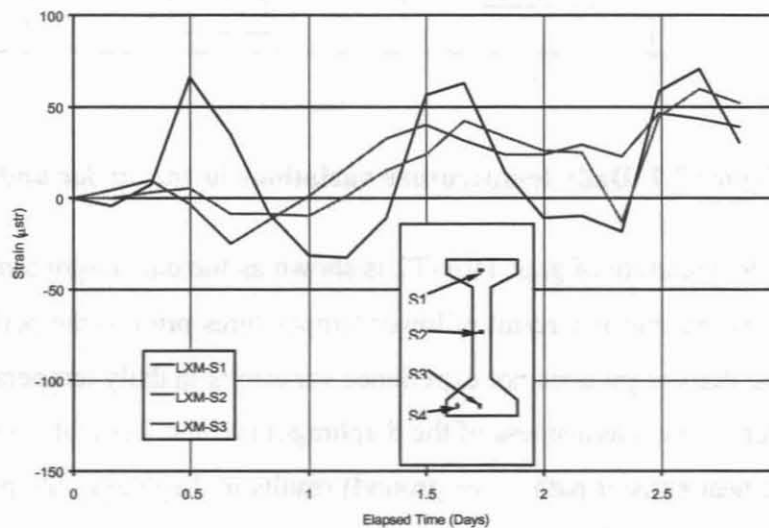
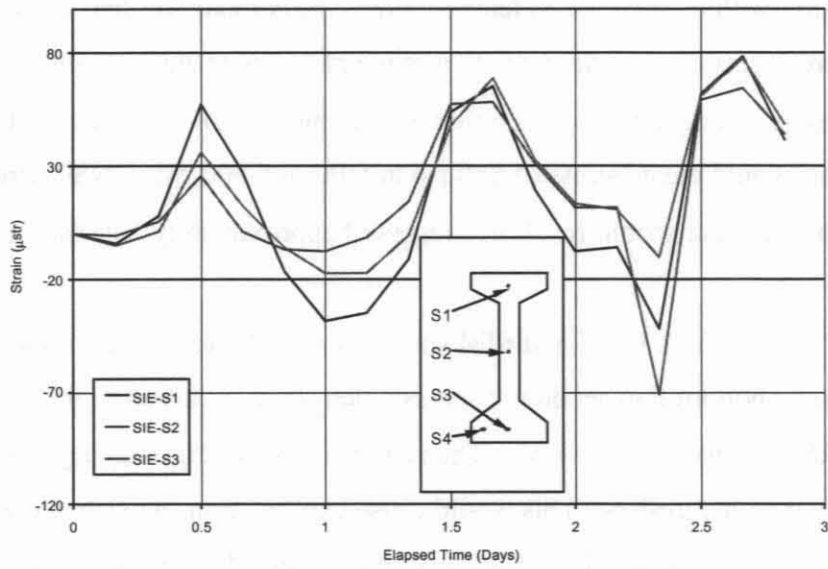
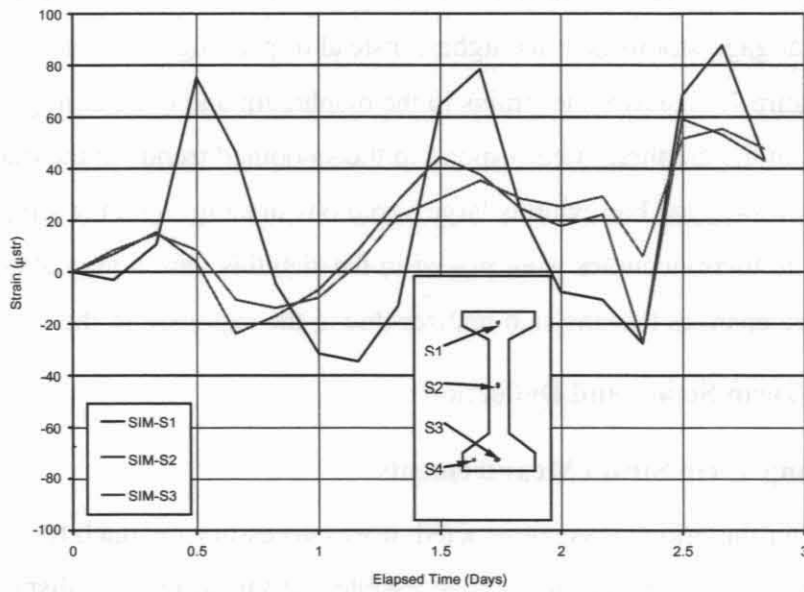


Figure 7.9 Strains due to daily temperature variations (cross-section LXM)



**Figure 7.10** Strains due to daily temperature variations (cross-section SIE)



**Figure 7.11** Strains due to daily temperature variations (cross-section SIM)

For cross-section LIE it is the trend for the whole girder cross-section to go into compression with an increase in temperature. The comparison that must be emphasized here is that for cross-section LIE strains with a range of 150  $\mu$ str were exhibited for a 15° C change, while a range of only 25  $\mu$ str was exhibited during a 41,780 lb truck load test. A strain excursion of 150  $\mu$ str would create stress of 850 psi in HPC and 600 psi in NSC girders. Similarly, excursion of 25  $\mu$ str would result in stresses of approximately 130 psi for HPC and 90 psi for NSC.

Cross-sections LXM and SIM show very similar responses to the temperature variations. The web and bottom flanges do not see as much strain variation as the top flange. The slab is exposed directly to the sun's rays. The slab is likely undergoing larger temperature changes on its surface than the girders. This would cause expansion in the slab and as a result negative curvature would be induced in the middle of the spans during the heat of the day. This is shown clearly in the LXM and SIM cross-sections. The SIE cross-section shows less curvature.

Figure 7.12 shows the response of the stirrups during the three-day period. A range of over 60  $\mu$ str variation was noted for some gages during the 15° C temperature changes. It is interesting to note that the peaks in the stirrup strains occurs when the rate of change of the longitudinal gage strains is at its highest instead of peaking when the longitudinal strains peak.

Figure 7.13 shows the strains in the diaphragm and deck during the same period. While the strains in the diaphragm correspond to the smoothed trends in the diaphragm temperatures, the deck strain-gaged bar exhibits large variations in strain with the temperature change. Although no thermocouples were placed in the slab this variation is likely due to large temperature changes that the slab realizes due to the exposure to the sun's rays.

### **7.3 Long Term Strain and Deflection**

#### **7.3.1 Long Term Strain Measurements**

After the bridge was constructed, it was necessary to attach the data acquisition system to the bridge in some way that made it accessible, yet safe from vandalism. The data acquisition box was attached to the diaphragm over Bent 2 with concrete anchor bolts. The terminal boxes were attached to the girders by hanging steel plates over exposed stirrups before the deck was cast. No anchor bolts were placed in the girder. The wires from the instrumentation to the

terminal boxes and the cables from the terminal boxes to the main box were protected with corrugated PVC tubing.

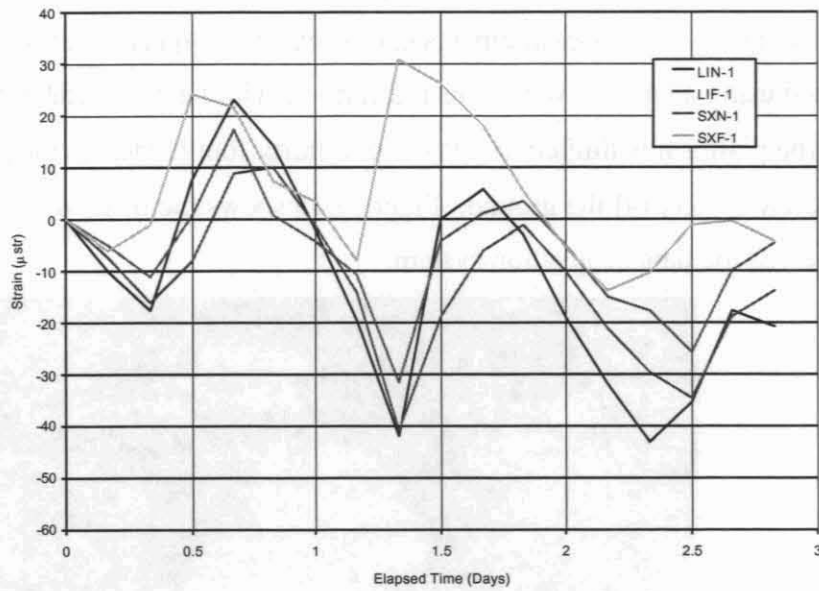


**Figure 7.12** Stirrup strains due to daily temperature variations (cross-section SIM)

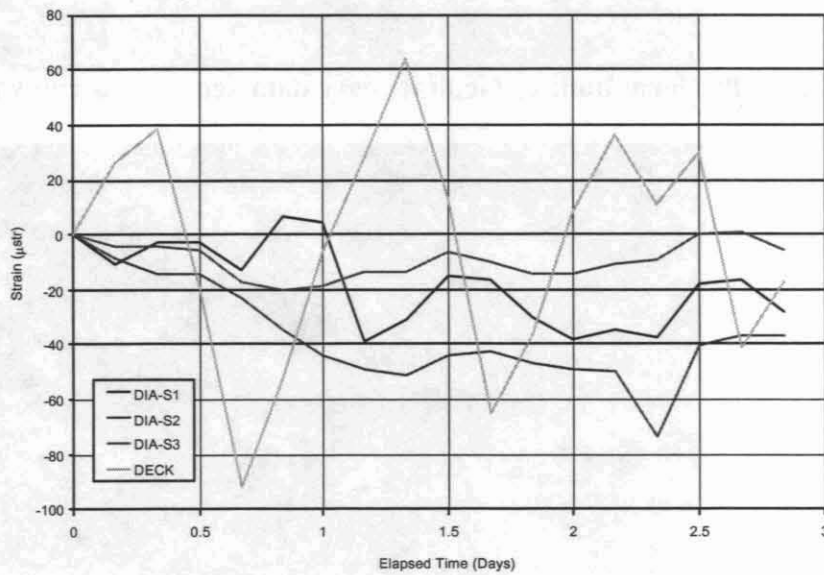


**Figure 7.13** Diaphragm strains due to daily temperature variations

A platform was built which rests on the bottom flanges of girders SI and SX. This platform is not attached to the girders in any way. The platform provides a staging area from which repairs, downloading data, uploading programs, and rewiring may be done. The platform is shown in Figure 7.14. Measurements can be examined quasi-real time and data can be downloaded using a laptop. While this platform provides a comfortable work environment, access to the platform is limited to owners of a thirty-foot ladder, as the platform sits approximately 25 feet off the ground. Figure 7.15 shows the method by which the MU Research Team accessed the data acquisition system.

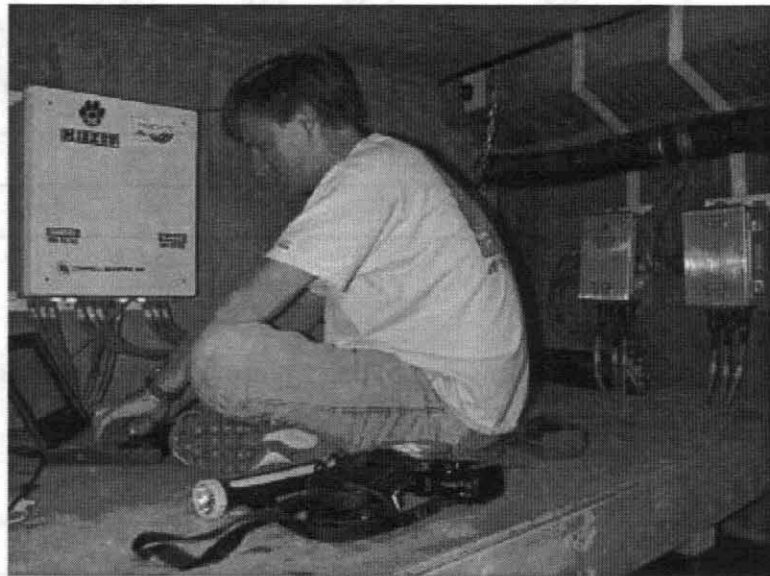


**Figure 7.14** Platform built to facilitate easy data acquisition and wiring reconfigurations

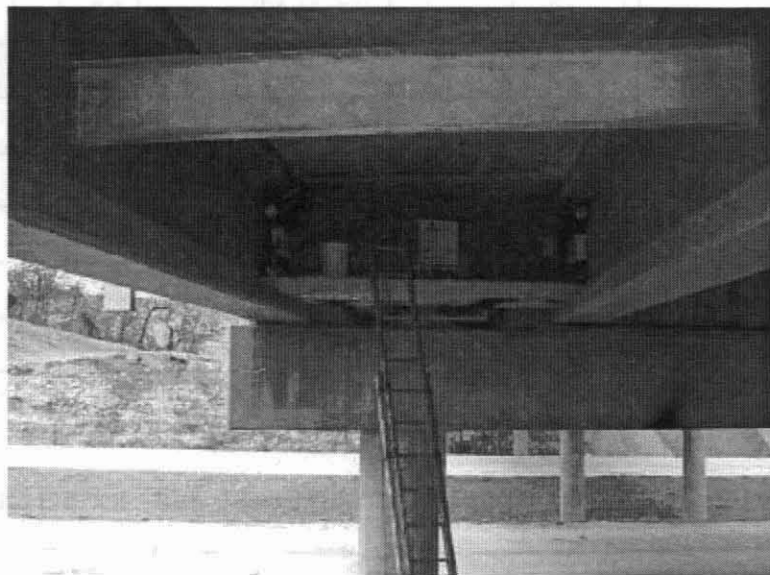


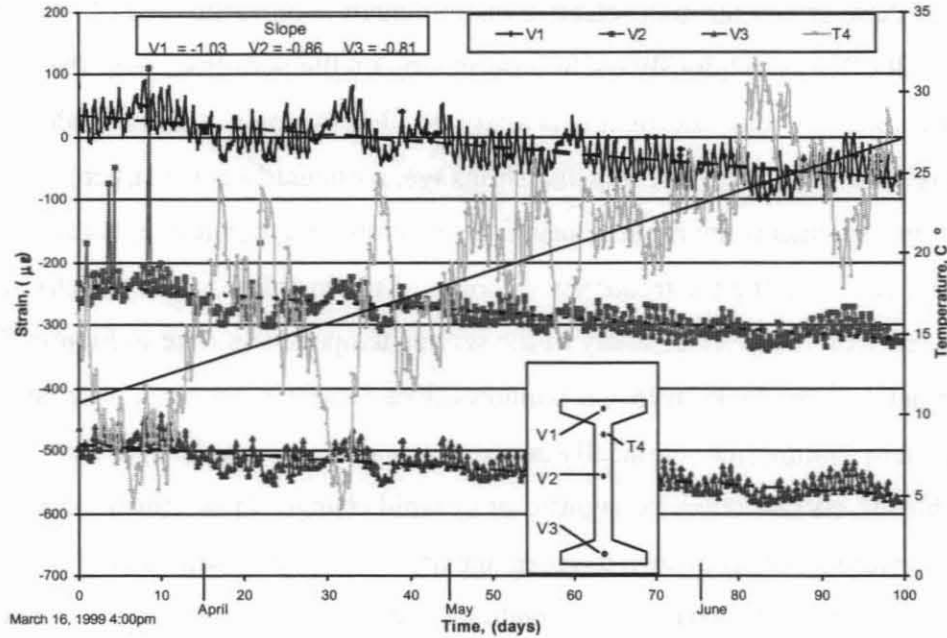
**Figure 7.15** Access to the work platform using a 30-ft ladder

It should be noted that all of the strain measurements reported after the bridge was placed in service include the combined effects of vehicular traffic, restrained creep and shrinkage as well as the effect of service temperature variations. It is difficult if not impossible to isolate one or more of these effects through selective instrumentation or traffic control. However, service data can still offer tremendously useful information on the performance of the as-built structure depending upon how this information is analyzed. For example, a short window of 2-3 days can essentially filter out effects of creep and shrinkage, particularly if the structure is sufficiently old when the measurements are made. During this window, if dynamic events due to vehicular traffic can be filtered out (using the frequency response of the instrumentation judiciously), what one is typically left with is the effect solely of the service temperatures (like in Figures 7.7 – 7.13). On the other hand, if one looks at longer windows (like 3 months), one can observe trendlines of strain and temperature (monotonically increasing or decreasing values) to isolate largely irreversible effects (assuming no significant or rapid changes in sustained loads or humidity during this window of time) such as creep and shrinkage can be separated from the influence of service temperature. This type of observation is demonstrated in Figures 7.16 and 7.17 (Barrett, 2000).

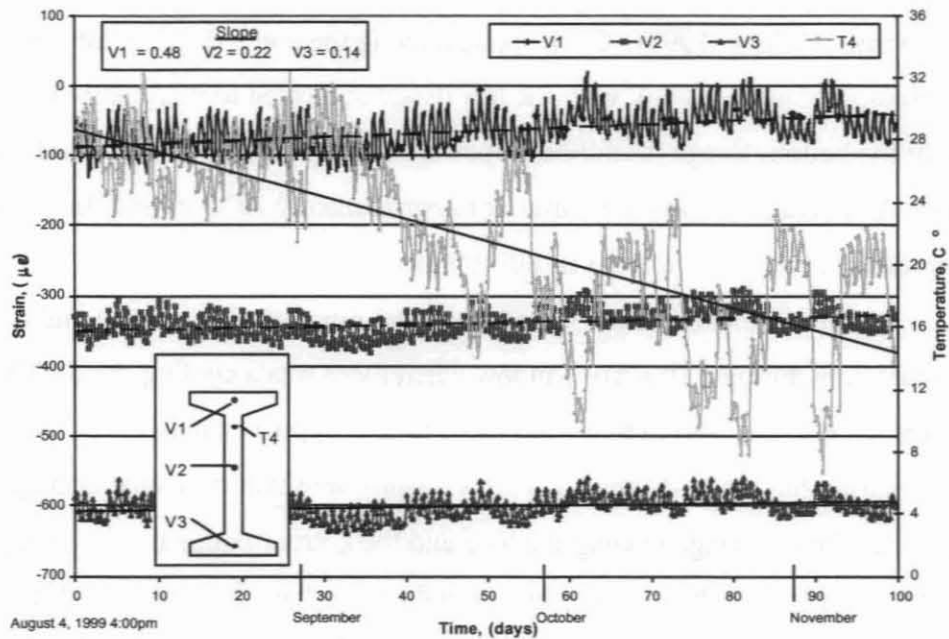
Figure 7.16 shows data from vibrating wire strain gages (V1, V2, V3) and a thermocouple (T4) in the cross-section SIE over a 100-day period when there is a warming trend (March through June, 1999). Girder strains along the entire depth exhibit increased compression (increasing negative strains), with the top flange subjected to marginally higher change than the web or the bottom flange (trendline slopes of  $-1.03$  versus  $-0.86$  and  $-0.81$ , respectively – see inset). An average rise in temperature of approximately  $15^{\circ}\text{C}$  during this period produces compressive strains of the order of 80-100  $\mu\text{str}$ .

Figure 7.17 shows the response from the same instrumentation and cross-section shown in Figure 7.16 during a 100-day window when there was a cooling trend. The drop in the average temperature during this window of time is approximately  $13^{\circ}\text{C}$ . All gages exhibit tensile strains during this time (decreasing compression), however of a smaller magnitude (15-50  $\mu\text{str}$ ), again with the top flange leading the web and the bottom flange in this change. The smaller effect of temperature during a cooling period can perhaps be explained due to the camber that exists in the bridge prior to service. When the girders lengthen due to increasing temperatures, the camber adds to the effect of restraints (additive effect) at the diaphragm causing larger

compressive strains on the girder. When the girders shorten due to decreasing temperatures, the camber relaxes some of the effect of the restraint (subtractive effect), resulting in smaller magnitudes of strain. Similar trends were observed in the other instrumented cross-sections.



**Figure 7.16** Strains due to service temperatures during a period of increasing temperature in cross-section SIE



**Figure 7.17** Strains due to service temperatures during a period of decreasing temperature in cross-section SIE

It is important to observe here that the maximum magnitude of strains in the girders caused either due to daily or seasonal variations of temperature is significantly larger than that caused due to the loaded truck used (approximately producing moment envelopes comparable to the designed live loads).

### 7.3.2 Long-Term Deflection Measurements

The deflection of the instrumented girders has been monitored at times during their fabrication, storage, erection, and service life. Figure 7.18 and Figure 7.19 show the deflections of girders SX and LX respectively. These figures show only some of the deflection readings taken and are considered representative of the other two girders. The initial camber of the girders after transfer is shown along with the increasing camber as the girder is stored in the precast yard.

The values of the initial mid-span camber and the mid-span camber after approximately 40 days of storage are tabulated in Table 7.2. To examine methods by which time-dependant deflections are determined, a calculation of this deflection was done to compare to the measured deflections for each girder. The ACI method for determining time-dependant deflections was carried out using appropriate assumptions. For all girders this prediction of deflection was greater than the measured values. The predicted time-dependant deflections are shown in Table 7.2.

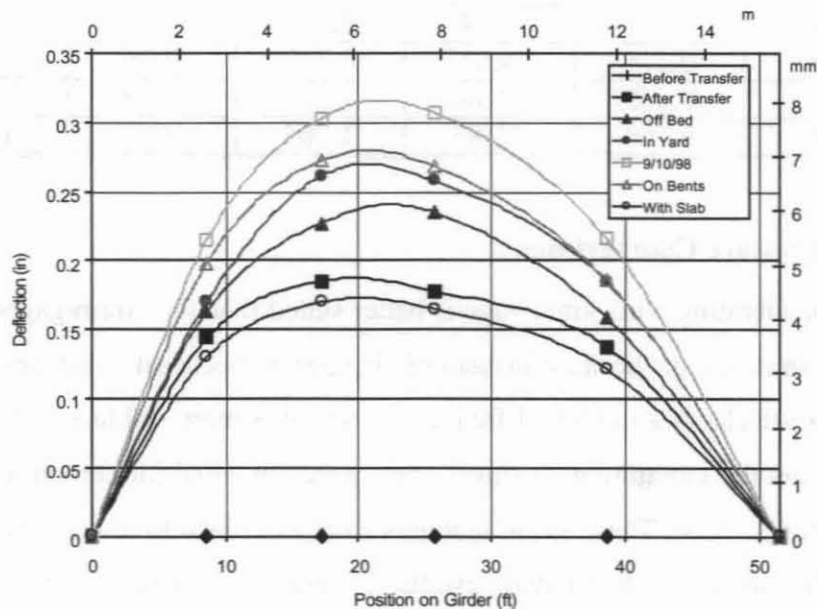
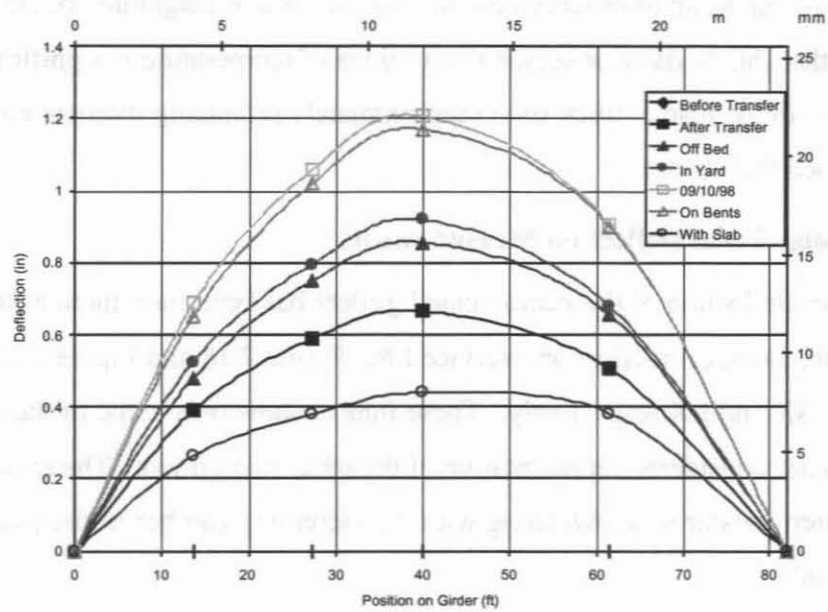


Figure 7.18 Deflections in girder SX at selected times during the girder life



**Figure 7.19** Deflections for girder LX at selected times during the girder life

**Table 7.2** Time-dependent deflections due to prestress force

Girder	Experimental Measurements				Analytical Prediction	
	After Transfer		September 10, 1998		ACI Code for 9/10/98	
	(in)	(mm)	(in)	(mm)	(in)	(mm)
SI	0.171	4.34	0.236	5.99	0.364	9.25
SX	0.178	4.52	0.307	7.80	0.379	9.63
LI	0.655	16.64	1.224	31.09	1.395	35.43
LX	0.664	16.87	1.205	30.61	1.414	35.92

### 7.3.3 Curvature Comparisons

The vibrating wire strain gage is better suited than the strain-gaged rebars to measure long-term strain events because instead of changes in electrical resistance, the vibrating wire gages measure changes in natural frequency (which is more stable and noise-free). The strain readings from the vibrating wire strain gages were compiled for certain times in the life of the instrumented girders. These strain readings were examined to understand the accumulation of strain in the girders due to all strain events. Figures 7.20 through 7.21 show the strain gradients at selected times for cross-sections LIE, LXM, SIM, and SXE. These figures do not show all of

the times for which the strain gradient was examined in this way, but instead shows a representative look at the data examined. These figures use the manufacturer's temperature correction for the vibrating wire strain gage.

Figure 7.21 clearly shows the increase in curvature after transfer, when only the time dependant effects are acting on cross-section LXM. After casting the slab a large decrease in curvature is noted. Figure 7.20 shows that neither the time-dependant effects during storage nor the slab dead load cause as large a change in curvature in cross-section LIE as the mid-span cross-section. In the long girders maximum compressive strains of  $950 \mu\text{str}$  were exhibited and no tensile strains were recorded.

The short girder cross-sections shown in Figure 7.22 and 7.23 show that the magnitudes of strain in the short girders peaked just over  $800 \mu\text{str}$  of compression. The trend in the long girders that the mid-span cross-section exhibits larger time-dependant change in curvature and more curvature as a result of the slab dead load is noted for the short girders.

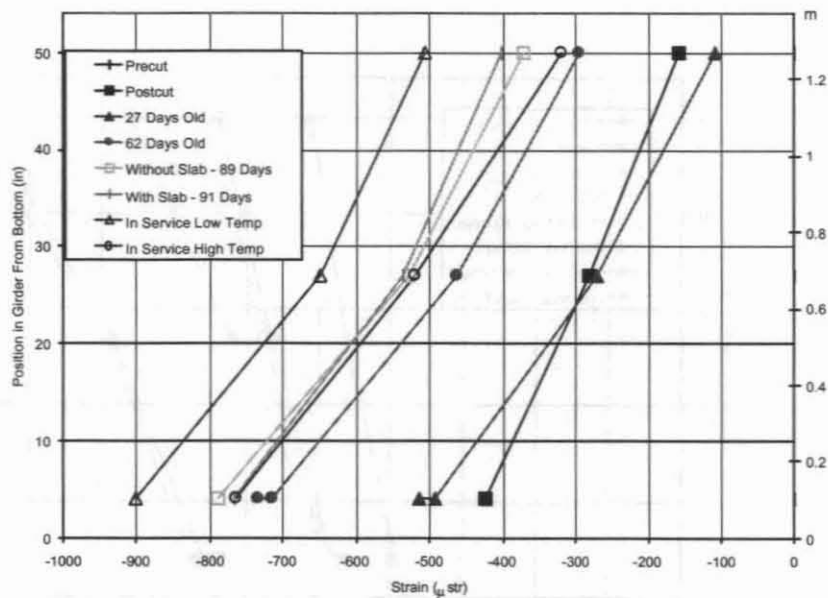


**Figure 7.20 Measured strain gradients at selected times for cross-section LIE**

Curvature values were computed from the strain gradients and from the deflection measurements. These curvature values are compared in Tables 7.3 through 7.6. To obtain the curvature from the deflection measurements a quadratic trendline was fit to the deflected shape.

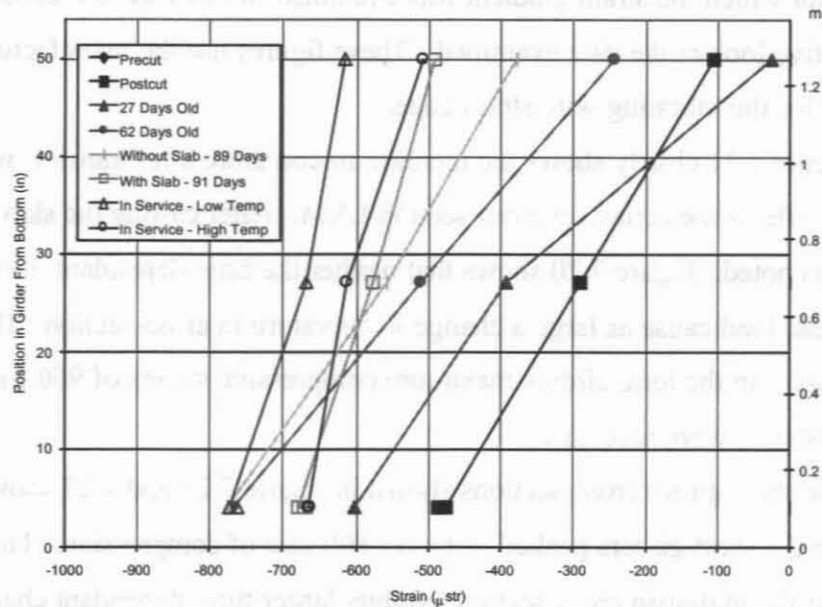


**Figure 7.21 Measured strain gradients at selected times for cross-section LXM**

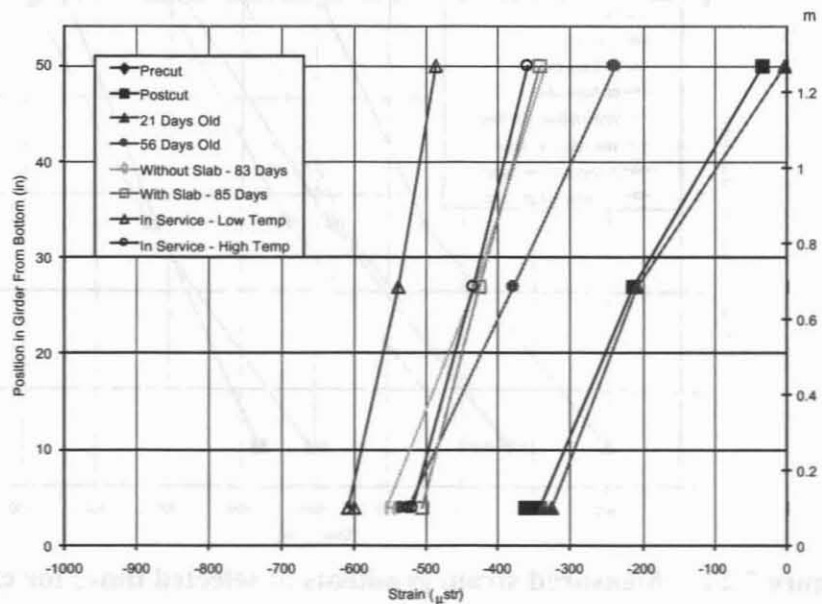


**Figure 7.22 Measured strain gradients at selected times for cross-section SIM**

The second derivative of this deflected shape equation gives a constant curvature. From beam theory, the deflected shape of the girder could better be approximated by a fourth order function so that the curvature would retain a quadratic form as expected. It has been observed that a quadratic trend for the deflected shape achieves high  $R^2$  values and makes the computation of

curvature easier. The curvature computed from the deflection measurements will not be accurate with dead load, and especially after the diaphragm is cast and continuity is provided. It can be seen in Tables 7.3 through 7.6 that the curvature values after the slab is cast, and the dead load increased, the curvature at the end cross-sections remains steady while the mid-span cross-sections exhibit the reduction in curvature with which the deflection measurement agrees. In general the curvature values computed from the deflection measurements agree with the curvature values computed from strain gradient measurements.

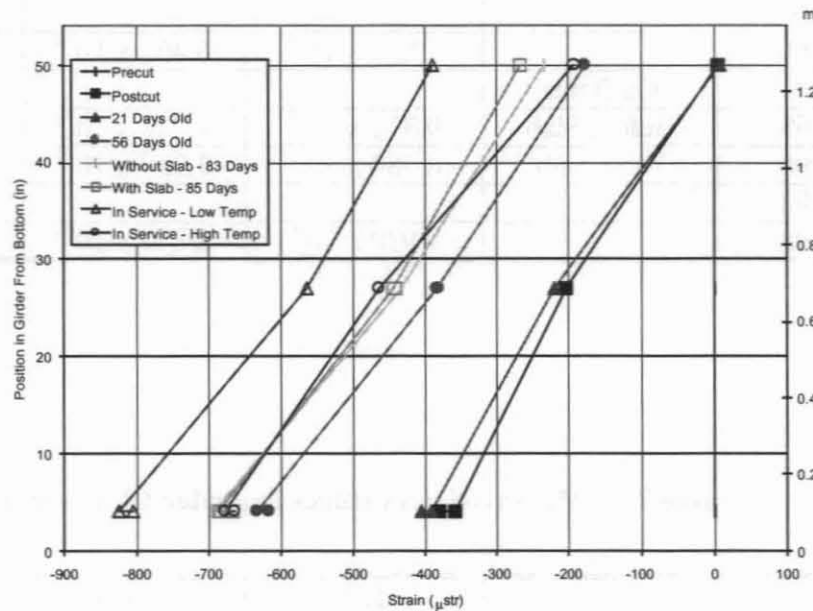


Figure 7.23 Measured strain gradients at selected times for cross-section SXE

Table 7.3 Measured curvatures in girder SI at selected times

Date	Description	SIE Curvature (1/in)	SIM Curvature (1/in)	Curvature From Deflection for Girder SI (1/in)
8/3/98	After Transfer	$8.157 \times 10^{-6}$	$6.868 \times 10^{-6}$	$3.578 \times 10^{-6}$
8/7/98	At the Yard			$3.724 \times 10^{-6}$
8/20/98				$4.306 \times 10^{-6}$
8/21/98		$8.826 \times 10^{-6}$	$7.337 \times 10^{-6}$	
8/26/98		$9.276 \times 10^{-6}$	$6.094 \times 10^{-6}$	
9/10/98				$4.964 \times 10^{-6}$
9/25/98		$9.843 \times 10^{-6}$	$6.337 \times 10^{-6}$	
10/22/98	Before Slab	$9.891 \times 10^{-6}$	$5.420 \times 10^{-6}$	
10/24/98	After Slab	$9.074 \times 10^{-6}$	$4.052 \times 10^{-6}$	
12/13/98		$10.000 \times 10^{-6}$	$3.373 \times 10^{-6}$	

**Table 7.4 Measured curvatures in girder SX at selected times**

Date	Description	SXE Curvature (1/in)	SXM Curvature (1/in)	Curvature From Deflection for Girder SX (1/in)
8/3/98	After Transfer	$7.752 \times 10^{-6}$	$6.916 \times 10^{-6}$	$4.225 \times 10^{-6}$
8/7/98	At the Yard			$5.804 \times 10^{-6}$
8/20/98				$6.783 \times 10^{-6}$
8/21/98		$8.217 \times 10^{-6}$	$7.087 \times 10^{-6}$	
8/26/98		$8.104 \times 10^{-6}$	$5.963 \times 10^{-6}$	
9/10/98				$6.904 \times 10^{-6}$
9/25/98		$10.00 \times 10^{-6}$	$6.402 \times 10^{-6}$	
10/8/98	On Bents			$6.213 \times 10^{-6}$
10/22/98	Before Slab	$9.311 \times 10^{-6}$	$4.744 \times 10^{-6}$	
10/24/98	After Slab	$8.584 \times 10^{-6}$	$3.559 \times 10^{-6}$	
10/30/98				$3.869 \times 10^{-6}$
12/13/98		$9.930 \times 10^{-6}$	$2.833 \times 10^{-6}$	

**Table 7.5 Measured curvatures in girder LI at selected times**

Date	Description	LIE Curvature (1/in)	LIM Curvature (1/in)	Curvature From Deflection for Girder LI (1/in)
7/27/98	After Transfer			$5.531 \times 10^{-6}$
7/28/98		$5.848 \times 10^{-6}$	$7.987 \times 10^{-6}$	$10.13 \times 10^{-6}$
7/29/98	Off Bed			$7.049 \times 10^{-6}$
7/31/98	At the Yard			$7.542 \times 10^{-6}$
8/7/98				$8.669 \times 10^{-6}$
8/20/98				$9.311 \times 10^{-6}$
8/21/98		$8.811 \times 10^{-6}$	$10.07 \times 10^{-6}$	
8/26/98		$8.396 \times 10^{-6}$	$10.46 \times 10^{-6}$	
9/10/98				$9.953 \times 10^{-6}$
9/25/98		$9.634 \times 10^{-6}$	$12.11 \times 10^{-6}$	
10/8/98	On Bents			$9.624 \times 10^{-6}$
10/22/98	Before Slab	$9.225 \times 10^{-6}$	$9.285 \times 10^{-6}$	
10/24/98	After Slab	$8.104 \times 10^{-6}$	$3.526 \times 10^{-6}$	
10/30/98				$3.674 \times 10^{-6}$
12/13/98		$9.302 \times 10^{-6}$	$4.065 \times 10^{-6}$	

**Table 7.6 Measured curvatures in girder LX at selected times**

Date	Description	LXE Curvature (1/in)	LXM Curvature (1/in)	Curvature From Deflection for Girder LI (1/in)
7/27/98	After Transfer			$5.531 \times 10^{-6}$
7/28/98		$5.627 \times 10^{-6}$	$8.170 \times 10^{-6}$	$5.961 \times 10^{-6}$
7/29/98	Off Bed			$7.049 \times 10^{-6}$
7/31/98	At the Yard			$7.542 \times 10^{-6}$
8/7/98				$8.669 \times 10^{-6}$
8/20/98				$9.311 \times 10^{-6}$
8/21/98		$10.48 \times 10^{-6}$	$12.47 \times 10^{-6}$	
8/26/98		$8.651 \times 10^{-6}$	$10.58 \times 10^{-6}$	
9/10/98				$9.953 \times 10^{-6}$
9/25/98		$8.881 \times 10^{-6}$	$11.39 \times 10^{-6}$	
10/8/98	On Bents			$9.624 \times 10^{-6}$
10/22/98	Before Slab	$7.987 \times 10^{-6}$	$8.734 \times 10^{-6}$	
10/24/98	After Slab	$8.019 \times 10^{-6}$	$4.042 \times 10^{-6}$	
10/30/98				$3.674 \times 10^{-6}$
12/13/98		$8.532 \times 10^{-6}$	$3.639 \times 10^{-6}$	

*This unnumbered page is intentionally left blank*

## **8. CONCLUSIONS AND RECOMMENDATIONS**

### **8.1 Conclusions**

The instrumentation and monitoring project, which required some serious planning to ensure that all the important parameters required for the different stages in the life of the prestressed girders, were measured was successful and greatly benefited from discussions with researchers who had previously carried out similar projects. The self-contained system, powered by a solar panel had the capability of remotely uploading of data acquisition programs and downloading data to monitor the performance of the bridge. Better calibration of the response of vibrating wire gages, particularly for monitoring events that subject these transducers to a combination of transient mechanical and thermal loads is necessary so that strains measured using these gages can be used in such situations (longer-term early-age strain measurements where the thermal loading is significant). In hindsight, the power capacity of the solar panels could be increased to allow for uninterrupted supply to the data acquisition system and the numerous transducers, even during periods of several cloudy days.

While the infrared thermography provided useful data to corroborate data from the embedded thermocouples and thermistors, more direct point-to-point comparisons planned earlier could not be successfully accomplished.

Maximum differential temperatures in the girder cross-sections during curing were between 12-22°C (54-72°F) for the HPC girders. The differential heating results in differential rates of concrete setting (due to locally accelerated curing at higher temperatures) as well as residual stresses due to restraints provided by the steel molds. Numerical modeling of the cross-section conducted in a companion study (Earney, 2000), based on thermal data from this investigation resulted in maximum residual tensile stresses in the cross-section, which is more than half the tensile strength of concrete. Girder end stresses due to prestress transfer have been computed using the modified Gerlely-Sozen model to be approximately half the tensile strength. Hence, the girder end cracking observed in this study, can be attributed to a combination of these two causes. Improved curing procedures that allow more uniform temperature development and end zone design modifications that provide improved tensile performance or reduced stresses will minimize the potential for such girder cracking.

Unrestrained shrinkage strains in HPC cylinders were observed to be approximately 40% less than that measured for NSC under similar laboratory conditions. For HPC mix parameters used, it was observed that the magnitude of autogenous shrinkage (measured from sealed specimens) was comparable to drying shrinkage in magnitude, although the former was marginally more dominant (unlike for NSC). Total creep was 5-15% smaller for HPC compared to NSC, however the basic creep components were nearly equal. HPC exhibited high early creep (with 60 days), which soon stabilized with very small additional creep. The improved shrinkage and creep performance of HPC can be incorporated in design so as to allow more accurate prediction of prestress losses and time dependent deflections.

Maximum strains during transportation of the girders from the precasting yard to the bridge site and construction strains were of the order of  $\pm 40 \mu\text{str}$ . The influence line of strains from a load-test (using a total truck load of 41,780 lbs) produced predictable profiles, although the overall as-built response was approximately 30-40% stiffer compared to analytical predictions (which did not include stiffness contributions from barriers etc.). Maximum strains from daily and seasonal temperature variations were observed to be significant and 5-6 times than the maximum strains observed from the load-test. It would be prudent to review design procedures so that bridges of this type (continuous composite prestressed I-girder) could be explicitly designed for these levels of service thermal loading in addition to normal design loading.

## **8.2 Recommendations**

It is recommended that the curing procedures be improved so that more uniform heat development can be ensured during hydration. Reconfiguring the steam lines used for steam curing the girders can readily accomplish this. Incorporating steel fibers in the concrete mix, particularly at the girder ends (in addition to the lateral reinforcement already included) should result in improved tensile performance of the end zone. Another practical way to reduce stress in the end zone is through the use of end blocks as is done in some other states.

Design provisions dealing with prestress losses and prediction of long-term deflection can be revised to reflect the improved performance of HPC as far as shrinkage and creep is concerned. Further more detailed studies on a range of HPC mixes to be used by MoDOT characterizing their creep and shrinkage response is needed before this can be accomplished. It is not advisable to develop models based on the limited study on the one mix studied here.

From the results reported in this investigation, it is clear that the influence of daily and seasonal service temperature variations are significant in comparison to the influence of mechanical loading and should be explicitly considered while designing such bridges. This will be the case with NSC bridges as much as it is with HPC bridges.

*This unnumbered page is intentionally left blank*

## 10. REFERENCES

1. ACI Committee 209 "Prediction of Creep, Shrinkage and Temperature Effects In Concrete Structures" Report No. ACI 209R-92, 1992.
2. Adelman, D. Cousins, T. E. "Evaluation of the Use of High Strength Concrete Bridge Girders in Louisiana" PCI Journal, v 40, n 6, September-October 1990.
3. Ahlborn, T., French, C. E., and Leon R. T. "Applications of High-Strength Concrete to Long-Span Prestressed Bridge Girders" Transportation Research Record, n 1476, 1995.
4. Ahlborn, T. M., Shield, C. K., French, C. W. "Behavior of Two Long-Span High Strength Concrete Prestressed Bridge Girders" Worldwide Advances in Structural Concrete and Masonry Structures Congress – Proceedings, ASCE, New York, NY, 1996.
5. Barker, M. , "Steel Girder Bridge Field Test Procedures", Construction and Building Materials, Vol. 13, 1999, pp. 229-239.
6. Barrett, D.G. , "Long Term Temperature Effects on High Performance Concrete Bridge Girders", CE350 Honors Report, Advisor: Prof. Vellore S. Gopalaratnam, Department of Civil and Environmental Engineering, University of Missouri-Columbia, May 2000.
7. Bazant, S. P. and Wittmann, F. H. Creep and Shrinkage in Concrete Structures John Wiley and Sons Ltd., Chichester, 1982.
8. Branson, D. E. Deformation of Concrete Structures New York, McGraw-Hill, 1977.
9. Beacham, M. W. "HPC Bridge Deck in Nebraska" Concrete International, v 21, n 2, February 1999.
10. Chojnacki, T., "Determination of High Performance Concrete (HPC) Characteristics," Missouri Department of Transportation, Report RDT 99-008, September 1999.
11. Eatherton, M. A., "Instrumentation and Monitoring of HPC Prestressed Bridge Girders," M.S. Thesis, Advisor: Prof. Vellore S. Gopalaratnam, Department of Civil and Environmental Engineering, University of Missouri-Columbia, May 1999.
12. Earney, T. P., "Girder Cracking in Prestressed Concrete I-Girder Bridges," M.S. Thesis, Advisor: Prof. Vellore S. Gopalaratnam, Department of Civil and Environmental Engineering, University of Missouri-Columbia, August 2000.
13. Einea, Amin Huo, Xiaoming Saleh, Mohsen Tadros, M. K. "High Performance Concrete for Giles Road Bridge" Structures Congress
14. FHWA "Alabama – Alabama Highway 199 Over Uphaupee and Bulger Creek, Macon County" Publication Number FHWA-RD-97-055, 1997a.

15. FHWA "Georgia – Bridge Over Interstate 75, Henry County, Tentative Site" Publication FHWA-RD-97-057, 1997b.
16. FHWA "Nebraska – 120<sup>th</sup> Street and Giles Road Bridge, Sarpy County" Publication Number FHWA-RD-97-058, 1997c.
17. FHWA "New Hampshire – Route 104 Bridge Over the Newfound River, Bristol" Publication Number FHWA-RD-97-059, 1997d.
18. FHWA "New Hampshire – Route 3A Bridge Over the Newfound River, Bristol" Publication Number FHWA-RD-97-088, 1997e.
19. FHWA "North Carolina – U.S. 401 Over the Neuse River, Wake County" Publication Number FHWA-RD-97-060, 1997f.
20. FHWA "Texas – Louetta Road Overpass State Highway 249, Houston" Publication Number FHWA-RD-97-063, 1997g.
21. FHWA "Texas – San Angelo Bridge U. S. Route 67, San Angelo" Publication Number FHWA-RD-97-062, 1997h.
22. FHWA "Virginia – Route 40 Over the Falling River, Lynchburg District" Publication Number FHWA-RD-97-065, 1997i.
23. FHWA "Virginia – Virginia Avenue Over the Clinch River, Richlands" Publication Number FHWA-RD-97-064, 1997j.
24. FHWA "Washington – Eastbound State Route 18 Over State route 515, King County" Publication Number FHWA-RD-97-066, 1997k.
25. French, C., Mokhtarzadey, A., Ahlborn, T., Leon, R. "High-Strength Concrete Applications to Prestressed Bridge Girders" Construction and Building Materials, v 12, n 2-3, March-April 1998.
26. Gamble, W. L., Kannel, J., French, C. and Stolarski, H. "Release Methodology of Strands to Reduce End Cracking in Pretensioned Concrete Girders – Reader Comments" PCI Journal, July- August 1997, pp. 102-108
27. Geren, K. L., Abdel-Karim, A. M., Tadros, M. K. "Precast / Prestressed Concrete Bridge I-Girders: The Next Generation" Concrete International, v 14, n 6, June 1992.
28. Gergely, P. and Sozen, M. "Design of Anchorage-Zone Reinforcement in Prestressed Concrete Beams" PCI Journal, April 1967, pp. 63-75

29. Gilbert, R. I. *Time Effects in Concrete Structures* Elsevier Science Publishers B. V., Amsterdam, 1988.
30. Goodspeed, C. H., Vaniker, S., Cook, R. A. "High-Performance Concrete Defined for Highway Structures" *Concrete International*, v 18, n2 February 1996.
31. Gross, S. "Instrumentation Plan for the Louetta Road Overpass in Houston" Project 9-580, Center for Transportation Research, The University of Texas at Austin, Sept 1994.
32. Gross, S. "Instrumentation Plan for the San Angelo Bridges" Project 9-589 Center for Transportation Research, The University of Texas at Austin, June 1995.
33. Han, Ningxu *Time Dependent Behaviour of High Strength Concrete* Dissertation, Delft University of Technology, Netherlands, 1996.
34. Kannel, J., French, C. and Stolarski, H. "Release Methodology of Strands to Reduce End Cracking in Pretensioned Concrete Girders" *PCI Journal*, January-February 1997, pp. 42-54
35. Malier, Y. "The French Approach to Using HPC" *Concrete International*, v 13, n 7, July 1991.
36. Malier, Y. *High Performance Concrete – From Material to Structure* E & FN Spon, London, 1992.
37. Marshall, W. T. and Mattock, A. H. "Control of Horizontal Cracking in the Ends of Pretensioned Prestressed Concrete Girders" *PCI Journal*, October 1962, pp. 56-74
38. Mokhtarzadey, A, Kriesel, R., French, C., and Snyder, M. "Mechanical Properties and Durability of High-Strength concrete for Prestressed Bridge Girders" *Transportation Research Record*, n 1478, July 1995.
39. Nawy, E. G. *Fundamentals of High Strength High Performance Concrete* Longman Group Limited, Essex, 1996.
40. Ozyildirim, C. "HPC Bridge Decks in Virginia" *Concrete International*, v 21, n 2, February 1999.
41. Ozyildirim, C., Gomez, J. "High-Performance Concrete in Bridge Structures in Virginia" *Materials for the New Millennium, Proceedings of the Materials Engineering Conference*, v 2, 1996.
42. Ozyildirim, C., Gomez, J., Elnahal, M. "High Performance Concrete Applications In Bridge structures In Virginia" *Worldwide Advances in Structural Concrete and Masonry Structures Congress – Proceedings*, ASCE, New York, NY, 1996.

43. Popovics, S. Concrete Materials – Properties, Specifications and Testing Noyses Publications, New Jersey, 1992.
44. Ralls, M. L., “Texas High Performance Concrete Bridges – How Much Do They Cost?” Concrete International, v 20, n 3, March 1998.
45. Ralls, M. L., “San Angelo High Performance Concrete Bridge in Texas” Worldwide Advances in Structural Concrete and Masonry Structures Congress – Proceedings, ASCE, New York, NY, 1996.
46. Roller, J. J., Russell, H.G., Bruce, R. N., Martin, B. T. “Long-Term Performance of Prestressed, Pretensioned High Strength Concrete Bridge Girders” PCI Journal, November-December 1995.
47. Russell, Henry “High Performance Concrete – From Buildings to Bridges” Concrete International, v 19, n 8, August 1997.
48. Taylor, H. F. W. Cement Chemistry 2<sup>nd</sup> edition, Thomas Telford Publishing, London 1997.
49. Troxell, G. E., Davis, H. E., Kelly, J. W. Composition and Properties of Concrete second edition, McGraw-Hill Inc., New York, 1968.
50. Waszczuk, C. M., Juliano, M. L. “Application of HPC in a New Hampshire Bridge” Concrete International, v 21, n 2, February 1999.
51. White, J., “Thermographic Survey of High Performance Concrete Prestressed Bridge A5529 in Jefferson County, Missouri,” CE350 Honors Report, Advisor: Prof. Vellore S. Gopalaratnam, Department of Civil and Environmental Engineering, University of Missouri-Columbia, December 1999.
52. Yelton, R. “Projects Bridge Gap Between HPC Problems, Solutions” Aberdeen’s Concrete Journal, v 14, n 10, October 1996.
53. Zia, P. Ahmad, S. and Leming, M. “High-Performance Concretes – A State-of-Art Report (1989-1994)” FHWA, Publication Number FHWA-RD-97-030, 1997

## APPENDIX A – TIMELINE FOR IMPORTANT EVENTS

**Table A1 Timeline for important events**

<b>Date</b>	<b>Description of Event</b>
7/23/98	Tensioning of girder LI and LX prestressing strands
7/24/98	Casting of girders LI and LX
7/27/98	Transfer of the prestress for girders LI and LX
7/28/98	Girders LI and LX were moved off the precast bed
7/30/98	Casting of girders SI and SX
8/3/98	Transfer of the prestress for girders SI and SX
8/7/98	Move all girders to the storage yard
10/6/98	Move girders SI and SX to the bridge site
10/8/98	Move girders LI and LX to the bridge site, all girders placed on bents
10/21/98	The diaphragm and slab were cast
11/1/98	Approximate date the bridge was opened to traffic
12/12/98	Load testing of bridge
3/16/99	Intermediate downloading of data
11/16/99	Final download of data

*This unnumbered page is intentionally left blank*

## APPENDIX B – INSTRUMENTATION WIRING SCHEMES USED

Tables B1 through B8 show the wiring schemes that were used during this project. Setup 1, 2 and 3 were used at the different stages of girder life as appropriate.

**Table B1 Multiplexer 1 wiring scheme for Setup 1**

GENERAL INFO			HOOKED TO BOX 1 & 2		HOOKED TO BOX 3 & 4	
Port	Box Number	Wire	Gage ID S-Girders	Location S-Girders	Gage ID L-Girders	Location L-Girders
1-1	2 / 4	2C1	SIE-T1	same	LXE-T1	LIE-T1
1-2	2 / 4	2C2	SIE-T2	same	LXE-T2	LIE-T2
2-1	2 / 4	2C3	SIE-T3	same	LXE-T3	LIE-T3
2-2	2 / 4	2C4	SIE-T4	same	LXE-T4	LIE-T4
3-1	2 / 4	2C5	SIE-T5	same	LXE-T5	LIE-T5
3-2	2 / 4	2C6	SIE-T6	same	LXE-T6	LIE-T6
4-1	2 / 4	2C7	SIE-T7	same	LXE-T7	LIE-T7
4-2	2 / 4	2C8	SIE-T8	same	LXE-T8	LIE-T8
5-1	2 / 4	2C9	SIM-T1	same	LXM-T1	LIM-T1
5-2	2 / 4	2C10	SIM-T2	same	LXM-T2	LIM-T2
6-1	2 / 4	2C11	SIM-T3	same	LXM-T3	LIM-T3
6-2	2 / 4	2C12	SIM-T4	same	LXM-T4	LIM-T4
7-1	2 / 4	2C13	SIM-T5	same	LXM-T5	LIM-T5
7-2	2 / 4	2C14	SIM-T6	same	LXM-T6	LIM-T6
8-1	2 / 4	2C15	SIM-T7	same	LXM-T7	LIM-T7
8-2	2 / 4	2C16	SIM-T8	same	LXM-T8	LIM-T8
9-1	1 / 3	1A1	SXE-T1	same	LIE-T1	LXE-T1
9-2	1 / 3	1A2	SXE-T2	same	LIE-T2	LXE-T2
10-1	1 / 3	1A3	SXE-T3	same	LIE-T3	LXE-T3
10-2	1 / 3	1A4	SXE-T4	same	LIE-T4	LXE-T4
11-1	1 / 3	1A5	SXE-T5	same	LIE-T5	LXE-T5
11-2	1 / 3	1A6	SXE-T6	same	LIE-T6	LXE-T6
12-1	1 / 3	1A7	SXE-T7	same	LIE-T7	LXE-T7
12-2	1 / 3	1A8	SXE-T8	same	LIE-T8	LXE-T8
13-1	1 / 3	1A9	SXM-T1	same	LIM-T1	LXM-T1
13-2	1 / 3	1A10	SXM-T2	same	LIM-T2	LXM-T2
14-1	1 / 3	1A11	SXM-T3	same	LIM-T3	LXM-T3
14-2	1 / 3	1A12	SXM-T4	same	LIM-T4	LXM-T4
15-1	1 / 3	1A13	SXM-T5	same	LIM-T5	LXM-T5
15-2	1 / 3	1A14	SXM-T6	same	LIM-T6	LXM-T6
16-1	1 / 3	1A15	SXM-T7	same	LIM-T7	LXM-T7
16-2	1 / 3	1A16	SXM-T8	same	LIM-T8	LXM-T8

**Table B2 Multiplexer 2 wiring scheme for Setup 1**

GENERAL INFO			HOOKED TO BOX 1 & 2		HOOKED TO BOX 3 & 4	
Port	Box Number	Wire	Gage ID S-Girders	Location S-Girders	Gage ID L-Girders	Location L-Girders
1-1	2 / 4	4A1	SIE-S1	(-)SIE-S1	LXE-S1	(-)LIE-S1
1-2	2 / 4	4A2	SIE-S2	same	LXE-S2	LIE-S2
2-1	2 / 4	4A3	SIE-S3	same	LXE-S3	LIE-S3
2-2	2 / 4	4A4	SIE-S4	same	LXE-S4	LIE-S4
3-1	2 / 4	4A5	SIM-S1	same	LXM-S1	LIM-S1
3-2	2 / 4	4A6	SIM-S2	same	LXM-S2	LIM-S2
4-1	2 / 4	4A7	SIM-S3	same	LXM-S3	LIM-S3
4-2	2 / 4	4A8	SIM-S4	same	LXM-S4	LIM-S4
5-1	2 / 4	4A9	SIN-1	same	LXN-1	LIN-1
5-2	2 / 4	4A10	SIN-2	same	LXN-2	LIN-2
6-1	2 / 4	4A11	SIF-1	same	LXF-1	LIF-1
6-2	2 / 4	4A12	SIF-2	same	LXF-2	LIF-2
7-1	---	RH	Rel Hum	---	Rel Hum	---
7-2	2 / 4	4 Excite	Box 4 Ex	---	Box 4 Ex	---
8-1	1 / 3	1C26	Box 1 Temp	---	Box 1 Temp	---
8-2	---	AT	Amb Temp	---	Amb Temp	---
9-1	1 / 3	3A1	SXE-S1	same	LIE-S1	LXE-S1
9-2	1 / 3	3A2	SXE-S2	same	LIE-S2	LXE-S2
10-1	1 / 3	3A3	SXE-S3	same	LIE-S3	LXE-S3
10-2	1 / 3	3A4	SXE-S4	same	LIE-S4	LXE-S4
11-1	1 / 3	3A5	SXM-S1	same	LIM-S1	LXM-S1
11-2	1 / 3	3A6	SXM-S2	same	LIM-S2	LXM-S2
12-1	1 / 3	3A7	SXM-S3	same	LIM-S3	LXM-S3
12-2	1 / 3	3A8	SXM-S4	same	LIM-S4	LXM-S4
13-1	1 / 3	3A9	SXN-1	same	LIN-1	LXN-1
13-2	1 / 3	3A10	SXN-2	same	LIN-2	LXN-2
14-1	1 / 3	3A11	SXF-1	same	LIF-1	LXF-1
14-2	1 / 3	3A12	SXF-2	same	LIF-2	LXF-2
15-1	---	Cyl TC1	---	---	Slab Temp	---
15-2	1 / 3	3 Excite	Box 3 Ex	---	Box 3 Ex	---
16-1	2 / 4	2C26	Box 2 Temp	---	Box 2 Temp	---
16-2	---	Cyl TC2	---	---	Cyl Temp	---

**Table B3 Multiplexer 3 wiring scheme for Setup 1**

GENERAL INFO			HOOKED TO BOX 1 & 2		HOOKED TO BOX 3 & 4	
Port	Box Number	Wire	Gage ID S-Girders	Location S-Girders	Gage ID L-Girders	Location L-Girders
1-1	2 / 4	2B1c	SIE-V1c	same	LXE-V1c	LIE-V1c
1-2	2 / 4	2B1t	SIE-V1t	same	LXE-V1t	LIE-V1t
2-1	2 / 4	2B2c	SIE-V2c	same	LXE-V2c	LIE-V2c
2-2	2 / 4	2B2t	SIE-V2t	same	LXE-V2t	LIE-V2t
3-1	2 / 4	2B3c	SIE-V3c	same	LXE-V3c	LIE-V3c
3-2	2 / 4	2B3t	SIE-V3t	same	LXE-V3t	LIE-V3t
4-1	2 / 4	2B4c	SIE-V4c	same	LXE-V4c	LIE-V4c
4-2	2 / 4	2B4t	SIE-V4t	same	LXE-V4t	LIE-V4t
5-1	2 / 4	2B5c	SIM-V1c	same	LXM-V1c	LIM-V4c
5-2	2 / 4	2B5t	SIM-V1t	same	LXM-V1t	<b>LIM-V4t</b>
6-1	2 / 4	2B6c	SIM-V2c	same	LXM-V2c	LIM-V2c
6-2	2 / 4	2B6t	SIM-V2t	same	LXM-V2t	LIM-V2t
7-1	2 / 4	2B7c	SIM-V3c	same	LXM-V3c	LIM-V3c
7-2	2 / 4	2B7t	SIM-V3t	same	LXM-V3t	LIM-V3t
8-1	2 / 4	2B8c	SIM-V4c	same	LXM-V4c	LIM-V1c
8-2	2 / 4	2B8t	SIM-V4t	same	LXM-V4t	<b>LIM-V1t</b>
9-1	1 / 3	1B1c	SXE-V1c	same	LIE-V1c	LXE-V1c
9-2	1 / 3	1B1t	SXE-V1t	same	LIE-V1t	LXE-V1t
10-1	1 / 3	1B2c	SXE-V2c	same	LIE-V2c	LXE-V2c
10-2	1 / 3	1B2t	SXE-V2t	same	LIE-V2t	LXE-V2t
11-1	1 / 3	1B3c	SXE-V3c	same	LIE-V3c	LXE-V3c
11-2	1 / 3	1B3t	SXE-V3t	same	LIE-V3t	LXE-V3t
12-1	1 / 3	1B4c	SXE-V4c	same	LIE-V4c	LXE-V4c
12-2	1 / 3	1B4t	SXE-V4t	same	LIE-V4t	LXE-V4t
13-1	1 / 3	1B5c	SXM-V1c	same	LIM-V1c	LXM-V1c
13-2	1 / 3	1B5t	SXM-V1t	same	LIM-V1t	LXM-V1t
14-1	1 / 3	1B6c	SXM-V2c	same	LIM-V2c	LXM-V2c
14-2	1 / 3	1B6t	SXM-V2t	same	LIM-V2t	LXM-V2t
15-1	1 / 3	1B7c	SXM-V3c	same	LIM-V3c	LXM-V3c
15-2	1 / 3	1B7t	SXM-V3t	same	LIM-V3t	LXM-V3t
16-1	1 / 3	1B8c	SXM-V4c	same	LIM-V4c	LXM-V4c
16-2	1 / 3	1B8t	SXM-V4t	same	LIM-V4t	LXM-V4t

**Table B4 Multiplexer 1 wiring scheme for Setup 2**

Port	Box	Wire	Gage ID	Loc'n	Port	Box	Wire	Gage ID	Loc'n
1-1	2	2A1	SIE-S1	same	9-1	1	1A1	SXE-S1	same
1-2	2	2A2	SIE-S2	same	9-2	1	1A2	SXE-S2	same
2-1	2	2A3	SIE-S3	same	10-1	1	1A3	SXE-S3	same
2-2	2	2A5	SIM-S1	same	10-2	1	1A5	SXM-S1	same
3-1	2	2A6	SIM-S2	same	11-1	1	1A6	SXM-S2	same
3-2	2	2A7	SIM-S3	same	11-2	1	1A7	SXM-S3	same
4-1	2	2A9	SIN-1	same	12-1	1	1A9	SXN-1	same
4-2	2	2A11	SIF-1	same	12-2	1	1A11	SXF-1	same
5-1	2	2C26	Box 2 Temp	---	13-1	1	1C26	Box 1 Temp	---
5-2	2	2EX	Box 2 Ex	---	13-2	1	1EX	Box 1 Ex	---
6-1	2	2C4	SIE-T4	same	14-1	1	1C4	SXE-T4	same
6-2	2	2C10	SIM-T2	same	14-2	1	1C10	SXM-T2	same
7-1	2	2C11	SIM-T3	same	15-1	1	1C12	SXM-T3	same
7-2	2	2C12	SIM-T4	same	15-2	1	1C13	SXM-T4	same
8-1	2	2C13	SIM-T5	same	16-1	1	1C14	SXM-T5	same
8-2	---	RH	Rel Hum	---	16-2	---	AT	Amb Temp	---

**Table B5 Multiplexer 2 wiring scheme for Setup 2**

Port	Box	Wire	Gage ID	Loc'n	Port	Box	Wire	Gage ID	Loc'n
1-1	4	4A1	LIE-S1	(-)LXE-S1	9-1	3	3A1	LXE-S1	LIE-S1
1-2	4	4A2	LIE-S2	LXE-S2	9-2	3	3A2	LXE-S2	LIE-S2
2-1	4	4A3	LIE-S3	LXE-S3	10-1	3	3A3	LXE-S3	LIE-S3
2-2	4	4A5	LIM-S1	LXM-S1	10-2	3	3A5	LXM-S1	LIM-S1
3-1	4	4A6	LIM-S2	LXM-S2	11-1	3	3A6	LXM-S2	LIM-S2
3-2	4	4A7	LIM-S3	LXM-S3	11-2	3	3A7	LXM-S3	LIM-S3
4-1	4	4A9	LIN-1	LXN-1	12-1	3	3A9	LXN-1	LIN-1
4-2	4	4A11	LIF-1	LXF-2	12-2	3	3A11	LXF-1	LIF-2
5-1	4	4C26	Box 4 Temp	---	13-1	3	3C26	Box 3 Temp	---
5-2	4	4EX	Box 4 Ex	---	13-2	3	3EX	Box 3 Ex	---
6-1	4	4C5	LIE-T5	LXE-T5	14-1	3	3C5	LXE-T5	LIE-T5
6-2	4	4C11	LIM-T3	LXM-T3	14-2	3	3C12	LXM-T3	LIM-T3
7-1	4	4C12	LIM-T4	LXM-T4	15-1	---	Bad	Port	---
7-2	4	4C13	LIM-T5	LXM-T5	15-2	3	3C14	LXM-T5	LIM-T5
8-1	4	4C14	LIM-T6	LXM-T6	16-1	---	Bad	Port	---
8-2	4	4C15	LIM-T7	LXM-T7	16-2	3	3C16	LXM-T7	LIM-T7

**Table B6 Multiplexer 3 wiring scheme for Setup 2**

Port	Box	Wire	Gage ID	Loc'n	Port	Box	Wire	Gage ID	Loc'n
1-1	4	4B1c	LXE-V1	LIE-V1	9-1	1	1B1c	SXE-V1	Same
1-2	4	4B2c	LXE-V2	LIE-V2	9-2	1	1B2c	SXE-V2	Same
2-1	4	4B3c	LXE-V3	LIE-V3	10-1	1	1B3c	SXE-V3	Same
2-2	4	4B4c	LXE-V4	LIE-V4	10-2	1	1B4c	SXE-V4	Same
3-1	4	4B5c	LXM-V1	LIM-V4	11-1	1	1B5c	SXM-V1	Same
3-2	4	4B7c	LXM-V2	LIM-V2	11-2	1	1B6c	SXM-V2	Same
4-1	4	4B8c	LXM-V3	LIM-V3	12-1	1	1B8c	SXM-V3	Same
4-2	4	4B9c	LXM-V4	LIM-V1	12-2	1	1B10c	SXM-V4	Same
5-1	3	3B1c	LIE-V1	LXE-V1	13-1	2	2B1c	SIE-V1	Same
5-2	3	3B2c	LIE-V2	LXE-V2	13-2	2	2B2c	SIE-V2	Same
6-1	3	3B3c	LIE-V3	LXE-V3	14-1	2	2B3c	SIE-V3	Same
6-2	3	3B4c	LIE-V4	LXE-V4	14-2	2	2B4c	SIE-V4	Same
7-1	3	3B5c	LIM-V1	LXM-V1	15-1	2	2B5c	SIM-V1	Same
7-2	3	3B6c	LIM-V2	LXM-V2	15-2	2	2B7c	SIM-V2	Same
8-1	3	3B8c	LIM-V3	LXM-V3	16-1	2	2B8c	SIM-V3	Same
8-2	3	3B10c	LIM-V4	LXM-V4	16-2	2	2B9c	SIM-V4	Same

**Table B7 Multiplexer 1 wiring scheme for Setup 3**

Port	Box	Wire	Gage ID	Loc'n	Port	Box	Wire	Gage ID	Loc'n
1-1	2	2A1	SIE-S1	same	9-1	1	1A1	SXE-S1	same
1-2	2	2A2	SIE-S2	same	9-2	1	1A2	SXE-S2	same
2-1	2	2A3	SIE-S3	same	10-1	1	1A3	SXE-S3	same
2-2	2	2A5	SIM-S1	same	10-2	1	1A5	SXM-S1	same
3-1	2	2A6	SIM-S2	same	11-1	1	1A6	SXM-S2	same
3-2	2	2A7	SIM-S3	same	11-2	1	1A7	SXM-S3	same
4-1	2	2A9	SIN-1	same	12-1	1	1A9	SXN-1	same
4-2	2	2A11	SIF-1	same	12-2	1	1A11	SXF-1	same
5-1	2	2C26	Box 2 Temp	---	13-1	1	1C26	Box 1 Temp	---
5-2	2	2EX	Box 2 Ex	---	13-2	1	1EX	Box 1 Ex	---
6-1	2	2C4	SIE-T4	same	14-1	1	1C4	SXE-T4	same
6-2	2	2C10	SIM-T2	same	14-2	1	1C10	SXM-T2	same
7-1	2	2C11	SIM-T3	same	15-1	1	1C12	SXM-T3	same
7-2	2	2C13	SIM-T5	same	15-2	1	1C13	SXM-T5	same
8-1	2	2A10	DIA-S2	same	16-1	1	1A10	DIA-S1	same
8-2	---	2A12	DIA-T2	same	16-2	---	1A12	DIA-T1	same

**Table B8 Multiplexer 2 wiring scheme for Setup 3**

Port	Box	Wire	Gage ID	Loc'n	Port	Box	Wire	Gage ID	Loc'n
1-1	4	4A1	LIE-S1	(-)LXE-S1	9-1	3	3A1	LXE-S1	LIE-S1
1-2	4	4A2	LIE-S2	LXE-S2	9-2	3	3A2	LXE-S2	LIE-S2
2-1	4	4A3	LIE-S3	LXE-S3	10-1	3	3A3	LXE-S3	LIE-S3
2-2	4	4A5	LIM-S1	LXM-S1	10-2	3	3A5	LXM-S1	LIM-S1
3-1	4	4A6	LIM-S2	LXM-S2	11-1	3	3A6	LXM-S2	LIM-S2
3-2	4	4A7	LIM-S3	LXM-S3	11-2	3	3A7	LXM-S3	LIM-S3
4-1	4	4A9	LIN-1	LXN-1	12-1	3	3A9	LXN-1	LIN-1
4-2	4	4A11	LIF-1	LXF-1	12-2	3	3A11	LXF-1	LIF-1
5-1	4	4C26	Box 4 Temp	---	13-1	3	3C26	Box 3 Temp	---
5-2	4	4EX	Box 4 Ex	---	13-2	3	3EX	Box 3 Ex	---
6-1	4	4C5	LIE-T5	LXE-T5	14-1	3	3C5	LXE-T4	LIE-T4
6-2	4	4C11	LIM-T3	LXM-T3	14-2	3	3C12	LXM-T2	LIM-T2
7-1	4	4C12	LIM-T4	LXM-T4	15-1	3	3C13	LXM-T3	LIM-T3
7-2	4	4C13	LIM-T5	LXM-T5	15-2	3	3C14	LXM-T4	LIM-T4
8-1	4	4A10	EXT-S2	DECK	16-1	3	3A10	DIA-S3	Same
8-2	4	4A12	LIF-2	LXF-2	16-2	3	3A12	DIA-T3	Same

**Table B9 Multiplexer 3 wiring scheme for Setup 3**

Port	Box	Wire	Gage ID	Loc'n	Port	Box	Wire	Gage ID	Loc'n
1-1	4	4B1c	LXE-V1	LIE-V1	9-1	1	1B1c	SXE-V1	Same
1-2	4	4B2c	LXE-V2	LIE-V2	9-2	1	1B2c	SXE-V2	Same
2-1	4	4B3c	LXE-V3	LIE-V3	10-1	1	1B3c	SXE-V3	Same
2-2	4	4B4c	LXE-V4	LIE-V4	10-2	1	1B4c	SXE-V4	Same
3-1	4	4B5c	LXM-V1	LIM-V4	11-1	1	1B5c	SXM-V1	Same
3-2	4	4B7c	LXM-V2	LIM-V2	11-2	1	1B6c	SXM-V2	Same
4-1	4	4B8c	LXM-V3	LIM-V3	12-1	1	1B8c	SXM-V3	Same
4-2	4	4B9c	LXM-V4	LIM-V1	12-2	1	1B10c	SXM-V4	Same
5-1	3	3B1c	LIE-V1	LXE-V1	13-1	2	2B1c	SIE-V1	Same
5-2	3	3B2c	LIE-V2	LXE-V2	13-2	2	2B2c	SIE-V2	Same
6-1	3	3B3c	LIE-V3	LXE-V3	14-1	2	2B3c	SIE-V3	Same
6-2	3	3B4c	LIE-V4	LXE-V4	14-2	2	2B4c	SIE-V4	Same
7-1	3	3B5c	LIM-V1	LXM-V1	15-1	2	2B5c	SIM-V1	Same
7-2	3	3B6c	LIM-V2	LXM-V2	15-2	2	2B7c	SIM-V2	Same
8-1	3	3B8c	LIM-V3	LXM-V3	16-1	2	2B8c	SIM-V3	Same
8-2	3	3B10c	LIM-V4	LXM-V4	16-2	2	2B9c	SIM-V4	Same